ABSTRACT

Title of Document:
ATLANTIC MULTIDECADAL VARIABILITY: SURFACE AND SUBSURFACE THERMOHALINE STRUCTURE AND HYDROCLIMATE IMPACTS

Argyro Kavvada, Doctor of Philosophy, 2014

Directed By:
Professor Sumant Nigam, Department of Atmospheric and Oceanic Science

Assistant Research Scientist Alfredo Ruiz-Barradas, Department of Atmospheric and Oceanic Science

The Atlantic Multidecadal Oscillation (AMO), a sea surface temperature mode of natural variability with dominant timescales of 30 -70 years and largest variations centered on the northern North Atlantic latitudes is one of the principal climate signals that have earned considerable attention in the recent decades, due to its multilateral impact on both local and remote weather and climate and its importance in predicting extreme events, such as drought development over North America. A 3-dimensional structure of the AMO is constructed based on observations and coupled, ocean-atmosphere 20th century climate simulations. The evolution of modeled, decadal-to-multidecadal variability and its hydroclimate impact is also investigated between two successive model versions participating in the CMIP3 and CMIP5 projects. It is found that both model versions underestimate low frequency variability in the 70-80 and 30-40 year ranges, while overestimating variability in higher frequencies (10-20 year range). In addition, no significant improvements are noted in the simulation of AMO's hydroclimate impact. A subsurface, vertically integrated heat content index (0-1000m) is proposed in an effort to capture the thermal state of the ocean and to understand the origin of AMO variability, especially its surface-subsurface link on decadal- to- multidecadal timescales in the North Atlantic basin. The AMO-HC index exhibits stronger oscillatory behavior and shorter timescales in comparison to the AMO-SST index, while leading the latter by about 5 years. A cooling of the North Atlantic subsurface is discernible in the recent years (mid-2000s –present), a feature that is almost absent at the ocean surface and could have tremendous implications in predicting future North Atlantic climate and in relation to the recent hiatus in the rise of global surface temperatures that was noted in the latest Intergovernmental Panel on Climate Change assessment report. Finally, AMO's decadal variability is shown linked to Gulf Stream's northward surges and the low-frequency NAO, as envisioned by Vinhelm Bjerknes in 1964. A cycle encompassing the low-frequency NAO, Gulf Stream's poleward excursions and the associated shifts in surface winds and SSTs over the subpolar North Atlantic is proposed as a possible mechanism for AMO's origin and a principal target for future research.

ATLANTIC MULTIDECADAL VARIABILITY: SURFACE AND SUBSURFACE STRUCTURE AND HYDROCLIMATE IMPACTS

By

ARGYRO KAVVADA

Dissertation submitted to the Faculty of the Graduate School of the
University of Maryland, College Park, in partial fulfillment
of the requirements for the degree of
Doctor of Philosophy
2014

Advisory Committee:
Dr. Sumant Nigam, Chair, Professor
Dr. Alfredo Ruiz-Barradas, Co-Chair, Assistant Research Scientist
Dr. James Carton, Professor
Dr. Rachel Pinker, Professor
Dr. Derrick Lampkin, Assistant Professor
Dr. Michael Kearney, Professor

Dedication

For my loving parents, Giorgos and Maria Kavvada, my sister Litsa Kavvada
and my grandmother Despoina Karagiannis.

To my dad:

“So, here I am, as promised. Thanks to you. With you, always. ”

Acknowledgements

First and foremost, I would like to thank my advisors, Dr. Sumant Nigam and Dr. Alfredo Ruiz-Barradas for their mentorship, support, guidance, endless scientific insight and friendship. I was fortunate enough to start collaborating with them back in 2010, and ever since, it has been a great experience, filled with challenges, lengthy meetings, data analysis, successes and yes, good times and laughter. I couldn't be more thankful to you, Sumant, for believing in me and encouraging me to always do better, for providing me with great scientific input and helping me strive for more, while obtaining a more holistic view of science and its societal impacts, and finally, for supporting me when things got really hard and almost impossible to handle. Alfredo, what could I say, no words could explain my gratitude to you about your endless support and the sharing of all your valuable knowledge. I can simply say that without you, and without both of you, this PhD thesis and everything I have accomplished in the past four years would not have been possible. So, thank you both, very much.

Next, I would like to thank Dr. Jim Carton, Dr. Rachel Pinker, Dr. Derrick Lampkin and Dr. Michael Kearney for agreeing to take the time and sit on this committee.

I would then like to extend my gratitude to my undergraduate professor, mentor and friend Dr. Adam Falk. I am certain that you are very happy, as I am today, Adam, and I thank you very much for your continuous and so valuable support and great friendship. I also want to thank all my professors and friends from my undergraduate and graduate years. A few important names that come to mind include Dr. Stamatios Krimigis, Dr. Kenneth Shaw, Dr. Hans Engler, Mr. Aris Melissaratos, and Dr. Robert Hudson.

I would like to thank my friends for always believing in me and pushing me to do better, in particular my good friends and family in Greece and my friends and staff members from University of Maryland for making this a wonderful experience.

I then wish to thank my significant other and my best friend, Jose Caceres, for his valuable help while he was the Assistant Systems' Administrator at the Department, and for his love and support and inexhaustible ability to make me laugh and smile.

I finally need to thank the three most important people in my life, my loving family. My sister, Litsa, for being the loving and amazing sister that she always has been, for supporting me endlessly in all the different ways that a sister can love and support another sister. Litsa, without you none of this would have been possible.

I need to thank my mom, Maria, for her endless, unconditional and extraordinary love and support, for always dreaming great dreams of me and helping me make them reality and for making this world such a beautiful place to live in. Mom, without you none of this would have been possible.

I finally need to thank my dad, Giorgos. What could I not say about you, dad? Thank you for the endless years of support and love and laughter and strength and joy? For your powerful, yet delicate, loving and such fulfilling presence? No words would ever be enough. Dad, without you none of this would have been possible.

Table of Contents

List of Tables

List of Figures

Chapter 1: Introduction

1.1 Formulation and Importance of the Problem

The planetary-scale mode of sea surface temperature swings in the North Atlantic basin, known as the Atlantic Multi-decadal Oscillation (AMO) after Kerr (2000), has been noted in several past studies (Kushnir 1994; Enfield et al. 2001; Sutton and Hodson 2005; Guan and Nigam 2009; Ting et al. 2009; Frankcombe 2010; Medhaug and Furevik 2011) and has attracted considerable attention in the recent years due to its extensive impact on regional as well as global weather and climate (e.g., Ting et al. 2011). The principal drivers of these basin-wide SST perturbations are, however, unclear and a common consensus with respect to the origin of North Atlantic SST variability remains to be reached. Some of the most prevailing oceanic and atmospheric mechanisms proposed as key drivers of the AMO include density and salinity fluctuations driven by variations in the Atlantic Meridional Overturning Circulation, AMOC (Bjerknes 1964; Latif et al. 2004; Medhaug and Furevik 2011, Mauritzen et al. 2012; Wang and Zhang 2013), changes in wind forcing and air–sea interactions (Huang et al. 2011), the secular increase of greenhouse gases such as CO2, CH4 etc. (Webster et al. 2005; Mann and Emanuel 2006), as well as fluctuations in atmospheric concentrations of anthropogenic and natural aerosols (Evan et al. 2009; Booth et al. 2012). Research into the origins of the AMO has also opened new questions. A question of key significance addresses the issue of how one can effectively separate the naturally induced, multidecadal North Atlantic SST perturbations from the upward, externally forced, SST trends that are attributed to global warming (e.g., Ting et al. 2009; Guan and Nigam 2009). This along with additional questions involving the influence of the extra-tropical North Atlantic variability on the signal and evolution of the tropical Atlantic SSTs (the decadal variability of the inter-hemispheric SST gradient across the Equator) and the extent to which these interactions manifest complementary features are the focus of ongoing climate research studies.

AMO's hydroclimate impact on the neighboring continents constitutes a cause of great concern, due to the large timescale of the phenomenon and its remarkable socioeconomic effects. Impacts on the regional surface climate associated with the AMO include droughts over North America (Sutton and Hodson 2005; Nigam et al. 2011), decreased rainfall over the Sahel and changes in the frequency and intensity of North Atlantic hurricanes (Knight et al. 2006; Zhang and Delworth 2006; Enfield and Cid- Serrano 2006, Ting et al. 2009; Guan and Nigam 2009) as well as decadal variations in surface air temperature over NE Brazil (Knight et al. 2006) and parts of Northern Europe. Although the SST footprint of the AMO is well identified to the north of the equator, the tropical part has been signaled as being very influential in driving the atmosphere and so the climate impacts (e.g., Sutton and Hodson 2005, Zhang and Delworth 2006) over the neighboring continents; on the other hand, the impact of the midlatitude SST signature has received little attention and just recently Nigam et al. (2011) proposed a mechanism of its influence in driving the global atmosphere.

Multidecadal variability in the North Atlantic can be identified not only in the surface temperatures and Arctic sea ice but also in the subsurface via oceanic heat content, and salinity. As noted in several studies, the North Atlantic Ocean presents an extensive record of perturbations involving SST and salinity (Reverdin et al. 1997; Zhang and Vallis 2006; Polyakov et al. 2005a, b) as well as sea ice anomalies (Deser and Blackmon 1993; Deser et al. 2002). Fresh water anomalies (reduced salinity) over the Labrador Sea, a region of deepwater formation, stratify the ocean layer, contributing thus to the weakening of the thermohaline circulation and deep water formation. This allows for the surface ocean layer to cool down due to the lack of vertical mixing with the warmer subsurface water, which in return and via a positive feedback, inhibits further the deep convection due to a reduction in the heat lost to the atmosphere (Gelderloos et al. 2012).

It is also important to mention that most of Earth's warming signal stemming from human forcing resides in the upper ocean (Hansen et al. 2005; Levitus et al. 2005) which makes difficult the identification of pure natural signals. The oceanic heat content acts as a key indicator of climate perturbations on seasonal, interannual and longer time scales (e.g., Chu 2011; Lozier et al. 2008), accounting thus for the total amount of heat exchange between the ocean and the atmosphere, via heat transport (i.e., surface heat fluxes that dominate variability on seasonal and annual timescales) and heat storage (Kelly and Dong 2004). That is not to say that temperature anomalies in the deeper (1,000–3,000 m) layer below the sunlit zone are not important for climate variability on a global scale, but that their contribution to the net integral of ocean heat content is small, when compared to that of the upper ocean (Levitus et al. 2000). The evolution and respective changes between surface and sub-surface temperature and salinity is also a strong fingerprint of decadal fluctuations in the oceanic overturning circulation (AMOC) and can thus provide significant insight on the vertical structure of the AMO (Zhang 2007) and its linkage to meridional density and salinity transport processes (Sundby and Drinkwater 2002). Assessing such long-term variability, however, can be challenging due to the short record of sub-surface data that is available, in relation to the extensive variability timescale (Keenlyside et al. 2008). Examining therefore the spatial and temporal patterns of sub-surface temperature and ocean heat content is essential in understanding regional warming trends and relating them to low-frequency modes of climate variability.

Advancing our ability to identify the principal drivers and impacts of the AMO, and the relative roles of anthropogenic and natural contributions to AMO's spatiotemporal evolution can therefore:

1. Facilitate the formulation of a more refined image of the North Atlantic SST variability and its local and remote climate influences.
2. Help to improve the accuracy and reliability of climate model projections of future trends.

1.2 Motivation for this Work and Scientific Questions

Achieving the aforementioned goals, however, remains a challenge. Proxy data (ice-core records, tree rings etc.) and climate simulations with models of varied complexity (e.g., Frankcombe 2010; Hodson et al. 2010) offer supplemental tools for improving our understanding of such low frequency, planetary-scale interactions. A holistic image of the AMO and its climate impacts, as well as its accurate representation in climate simulations is yet to be reached, however. Specifically, this study aims at addressing the following fundamental open questions:

1. How robust is the observed AMO spatial structure and how does it evolve through time?
2. How are low frequency North Atlantic sea surface temperature perturbations associated with vertically integrated salinity and heat content anomalies?
3. How do simulations from state-of-the-art global, coupled ocean-atmosphere models participating in the CMIP3 (Meehl et al. 2007[1]) and CMIP5 (Taylor et al. 2012[2])

projects portray the observed spatiotemporal features of the AMO and its surface climate impact?

4. Is there satisfying progress from CMIP3 to CMIP5 projects in simulating AMO-related variability, its structure and hydroclimate impact?
5. What is the link between surface and subsurface temperature, salinity and density anomalies in the subpolar North Atlantic, and how do they relate to the decadal and multidecadal spectral peaks of the AMO, from an observational point of view?
6. How are the low-frequency changes in the Gulf Stream's latitudinal position related to the AMO and extra-tropical atmospheric variability?

These questions are addressed by the following fundamental tasks:

- Identification of the three-dimensional structure and temporal evolution of the AMO in observations and their characterization in historical simulations of the 20th century climate from models that participated in the latest CMIP5 project (Chapter 2).
- Assessment of the representation of the AMO and its hydroclimate impact in simulations of the 20th century climate from CMIP3 to CMIP5 projects (Chapter 3).
- Characterization of subsurface low-frequency features of the AMO through (Chapter 4):
    - An alternate definition of the AMO based on vertically integrated heat content in order to enhance subsurface ocean variability and minimize atmospheric variability.

- Identification of the thermohaline structure of the subpolar North Atlantic in relation to the AMO with a focus on the Labrador and Irminger Seas.
- Clarification of the phase relationship between the AMO and the North Atlantic Oscillation-Gulf Stream couplet.
- Analysis of the subpolar North Atlantic during the past decade.

The thesis is concluded with a brief summary of the main results and key remarks (Chapter 5).

Chapter 2: AMO's Structure and Climate Footprint in Observations and IPCC AR5 Climate Simulations

2.1 Introduction

The planetary-scale mode of sea surface temperature swings in the North Atlantic basin, known as the Atlantic Multi-decadal Oscillation (AMO) after R. Kerr (2000), has been noted in several past studies (Kushnir 1994; Enfield et al. 2001; Sutton and Hodson 2005; Guan and Nigam 2009; Ting et al. 2009; Frankcombe et al. 2010; Medhaug and Furevik, 2011) and has attracted considerable attention in the recent years due to its extensive impact on regional as well as global weather and climate (e.g. Ting et al. 2011). The principal drivers of these basin-wide SST perturbations are, however, unclear and a common consensus with respect to the origin of North Atlantic SST variability remains to be reached. Some of the most prevailing oceanic and atmospheric mechanisms proposed as key drivers of the AMO include density and salinity fluctuations driven by variations in the Atlantic Meridional Overturning Circulation, AMOC (*Bjerknes* 1964; Latif et al. 2004; Medhaug and Fuverik 2011), changes in wind forcing and air-sea interactions (Huang et al. 2011), the secular increase of greenhouse gases such as CO_2, CH_4 etc. (Webster et al. 2005, Mann and Emanuel 2006), as well as fluctuations in atmospheric concentrations of anthropogenic and natural aerosols (Evan et al. 2009, Booth et al. 2012). A question of key significance addresses the issue of how one can effectively separate the naturally induced, multidecadal North Atlantic SST perturbations from the upward, externally forced, SST trends that are attributed to global warming (e.g., *Ting et al.,* 2009; *Guan and Nigam*, 2009). This along with supplemental, open questions involving the influence of the extra-tropical North

Atlantic variability on the signal and evolution of the tropical Atlantic SSTs (the decadal variability of the inter-hemispheric SST gradient across the Equator) and the extent to which these interactions manifest complementary features are the focus of ongoing climate research studies.

Persistent, large-scale SST anomalies exert a meaningful and often predictable influence on climate. AMO's hydroclimate impact on the neighboring continents is thus well anticipated and constitutes a cause of great concern, due to the large timescale of the phenomenon and its remarkable socioeconomic effects. Impacts on the regional surface climate associated with the AMO include droughts over North America (Sutton and Hodson 2005, Nigam et al. 2011), decreased rainfall over the Sahel and changes in the frequency and intensity of North Atlantic hurricanes (Knight et al. 2006, Zhang and Delworth 2006, Enfield and Cid-Serrano 2009, Ting et al. 2009, Guan and Nigam 2011) as well as decadal variations in surface air temperature over NE Brazil (Knight et al. 2006) and parts of Northern Europe.

Apart from the atmospheric response, multidecadal variability in the North Atlantic climate system also exhibits a signature on subsurface oceanic heat content and salinity, as well as on Arctic sea ice. As noted in several studies, the North Atlantic Ocean presents an extensive record of perturbations involving SST and salinity (Reverdin et al. 1997; Zhang and Vallis 2006; Polyakov et al. 2005) as well as sea ice anomalies (Deser and Blackmon 1993; Deser et al. 2002). Fresh water anomalies (reduced salinity) over the Labrador Sea, a region of deepwater formation, stratify the ocean layer, contributing thus to the weakening of the thermohaline circulation and deep water formation. This allows for the layer to cool down due to the lack of vertical mixing with the warmer subsurface water, which in turn and via a positive feedback, inhibits further the deep convection due to a reduction in the heat lost to the atmosphere (Gelderloos et al. 2012).

Furthermore, most of Earth's warming signal stemming from human forcing resides in the upper ocean (Hansen et al. 2005, Levitus et al. 2005). That is not to say that temperature anomalies in the deeper (1000-3000 m) layer below the sunlit zone are not important for climate variability on a global scale, but that their contribution to the net integral of ocean heat content is small, when compared to that of the upper ocean (Levitus et al. 2000). The oceanic heat content acts as a key indicator of climate perturbations on seasonal, interannual and longer time scales (e.g., Chu 2011, Lozier at al. 2008), accounting for the total amount of heat that is made available to the atmosphere, via heat transport (i.e. surface heat fluxes that dominate variability on seasonal and annual timescales) and heat storage (Kelly and Dong 2004). Examining, thus, the spatial and temporal patterns of sub-surface temperature and ocean heat content is essential in understanding regional warming trends and relating them to low-frequency modes of climate variability. The evolution and respective changes between surface and sub-surface temperature and salinity is also a strong fingerprint of decadal fluctuations in the oceanic overturning circulation (AMOC) and can thus provide significant insight on the vertical structure of the AMO (Zhang 2007) and its linkage to meridional density and salinity transport processes (Sundby and Drinkwater 2002). Assessing such long-term variability, however, can be challenging due to the short record of sub-surface data that is available, in relation to the extensive variability timescale (Keenlyside et al. 2008).

Advancing our ability to identify the principal drivers and impacts of the AMO, and the relative roles of anthropogenic and natural contributions to AMO's spatiotemporal evolution can therefore facilitate *1)* the formulation of a more refined image of the North Atlantic SST variability and its local and remote climate influences and *2)* the accuracy and reliability of climate model projections of future trends. Achieving these goals, however, remains a challenge;

proxy data (ice-core records, tree rings etc.) and climate simulations with models of varied complexity (e.g., Frankcombe 2010, Hodson et al. 2010) offer supplemental tools for improving our understanding of such low frequency, planetary-scale interactions. A holistic image of the AMO and its climate impacts, as well as its accurate representation in climate simulations is yet to be reached, however.

In this study, the structure and evolution of the Atlantic Multidecadal Oscillation have been investigated in observations and model simulations of the 20th century climate from models participating in the CMIP5 project (Taylor et al*.,* 2011). We have sought to identify ways in which the spatiotemporal evolution of North Atlantic SSTs that are associated with the AMO compares between models and observations, while also constructing a 3-dimensional image of its structure, by examining decadal-scale perturbations on the North Atlantic surface, subsurface, as well as the overlying atmosphere [1]. Some of the central questions that have been addressed include:

- How robust is the AMO structure and how does it evolve through time (i.e. how coherently does it evolve in space and time)?
- Is the AMO associated with deep, coherent salinity and heat content anomalies?
- How do simulations from four state-of-the-art global climate models participating in the CMIP5 project portray the observed features of the AMO and its surface climate impact?

2.2 Datasets and Analysis Methods

2.2.1 Datasets

---

[1] The use of coupled, ocean-atmosphere models from the CMIP5 project allows for the ocean circulation to freely evolve, facilitating, in this way, a more accurate understanding of the AMO-related ocean state and its imprint on local as well as remote climate features. A downside of this approach, however, is that in such models, there are so many fields that are varying simultaneously, that it becomes very challenging to separate cause from effect.

To investigate the structure, properties and impacts of the AMO, we used a variety of observational variables including sea surface temperature (SST), sub-surface potential temperature and salinity, as well as geopotential height, surface air temperature and precipitation. The SSTs were obtained from the Met Office's (UKMO) Hadley Centre Sea Ice and Sea Surface Temperature dataset, HadISST version 1.1 (Rayner et al. 2005), available on a 1°×1° grid at a monthly resolution for the 1870-present period. Both subsurface temperature and salinity fields were obtained from the National Oceanographic Data Center (NODC) (Levitus et al. 2001) and the SODA Ocean Reanalysis product, version 2.2.4 (Carton et al. 2005). The NODC dataset included subsurface temperature anomalies on a 1°×1° horizontal grid with 26 vertical levels (sfc–2000m) at seasonal resolution for the winter 1955 – fall 2010 period. NODC subsurface salinity measurements were provided as 5-year (pentadal) averaged anomalies (Boyer et al. 2005) at annual resolution on a 1°×1° horizontal grid and with 26 vertical levels, for the period 1955–2006. The SODA 2.2.4 dataset was provided at a 0.5°×0.5° horizontal grid with 40 vertical levels, at monthly resolution for the period between January 1871 and December 2008. Geopotential height data were obtained from the National Center for Environmental Prediction (NCEP) Reanalysis (Kalnay et al. 1996) at a horizontal resolution of 2.5°×2.5° and with 17 vertical levels, at monthly resolution for the January 1949 – December 2009 period. Finally, we obtained precipitation and surface air temperature data from the CRU TS3.1 monthly data set (Mitchell and Jones 2005), available over land points at a 0.5°x0.5° resolution for the January 1901 – October 2009 period.

Models from the CMIP5 project that we used to analyze the 20th century climate simulations included those from leading climate research centers around the world: NCAR's CCSM4 (6 ensemble members), NOAA's GFDL-CM3 (5 ensemble members), UK Meteorological Office's

UMKO-HadCM3 (9 ensemble members) and the German Max Planck Institute's ECHAM6/MPI-ESM-LR (3 ensemble members). For most models, the historical simulation scenario covered the period 1850/1860 – 2005. The time varying forcing agents that were employed included emissions or concentrations of natural and anthropogenic aerosols (or their precursors), solar forcing, greenhouse gases (CO_2, CH_4, N_2O), atmospheric composition as well as land use change (Meinshausen et al. 2011). Table 1 shows the model simulations (ensembles) that were used (based on availability at the time) for the analysis of the different oceanic and atmospheric, AMO-related fields.

2.2.2 Methods

The current analysis aimed at documenting the spatiotemporal characteristics and evolution of the observed and modeled low frequency AMO pattern, along with its impact on various seasonal resolution fields for the period 1900-1999. Seasonal averages of the different monthly variables were calculated based on the usual Northern Hemisphere meaning of the three-month season average: December-February for winter, March-May for spring, June-August for summer and September-November for fall. Seasonal anomalies of the different fields were calculated by subtracting the seasonal climatology (i.e., the long-term mean using the 1900-1999 base period, unless noted otherwise) from the seasonal fields. Observed and simulated AMO indices were created by taking the following steps: a. constructing the observed and simulated AMO indices by first averaging the respective seasonal SST anomalies (SSTA) over the Atlantic region (5°-75°W, 0°-60°N)[2], and subsequently, linearly de-trending them over the January 1900- October 1999 period, using the least-squares method, b. smoothing these indices by applying a binomial (1-2-1)

---

[2] Note the similarity in the domain used to define the area-averaged SST anomalies by Sutton and Hodson (2003) which used the 7.5°-75°W, 0°-60°N domain, as well as the different way to smooth the area-averaged SST anomalies by using a 37-point Henderson filter.

filter 50 times to efficiently remove interannual variations without aliasing the decadal-scale pulses and c. normalizing the de-trended and smoothed time series to unit variance, by dividing each time series by the respective standard deviation of the calculated index. Finally, indices for a specific season were created by extracting that season from the all-season, smoothed and normalized index.

Lead/lag regressions of the all-season (derived from step a.) AMO indices on the different field variables were calculated for both observational and model-generated data. Regressions from model simulations were computed for each ensemble member of a given model, separately, and a mean value of the combined regression results was subsequently obtained and shown (rather than demonstrating the regressions on the mean ensemble field of a given model).

It should be noted that the defined seasons for the provided temperature anomalies from NODC were calculated in a slightly different way, in comparison to the ones from other datasets that were used in this analysis: January-March was used for winter, April-June for spring, July-September for summer and October-December for fall. Finally, since the NODC salinity anomalies were given at annual resolution, we linearly interpolated this dataset in time, to create its seasonal version. Despite the fact that this technique did not produce meaningful seasonal values and it wasn't thus optimal for researching the time evolution or spatial footprint on a particular season, it allowed the investigation of all-season, contemporaneous salinity regressions and latitudinal salinity profiles (seasonal differences were leveled out in this case.)

2.3 Results

2.3.1 Observed versus modeled, spatiotemporal features of the AMO

Climate simulations of the 20th century constitute a real challenge for the models, since they largely depend on their ability to simulate natural variability given the relatively modest role of the observed GHG and aerosol forcing that is being used (in comparison with the 21st century, forced projections). Thus, a first-order question that one can ask is whether the models possess the necessary elements to portray the characteristic, basin-wide SST anomalies that relate to the AMO. The structure of the SST anomalies associated with the warm phase of the AMO in observations and simulations is shown in Figure 2.1, via simultaneous all season regressions. Positive anomalies are present over the entire North Atlantic basin in observations, with maximum values of as high as 0.4K arising just south of Greenland in the mid-latitudes, between 40° and 50° N and 35° to 45°W and with a secondary maximum (half the size of the one over the mid-latitudes) noted over the northern tropical Atlantic, off of the coast of northwest Africa; normal conditions are evident in the western subtropical latitudes.

The four models capture the general spatial structure of the SST anomalies as portrayed in observations, with some clear differences, however. Most models exhibit a region of positive anomalies in the mid-latitudes, while placing the maximum of the anomalies further to the east (southeastward of Greenland) than observations show; furthermore, the models also exhibit weaker positive anomalies over the Davis Strait and the Labrador Sea, while also showing a weaker secondary maximum off of the northwestern African coast, in comparison to observations. It is interesting to note that GFDL-CM3 is the only model that portrays the same anomalies over the Labrador Sea as seen in observations, with the subtropical/tropical extension of the anomalies appearing further to the west; anomalies are also shown over the equatorial Pacific, a feature not present in observations. On the other hand, anomalies in CCSM4 are constrained to the northern latitudes, with two local maxima southward of Iceland and over the

Greenland Sea, but with normal conditions off of the northwest African coast. Similarly to GFDL-CM3, CCSM4 demonstrates anomalies over the equatorial Pacific that are not present in observations. Anomalies over the N. Atlantic mid-latitudes from ECHAM6/MPI-ESM-LR and UKMO-HadCM3 appear weaker and stronger, respectively, in comparison to observations. In addition, the latter two models appear unable to capture the magnitude of the observed anomalies in the subtropical/tropical Atlantic, with UKMO-HadCM3 being closer to observations than ECHAM6/MPI-ESM-LR.

After investigating the spatial structure of the AMO at the surface, we now concentrate on the propagation of its spatial footprint through time. For this purpose, we compare the time series of the observed and model-based AMO indices for the January 1900 – October 1999 period, while choosing to display the AMO time series of the ensemble member (of each model) that manifests the highest correlation with observations (2.1, bottom panel.) The AMO index from GFDL-CM3, Run 5, is the closest to the observed index, with a simultaneous correlation of 0.75. This is followed by the AMO index from UKMO-HadCM3, Run 5, with a 0.48 correlation, and the index from CCSM4, Run 4, with a correlation of 0.29. Finally, the AMO index from ECHAM6/MPI-ESM-LR, Run 3, shows the least co-variability with observations, with a maximum correlation of 0.01. All correlation coefficients for the ensemble members of each model are shown in Table 2. The statistical significance of the correlations is assessed via a two-tailed Student's t-test at the 5% level using an effective sample size that accounts for serial correlation (Quenouille, 1952), Ne ($=N/[1 + 2r_{x,1}r_{y,1} + 2r_{x,2}r_{y,2} + ...]$), where N is the time-series length (here 300 seasons after the smoothing); $r_{x,1}$, $r_{x,2}$... are the first, second, ...-order autocorrelations for the observed time series (x), and $r_{y,1}$, $r_{y,2}$... are the corresponding first, second, …-order autocorrelations for the time series of each ensemble member of each model ensemble mean (y); stable Ne (and thus t-test) values are obtained by summing up to the 6^{th}-order. The degrees of freedom corresponding to the ensemble mean for all four models are found to be in the 24-26 range so a value of 25 was used. Based on this analysis, the critical correlation is subsequently calculated via the formula: $t = r * \sqrt{\frac{N_e}{1-r^2}}$ and is found to be |±*0.38*|. Correlations above this value are considered statistically significant.

Supplemental information regarding the spatial and temporal features of the smoothed AMO indices derived from observations and the ensemble means of the four models is found in Figure 2.2, via the use of Taylor diagrams (Taylor, 2005). Comparison of the temporal features of the AMO indices indicates that the majority of the models have poor correlation with observations and under-estimate the observed variability, with the exception of GFDL CM3, which shows a slightly above 0.5 correlation to observations and a standardized, standard deviation of ~ 0.94. Regarding the spatial variability and spatial correlations between the observed and modeled SST anomalies of the mature phase of the AMO, UKMO-HadCM3 is the best among the four models in depicting AMO's observed, spatial structure, with a correlation of 0.74, followed by MPI-ESM-LR and GFDL CM3, with correlations of 0.55 and 0.24, respectively. CCSM4 is the least efficient in capturing the spatial structure and variability of the AMO, with temporal and spatial correlations of -0.01 and -0.16, respectively. To resume, UKMO-HadCM3 and MPI-ESM-LR seem to be most efficient in capturing the spatial features of the mature phase of the AMO, whereas GFDL CM3 appears to be the best model in capturing AMO's temporal structure and variability.

Next, we focus on the time scale of the AMO indices, by looking at their autocorrelation functions (Fig. 2.3). The time span defined by the crossing of the autocorrelation line of the AMO index with the zero line at both ends indicates the half-period of the AMO index[3]. The crossing of the autocorrelation of the observed AMO index with the zero line (thick black line) shows a dominant period of approximately 58 years. The color lines, representing the mean autocorrelation for each model, display varying amplitudes and a general underestimation of the AMO period. These appear to be relatively close together, particularly the ones corresponding to UKMO-HadCM3, CCSM4 and GFDL-CM3 models, with periods of 52, 50 and 48 years, respectively (looking at the zero line crossing); the ECHAM6/MPI-ESM-LR autocorrelation function demonstrates the shortest period (40 years). An estimate of the observed and model-based AMO periods is shown in Table 3. It is interesting to point out that while the characteristic time of the AMO indices by the models is up to 31% apart from the observed value when considering the zero crossing metric, it is further apart (within 65% of the observed value) when considering the time needed for the autocorrelations to decay to 1/e of their values, a measure of the memory or persistency of the AMO. Graphically, this suggests that higher frequency variability remains present in the model indices, in contrast to the observed AMO index. Spectral analysis of the smoothed AMO indices is displayed in Figure 2.4 (histograms of the spectral peaks, derived from the mean spectral peaks of the different model ensembles are shown in 10-yr bins). The observed smoothed AMO index (Figure 2.4) reveals a spectral peak in the 70-80 years range, which is four times larger than the peak in the 10-20 years range. However, the mean spectral peaks in the 10-20 years range of the smoothed indices from model simulations have a more prominent role than their corresponding 70-80 year peaks (and than the ones seen in observations); in fact, these higher frequency peaks are comparable to (actually slightly larger

---

[3] That is, the time to take the anomaly to grow from climatological conditions to reach its maximum value and then go back to climatological conditions before going in the opposite direction.

than) their 70-80 year peaks. This helps explain why the peaks displayed in the autocorrelation of the indices in Fig. 2.3 are so narrow.

An additional insight with respect to the models' skill to simulate low-frequency variability over the North Atlantic Ocean associated with the AMO is investigated by the evolution of the SST anomalies associated with the AMO via all-season lead/lag regressions, four years before and after the mature phase of the AMO (Figure 2.5). Observations indicate that positive SST anomalies emerge from the Davis Strait and Labrador Sea following a southeastward propagation in the higher mid-latitudes and a subsequent southwestward advection in the lower latitudes, as time evolves, tracking the east branch of the subtropical gyre until they reach maximum amplitude and extension in the mature phase. The subtropical anomalies appear weaker than those in the mid-latitudes, with a local maximum developing off of Northwest Africa. In the post-mature phase, the anomalies gradually abate, with the signal first dissipating over the tropical latitudes and subsequently further to the north. Positive anomalies over the North Pacific appear more extensive in the SODA-based AMO evolution than in the HadISST dataset[4].

The modeled AMO structure and evolution around the mature phase of the AMO (±4 years) agrees partially with observations, particularly in the mid-latitudes just before and after the mature phase (±2 years). Noticeable differences are present, however, in the CCSM4 evolution, which manifests a focus on the northern North Atlantic over the Greenland Sea that is not present in observations; furthermore, GFDL-CM3 and ECHAM6/MPI-ESM-LR show negative anomalies at the end of the +4 years lag period, a feature that is also not present in observations. Except for CCSM4, anomalies in the other three models reach maximum latitudinal extension

---

[4] To investigate this difference, we used NOAA's Extended Reconstructed SST data set (ERSSTv3b, Smith et al. 2008) to generate a smoothed AMO index and lead/lag SST regressions (not shown); the pattern that emerges agrees with the lead/lag regressions from HadISST, with SST anomalies over the Pacific being less widespread than the ones noted in the SODA lead/lag regressions.

into the tropics in the mature phase; GFDL-CM3 and UKMO-HadCM3 exhibit a greater ability in capturing AMO-related anomalies in the tropical North Atlantic, which remains almost completely quiescent in the other two models, during the pre- and post-mature phases (in contrast to observations). It can therefore be inferred that even though the models do capture the northward focus of the observed SSTA maxima, they lack the ability to effectively reproduce their structure and evolution, especially over the tropical part. The quick setting and dismissal of the simulated tropical SST anomalies may be related to the superficial nature of the anomalies, with little consideration of subsurface processes, in the models.

2.3.2 Subsurface features of the AMO: Salinity

The identification of footprints of low-frequency variability of North Atlantic SSTs on ocean surface and sub-surface fields is essential for the construction of a more holistic image of the AMO. The current study focuses on the sfc–50m oceanic layer in an attempt to assess the spatial distribution, magnitude and vertical structure of any AMO-related salinity anomalies during the winter 1955–fall 1999 period, which is common among observations and model simulations. The AMO indices are re-calculated for this shorter period (by using NODC, SODA and simulated SST fields, respectively, Figure 2.6).

The regressed observed SST anomalies from the 1955-1999 period (Fig. 2.6, left column, upper two panels) display only a small variation in their structure, when compared with those of the larger period (Fig. 2.1), with slightly weaker/stronger anomalies over the mid/tropical Atlantic and almost normal conditions over the subtropical western Atlantic (off of the eastern US coast). Negative anomalies are now discernible, north of the Greenland Sea. The associated anomalies over the Atlantic mid-latitudes appear of the same magnitude to the ones over the tropics. The simulated anomalies for this shorter period retain their spatial structure, as seen in the longer period, but are unable to capture the extension and magnitude of the cold anomalies off of the US coast as well as the increase in magnitude of the anomalies over the tropical Atlantic. Except for GFDL-CM3, the other three, simulated regressed anomalies are of smaller magnitude, in comparison to the longer period ones. (Fig. 2.6, left column, lower four panels).

Regressed salinity anomalies are analyzed as a vertical mean along the sfc–50m layer (Fig. 2.6, central column) and as a vertical profile (Fig. 2.6, right column). Contained, positive, vertically-averaged (sfc-50m) salinity maxima are noted in observations in the mid-latitudes, south of Greenland (Fig. 2.6, central column, upper two left panels), while negative values are evident in NODC along the northeastern US coast. We note that the negative salinity anomalies in NODC agree with the observed, negative SST anomalies, a co-occurrence absent from the SODA-derived regressions. Negative salinity anomalies are also found in the western northern tropical Atlantic, between the Equator and 25° N, while positive anomalies are discernible over the Davis and Fram Straits as well as over the Labrador and Greenland Seas, in both NODC and SODA datasets.

The latitudinal profile of the regressed salinity anomalies along the 35°-50°W band in the upper 50m indicates a coherent vertical structure (Fig. 2.6, right column, upper two panels). The observed contrasting anomalies identified in the vertical average (south of Greenland and in the northern tropical Atlantic) extend into the subsurface. It is worth noting that lead/lag regressed salinity anomalies (not shown) indicate a counterclockwise propagation of sub-Arctic water into the North Atlantic, from the Davis Strait extending southward into the Labrador, Greenland and Norwegian Seas. Such decadal pulses are evident in past incidents of low salinity and sea surface temperature anomalies in the region, such as the Great Salinity Anomaly of 1968-82 (Slonosky et al. 1997). Our analysis, hence, supports the notion that N. Atlantic surface temperature and salinity show coherent, low frequency fluctuations, which are consistent with heat and freshwater interactions between the Arctic and the N. Atlantic basins (Polyakov et al. 2005).

Mean regressed positive salinity anomalies from the four models (Fig. 2.6, central column, four lower panels) are reminiscent of the regressed SST positive anomalies that have already been analyzed (Fig. 2.6, left panels). While GFDL-CM3, ECHAM6/MPI-ESM-LR and UKMO-HadCM3 exhibit maximum positive salinity anomalies over the regions of maximum SST positive anomalies in the mid-latitudes, CCSM4 manifests negative anomalies, with only hints of a positive signal off of the southwestern tip of Greenland; anomalies over the subtropical region off of the northwest African coast are portrayed in different ways by all four models. GFDL-CM3 captures the extent and spatial variability of AMO-related salinity anomalies, while exaggerating, however, their magnitude; prominent positive anomalies are evident south of Greenland, along with negative anomalies off of the northeastern US (seen in the NODC map) and off of the northwestern African coast. ECHAM6/MPI-ESM-LR and UKMO-HadCM3 depict salinity maxima slightly displaced eastward (in comparison to the observations). Finally, none of the models is able to simulate the positive salinity anomalies over the Straits around Greenland (from the NODC and SODA maps).

The salinity profiles from the model simulations (Fig. 2.6, four lower right panels) show that the profile from the GFDL-CM3 model is the closest to the observed one, even though it manifests mid-latitude negative anomalies that are not present in observations. Salinity profiles from CCSM4 and ECHAM6/MPI-ESM-LR are in the least agreement with observations, despite the fact that they demonstrate a coherent salinity structure through the sfc-50m layer. On the other hand, the salinity profile from UKMO-HadCM3 does not show any resemblance to the observed profiles and is characterized by negative salinity anomalies underneath the positive ones, in the mid-latitudes. In short, the models appear challenged in portraying the position and magnitude of AMO-related, salinity anomalies, with GFDL-CM3 being the most successful in capturing the spatial variability of the SSTA-associated, salinity field.

2.3.3 Subsurface features of the AMO: Ocean Heat Content

As mentioned in the Introduction, heat content has been identified as an important marker in climate variability studies. It is therefore important to examine some of the directly observable sub-surface signatures of the AMO, such as the sub-surface temperature and oceanic heat content.

Subsurface temperatures from NODC, SODA and model simulations are used to obtain vertically integrated heat content anomalies for the sfc-400m layer. Figure 2.7 shows lead/lag regressions of the AMO on the oceanic heat content four years before and after its mature phase, at two-year intervals. It is worth noting the coincidence of the anomalies between the NODC and SODA datasets. Four years before the mature warm phase of the AMO, the Atlantic is crossed by negative heat content anomalies in the mid-latitudes (~45°N), extending from the Newfoundland to the UK (along the Gulf Stream's northern extension) and positive anomalies in the subtropics, off of the eastern US coast and along the southern tip of Greenland that reach as far as the Nordic Sea; the deep tropics are marked by cold heat content anomalies. Two years later (that is, two years before the mature warm phase), the cold heat content anomalies that were crossing the mid-Atlantic earlier, have now moved to the Nordic Sea and along the eastern US coast, while the warm heat content anomalies over southern Greenland appear expanded southward. The warm anomalies off of the eastern US have moved further to the east, toward the central subtropics, at about 30°N, with a southward extention to the tropics, off of the northwest African coast. Finally, the cold anomalies that were present in the deep tropics earlier have almost disappeared.

As time evolves toward the mature phase, the positive anomalies over southern Greenland propagate southeastward along the European and African western coasts, while the subtropical warm anomalies weaken. The cold anomalies along the eastern US extend toward the central Atlantic and the ones over the western northern tropical Atlantic are being replaced by warm anomalies. During the post-mature phases, in both the NODC and SODA maps, the cold anomalies continue to propagate toward the central mid-Atlantic; warm anomalies around the southern tip of Greenland are being displaced further to the east, allowing for cold anomalies to develop over the Labrador Sea and the Davis Strait. Furthermore, the warm link between the mid and tropical Atlantic off of the northwestern African coast is weakened. It is important to note that the SST anomalies (Fig. 2.6) over the Davis Strait and Labrador Sea, as well as those over the Fram Strait (northeast of Greenland) and along the coastal, eastern US, are coincident with the same sign anomalies in heat content over the same regions, not only during the mature phase (e.g. compare Fig. 2.6, upper two panels in left column with Fig. 2.7 upper two panels in central column) but also in the pre- and post-mature phases (not shown).

GFDL-CM3 appears to be the most efficient model in capturing the spatial pattern and systematic evolution of the observed, warm and cold heat content interchanges, especially during the mature and post-mature phases. Among the other 3 models, CCSM4 lacks the ability to efficiently portray a reasonable evolution of the AMO-related, heat content anomalies, whereas UKMO-HadCM3 and ECHAM6/MPI-ESM-LR exhibit a better propagation of sub-surface temperature anomalies, with a principal focus in the northern mid-latitudes. The tropical North

Atlantic in the latter two models appears more quiescent during the pre- and post-mature phases, similarly to the pre- and post-cursor periods of the SSTA evolution (not shown for this shorter period but very similar to the ones examined in Fig. 2.5).

2.3.4 AMO's Atmospheric Footprint

A thorough characterization of the AMO is not complete without its associated signature on the atmosphere and surface climate over the neighboring continents. Investigation of seasonality is of great importance, given the possibility of canceling/building effects that may arise from season to season throughout the year. The seasonality of AMO's influence on the overlying atmosphere is analyzed via regressions of the AMO index on the 500mb circulation anomalies (Fig. 2.8). It is important to note that these simultaneous regressions include both the atmospheric weather noise (the part of atmospheric variability that does not emerge as a result of boundary or external forcing mechanisms (Schneider and Fan 2007) and AMO's atmospheric response, which tends to abate SST variability. To extract AMO's forced response in atmospheric and other climate features (i.e. hydroclimate), one needs to remove the weather noise-related surface fluxes and variability from the observed SST evolution, as shown in Fan and Schneider (2012), by i.e. employing an interactive model configuration of a coupled GCM forced by weather noise surface fluxes, to isolate the individual contribution of local weather surface fluxes to the N. Atlantic SST variability. Such an approach could advance investigation of the mechanisms that lead to such low-frequency SST pulses, as shown in Schneider and Fan (2012).

Observations (top four panels, Fig. 2.8) show prominent winter geopotential height anomalies that decrease to a minimum during the summer. A resemblance to the negative NAO pattern of high pressure over the Icelandic region and a contrasting pattern of low pressure over the western Atlantic-Azores region are discernible during winter. Furthermore, the geopotential height patterns exhibit same-sign anomalies for different atmospheric levels (not shown here), indicating the existence of an equivalent barotropic structure. A supplemental feature that is worth mentioning is the high-low-high wave pattern that emerges during the fall season over the US-Labrador Sea region, with a ridge (trough) over the western (eastern) US; this is essential in relating circulation anomalies to perturbations in surface temperature and precipitation over the continental US (examined further below.)

The four models exhibit some problems while attempting to simulate the observed seasonality of the atmospheric, SST-related features and the associated regional circulation patterns. While portraying their own version of the observed winter ridge/trough over the Icelandic/western Atlantic-Azores region, most of them are unable to capture the atmospheric seasonality that is characterized by a summer minimum in the anomalies. It is revealing to find out that while GFDL-CM3 was shown to be the best model in reproducing observed features over the ocean, it is the worst in capturing the respective atmospheric patterns via geopotential height regressions; some of the key, contradictory features (with respect to observations) include maximum positive anomalies over the Icelandic region during spring rather than winter, as well as minimum height anomalies during the winter and fall seasons (instead of summer). On the other hand, CCSM4, which was the worst in simulating the observed oceanic features of the AMO, exhibits a reasonable seasonal cycle on the atmospheric front (the strongest among all models): it displays maximum (minimum) anomalies in winter (summer), but of greater amplitude in comparison to observations, including an enhanced subtropical/tropical response, which is not seen in observations. The respective atmospheric features in ECHAM6/MPI-ESM-

LR are marginally stronger than in GFDL-CM3, with a seasonal cycle of similar skill to the one in GFDL-CM3, however: maximum anomalies are displayed in winter, with the strongest minimum anomalies being observed during fall. Finally, in UKMO-HadCM3 a seasonal cycle similar to the one in observations is discerned, but of much weaker amplitude: in fact, the response is so weak that it is characterized by normal conditions during the defined summer season. At last, it is worth noting that none of the models captures the fall wave pattern over North America and parts of the northeastern Atlantic; this is important as low and mid-tropospheric geopotential height variability can be related to winds and low-level circulation that is associated with moisture transport and is therefore conducive to more efficiently understanding and modeling hydroclimate changes and extreme events (i.e. droughts) over the US Great Plains and other regions (Ruiz-Barradas and Nigam 2005).

2.3.5 AMO and Precipitation Patterns

The main rainy season for the majority of the domain examined in this study occurs in the months of summer and fall, but among these seasons, fall is the season during which we observe the greatest association between the AMO and regional geopotential height anomalies, as well as circulation and surface climate features. The warm phase of the AMO is characterized by prominent SST anomalies that are linked to important precipitation anomalies in observations (Fig. 2.9, upper panel). The structure of the fall- SST anomalies in the mid-latitudes and northern tropical Atlantic[5] is similar to the all-season regressed anomalies (Fig. 2.1) but with a stronger

---

[5] The AMO-related SST anomalies in the North Atlantic are minimum in spring, a time when the SST anomalies over the northern tropical Atlantic reach the maximum extension and have the largest impact on the Northeast region of Brazil rainy season (not shown). This is all reminiscent of the so called interhemispheric mode.

maximum in the mid-latitudes. The associated precipitation anomalies display a general decrease in rainfall over the US, which is particularly prominent in the eastern half[6]; furthermore, a rainfall decrease is noted over the western and southeastern portions of northern South America. On the other hand, enhanced rainfall is observed over Central America, the Guinean zone in Africa[7], southern Europe, and the UK (Fig. 2.9, upper panel). The previously studied 500mb anomalous geopotential height pattern (ridge-trough-ridge) that is present during fall, is a good example of how mid-level circulation anomalies generate precipitation anomalies over land: the wave pattern of high-low-high at the 500mb pressure level over the US enables the generation of near-the-surface, northerly winds, reduced moisture transport and a low-level subsidence that can subsequently lead to enhanced dryness over the central and southeastern US.

As far as the models are concerned, fall SST anomalies manifest some similarities to the all-season regressions, with some distinct differences, however, due to the seasonality of the phenomenon (Fig. 2.9, middle and lower panels). As in the case of the all-season regressions, models (with the exception of GFDL-CM3) tend to place the maximum SST anomalies in the North Atlantic too far to the east of the Labrador Sea, in comparison to observations. CCSM4 is the only model with no subtropical/tropical extension of the SST anomalies; on the other hand, GFDL-CM3 and ECHAM6/MPI-ESM-LR demonstrate a similar-magnitude, subtropical/tropical extension of the North Atlantic SST anomalies (as in observations), a phenomenon that was absent from the all-season regressions. Finally, UKMO-HadCM3's fall SSTA structure appears similar to the all-season one, remaining unable to match the observed magnitude of the SSTA extension into the Tropics.

---

[6] The influence of the AMO in central US rainfall is considerably less extensive in summer than in fall (not shown).

[7] The impact of the AMO on regional rainfall over Africa depends on the season. As noted above, the Guinean zone is affected in fall, but the Sahelian zone to its north is most affected in summer (not shown).

Now the four models remain challenged when focusing on their ability to capture the vast hydroclimate features that are related to the warm phase of the AMO, during fall. The observation- based, reduced rainfall in central and eastern US is only partially captured by ECHAM6/MPI-ESM-LR and in a minimum way by UKMO-HadCM3. On the other hand, the reduced rainfall over South America is broadly captured by GFDL-CM3 in its western portion, with CCSM4 and UKMO-HadCM3 having only a few hints of the reduced rainfall over its southeastern part. The broad region of enhanced rainfall over the Guinean zone in Africa is also problematic for all four models; while GFDL-CM3 portrays decreased rainfall over the region, accompanied with enhanced rainfall over the Sahelian zone (extending too far to the north, however, with respect to observations), the other three models are unable to simulate the magnitude and spatial extent of these precipitation anomalies.

2.3.6 AMO Related, Surface Air Temperature Variability

Given the decadal scale of the phenomenon, it is also important to identify AMO's signal in surface air temperature, in order to differentiate it from the man-induced impact on regional temperatures. Regressions of the AMO indices on surface air temperature during fall are shown in Figure 2.10. Warming associated with the warm phase of the AMO in observations is manifested over the western US, the Labrador Peninsula and southern Greenland, large parts of Europe, northwestern Africa, as well as western South America (Figure 2.10, upper panel). The AMO influence on surface air temperature is seasonally dependent: while fall is the season with the most extended warming over the domain used for the current study, winter is the season when warming appears to be maximum over eastern US and Canada, with a generalized cooling observed over Europe, except for a region of intense warming occurring over the Scandinavian Peninsula (not shown).

AMO-related fall surface air temperature anomalies are not being fully captured, in magnitude or position, by any of the four model simulations employed here. The warming over western US is only timidly shown by ECHAM6/MPI-ESM-LR. The remaining models (with the exception of CCSM4) weakly portray the warming over the Labrador Peninsula and southern Greenland. In addition, the broad extension of the warming over northwestern Africa is also weakly and sparsely simulated by all four models. Finally, the warming over western South America appears exaggerated by GFDL-CM3, with an extent that surpasses the one in observations, while ECHAM6/MPI-ESM-LR depicts the warming in a muted way.

2.4 Summary and Discussion

The basin-wide, sea surface temperature variability known as the Atlantic Multidecadal Oscillation and its signature on surface and sub-surface fields, as well as its impact on the climate of neighboring continents, has been analyzed in this study, in an effort to construct an integrated view of the phenomenon. North Atlantic SSTs exert a significant and oftentimes predictable influence on climate, with devastating socioeconomic impacts, such as the ones derived from multi-year drought and enhanced rainfall incidents over N. America. Thus, the characterization of the AMO is of vital significance in assessing the efficiency of decadal climate prediction experiments of current state-of-the art models participating in the CMIP5 project. The need for a proper incorporation of such low frequency natural variability phenomena, such as the AMO, has been noted in past studies (Meehl et al. 2009, Hurrell et al. 2009, Nigam et al. 2011) and is essential for a better attribution of natural and human-induced effects in model projections of present and future climate events.

A clarified description of AMO's spatiotemporal structure and evolution emerges from century-long observations. The mature warm phase of the smoothed AMO is associated with warm anomalies in the North Atlantic mid-latitudes over the sub-polar gyre region and the Labrador sea and a secondary maximum of warm anomalies in the northern tropical Atlantic (also see Nigam et al. 2011). The relative magnitude of the maximum SST anomalies is inverted when the analysis is confined to the second half of the 20th century, despite the fact that the structure remains unchanged.

A period of 58 years is inferred for the smoothed AMO from observations, which is smaller than other estimations in the 65-75 years range (e.g., Enfield et al. 2001, Sutton and Hodson 2005); these other estimates are based on the use of heavy smoothing of the area-averaged anomalies, as compared with the 1-2-1 binomial filter used here. Spectral analysis shows that oscillations in the 70-80 year range are dominant in the observed smoothed AMO index, but are combined with oscillations in the 30-40 year range and shorter periods. Models, however, underestimate the life span of the phenomenon by increasing variability in the 10-20 year range, to the extent that it becomes more dominant than variability in the 70-80 year range.

Sea surface temperature anomalies are shown to be associated with vertically-integrated heat content anomalies (sfc-400m) that evolve coherently in time, as well as vertically integrated (sfc.-50m) salinity anomalies - particularly the positive anomalies developing over the Labrador Sea and the negative ones off of the US coast. While this configuration of SST/salinity/heat content anomalies over the deep water formation region of the sub-polar gyre points toward a more active thermohaline circulation during the warm phase of the AMO, the cold phase of the

AMO suggests a weaker thermohaline circulation and fresh water anomalies, similar to the ones evolving during Great Salinity Anomaly events (as noted in Slonosky et al. 1997). An atmospheric signal associated with the N. Atlantic low-frequency variability is also discerned from observations, when looking at regressions of the seasonal AMO index on the respective 500 mb geopotential height field. Regional geopotential height anomalies, including both the weather noise that is forcing the SSTA evolution, as well as the atmospheric feedback to the Atlantic impact, appear stronger in winter and weaker during summer, while persisting, however, throughout the entire year, as noted in Kushnir et al. 2010 and Wang et al. 2010. The fall season appears to be of critical importance as far as the interactions between the AMO and the regional surface climate of the adjacent continents are concerned; an anomalous wave pattern extending from North America to eastern Europe is linked to reduced (enhanced) rainfall over large portions of the Americas (western Africa, over the Guinean region) and generalized warming over the western Americas, Greenland, Europe and northwestern Africa, during that season.

The four CMIP5 models examined in this study capture the focus of North Atlantic SSTAs in the mid-latitudes, while moving, however, the maximum anomalies further to the east than observations indicate, and while remaining, in general, unable to portray the extension of same-sign anomalies into the tropics, during the pre- and post-mature phases of the AMO. The characteristic period of the AMO remains underestimated with an error range between 6 (UKMO-HadCM3) and 18 years (ECHAM6/MPI-ESM-LR). UKMO HadCM3 appears to be most successful in simulating the AMO's spatial evolution and variability around the mature phase (±4 years). Furthermore, the models tend to associate N. Atlantic SST anomalies (especially the warm ones) with the sfc-400m heat content variations (as seen in observations), while appearing more challenged, however, when simulating the observed temporal evolution of these anomalies close to the mature phase of the AMO. At the mature phase, GFDL-CM3 and UKMO-HadCM3 portray some of the observed features (of the SST and heat content fields), such as the contrasting warm anomalies over the sub-polar gyre region (Labrador Sea and Davis Strait) and the cold anomalies off of the eastern US coastline. GFDL-CM3 is the only model capturing the spatial distribution of the salinity anomalies, while exaggerating however their spatial extent off of the US coast. In general, GFDL-CM3 exhibits the most favorable oceanic description associated with the AMO, while CCSM4 exhibits the least favorable one (CCSM4 salinity and heat content anomalies are the weakest among models, and have the least resemblance to the observed structure).

None of the four models employed in this study is able to capture the anomalous circulation pattern that is seen in observations during the fall season. CCSM4, despite its unsuccessful depiction of the AMO-related, oceanic features, displays a more realistic atmospheric structure (in comparison to the other models) via the seasonality of the 500mb geopotential heights. Regarding the fall hydroclimate characteristics associated with the AMO, ECHAM6/MPI-ESM-LR is best at representing the reduced rainfall over the US (although it is deficient in capturing its spatial extent); over the same region, UKMO-HadCM3 displays similar to the observations but of minimum amplitude features, whereas CCSM4 and GFDL-CM3 are unable to reproduce the reduced precipitation impact, manifesting normal and increased precipitation patterns, respectively. Finally, regarding the AMO-related, surface air temperature anomalies, GFDL-CM3 demonstrates the strongest, warming signal among the models but is unable to capture the warming over western North America, while ECHAM6/MPI-ESM-LR marginally captures the extensive warming; CCSM4 and UKMO-HadCM3 are only able to represent the warming over northwestern Africa, in a minimum way. One can therefore argue that representation of low frequency variability and its associated hydroclimate structure remains challenged in these simulations and that there is an uneven (incoherent) progress noted between these models and their respective predecessors (their CMIP3 versions), as noted in recent studies (Ting et al. 2011; Ruiz-Barradas et al. 2012). Furthermore, the models remain unable to efficiently depict a holistic perspective of the AMO-related oceanic and atmospheric features. More research is therefore necessary to unravel potential mechanisms that are critical in low frequency variability structure and evolution in the North Atlantic and that might not be well represented in models, hindering thus their ability to more efficiently portray the observed, AMO signature. Such mechanisms include the ability of climate models (or lack thereof) to a. efficiently produce the Pacific basin link of the Atlantic impact (Ting et al. 2011, Guan and Nigam 2008) - this connection has been noted in several studies in the past (Enfield and Mayer 1997; Ruiz-Barradas et al. 2000, Latif 2001), b. to capture the role of the ocean in long-term variability (i.e. by efficiently simulating its surface and sub-surface structure), c. to understand and simulate the coupling between the ocean and the overlying atmosphere and the connection between circulation features, weather noise (momentum, heat, freshwater) and ocean-induced surface fluxes (via the atmospheric response to SST evolution) and regional hydroclimate (for instance, the relation between the recent N. American drought events of 2012 in the context of North Atlantic and equatorial and northern Pacific impact). Some research questions that arise from the current study and are yet to be fully answered include: a. the connection between the region of origin, the excitation mechanism and the propagation of salinity anomalies between the Arctic and N. Atlantic basins (Sundby and Drinkwater 2007) and the ways in which these anomalies relate to low-frequency, sea surface temperature variability in the N. Atlantic and b. the relative contribution of the surface versus deeper layers of the ocean to the increase in oceanic heat content and the ways in which this relates to the spatiotemporal pattern of multi-decadal, N. Atlantic SST variability.

2.5 Conclusions

To conclude, we believe that our analysis sheds light on the structure and evolution of the low-frequency AMO, while also inciting supplemental interest for AMO’s footprint on both surface and sub-surface variables. The modeled AMO image that emerges via the newly released historical simulations demonstrates limited success, particularly on the continental climate impact front. A greater focus on building AMO’s sub-surface signature, throughout the entire North Atlantic basin and its co-variability with salinity and meridional overturning circulation fluctuations could potentially help improve the incorporation of AMO-related mechanisms in climate models. However, this may not be enough to substantially advance the way the atmosphere responds to mid-latitude sea surface temperature anomalies in the models. Without a proper incorporation of low-frequency natural variability in climate simulations, the accuracy of both climate projections under climate change scenarios and decadal predictions remains compromised.

Table 2.1 Ensemble members used for Figs. 2.1-3, 2.7 and 2.8. The bold numbers indicate the model runs that were used for the remaining figures 2.4-2.6.

IPCC CMIP5 20th CENTURY MODELS	RUNS USED
GFDL-CM3	1,**2,3**,4,**5**
CCSM4	**1**,2,3,4,5,6
ECHAM6/MPI-ESM-LR	**1,2,3**
UKMO-HadCM3	**1,2**,3,**4,5,6,7,8,9**

Table 2.2 Correlations of the smoothed AMO indices between model simulations of the 20th century climate and the observed smoothed AMO index for the period 1900-1999. The statistical significance of the regressions is assessed via a two-tailed Student's t-test at the 5% level, using an effective sample size Ne=25 (degrees of freedom). Critical correlation is found to be (R_c) equal to **0.38**. Correlations above this value are statistically significant.

IPCC AR5 20th Century Simulations	Run1	Run2	Run3	Run4	Run5	Run6	Run7	Run8	Run9
GFDL-CM3	0.40	0.51	0.49	0.56	0.75	-	-	-	
CCSM4	0.14	0.14	-0.39	0.29	-0.03	-0.18	-	-	
ECHAM6/MPI-ESM-LR	-0.47	-0.1	0.01	-	-	-	-	-	
UKMO-HadCM3	0.38	0.36	-0.23	0.11	0.48	0.23	-0.14	0.39	0.29

Table 2.3 Timescale in years of the smoothed AMO indices estimated from their autocorrelation functions displayed in Fig. 2.2. If considering the anomalies of a given sign decay until the autocorrelation reaches a certain value, this defines a quarter of the period of the phenomenon. If the zero line is used to define the period of the smoothed AMO index, its period is given in the zero-Crossing column, but if the 1/e line is used instead, the period is given under the 1/e-crossing column.

MODEL/OBS	**Zero-Crossing**	**1/e-crossing**
Observations	58	44
GFDL CM3.1 (4 runs)	48	22
CCSM4 (6 runs)	50	16.5
ECHAM6 (3 runs)	40	15.5
HadCM3 (9runs)	52	16.5

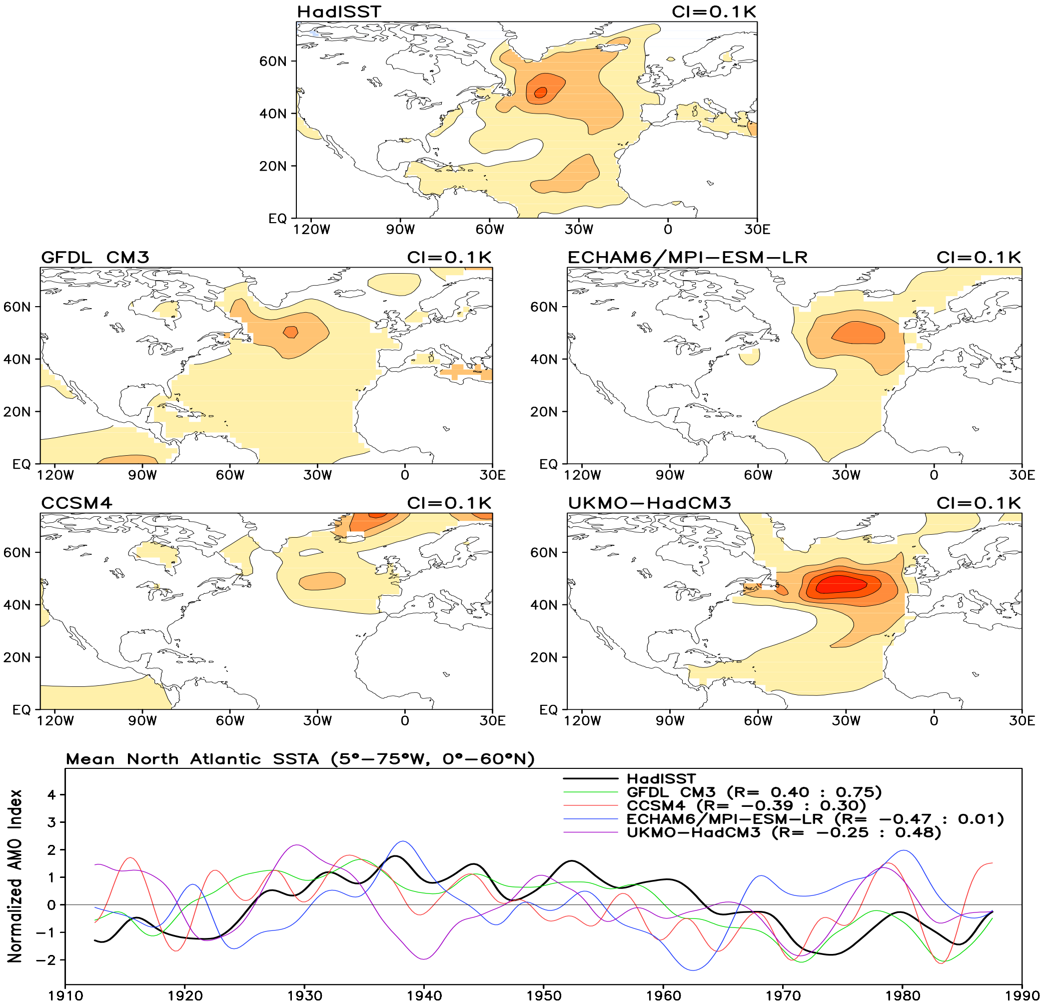

Figure 2.1 All-season regressions of standardized smoothed AMO indices on SSTs for the winter 1900 – fall 1999 period. Regressions for the models are calculated for each ensemble member separately and then an average is computed for each model. Red/blue shading denotes positive/negative SST anomalies; contour interval is 0.1K. The indices are constructed by first calculating a spatial average of SST anomalies over the (5°-75°W, 0°-60°N) region and then detrended, using the least squares method. The indices are finally smoothed by applying a 1-2-1 binomial filter 50 times and normalized by using their standard deviation. Regressions are shown after 5 applications of smth9 in the GRADS plotting software. **Bottom Panel:** Observed HadISST smoothed AMO index and other four model-derived smoothed AMO indices which have the highest correlations, R, with the observed index: GFDL-CM3, Ensemble 5 (R=0.75), UKMO-HADCM3, Ensemble 4 (R=0.56), ECHAM6/MPI-ESM-LR, Ensemble 3 (R=0.01) and CCSM4 Ensemble 4 (R=0.29). The correlation range for the different ensembles within each model is shown adjacent to the model's name.

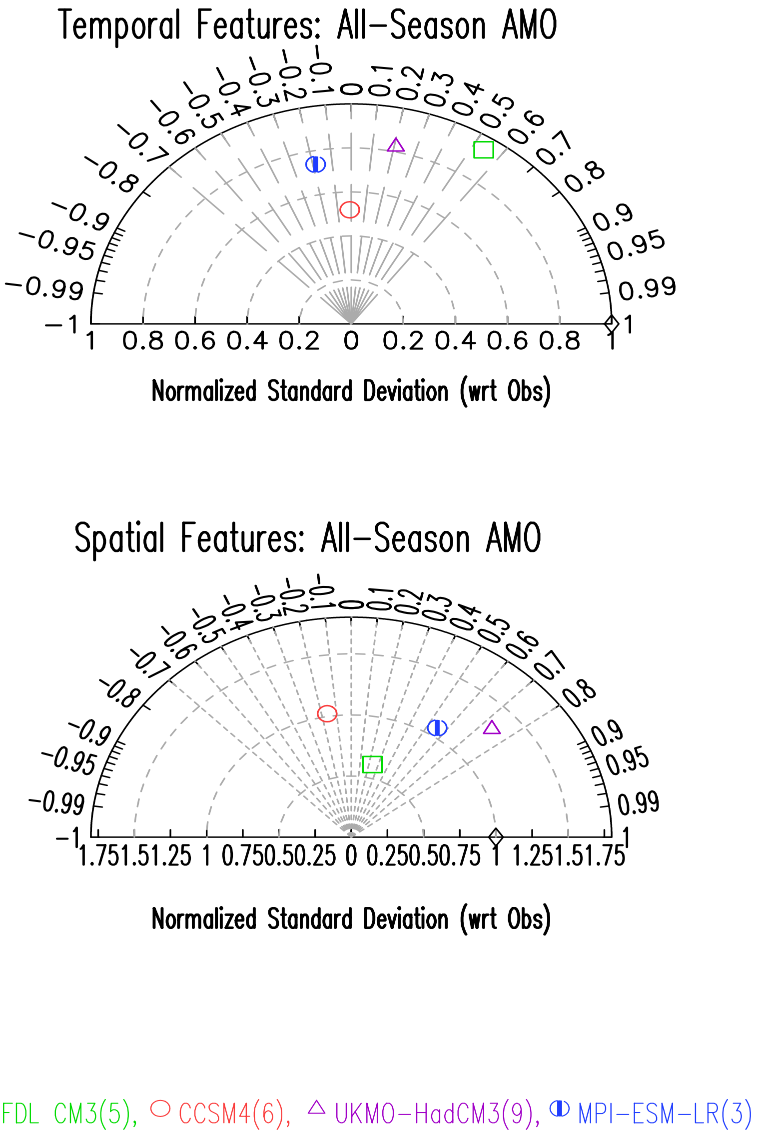

Figure 2.2: Taylor diagrams of smoothed AMO indices and their regressions from observations and CMIP5 climate model simulations for the period 1900-1999. Normalized standard deviations, correlations and standard deviations are calculated between observations and the different ensembles' mean for each model, to compare the temporal and spatial variability and correlations between observations and the four models. The temporal (spatial) standard deviations are normalized with respect to the observed, temporal (spatial) standard deviation of 0.17K (0.46K). The horizontal (x axis) shows normalized standard deviation values, whereas the arc-part of the diagrams shows the respective correlation values. Each model is shown in a different color (see legend) and the number in parenthesis denotes the number of ensembles used from each model to generate the mean standard deviation and mean correlation.

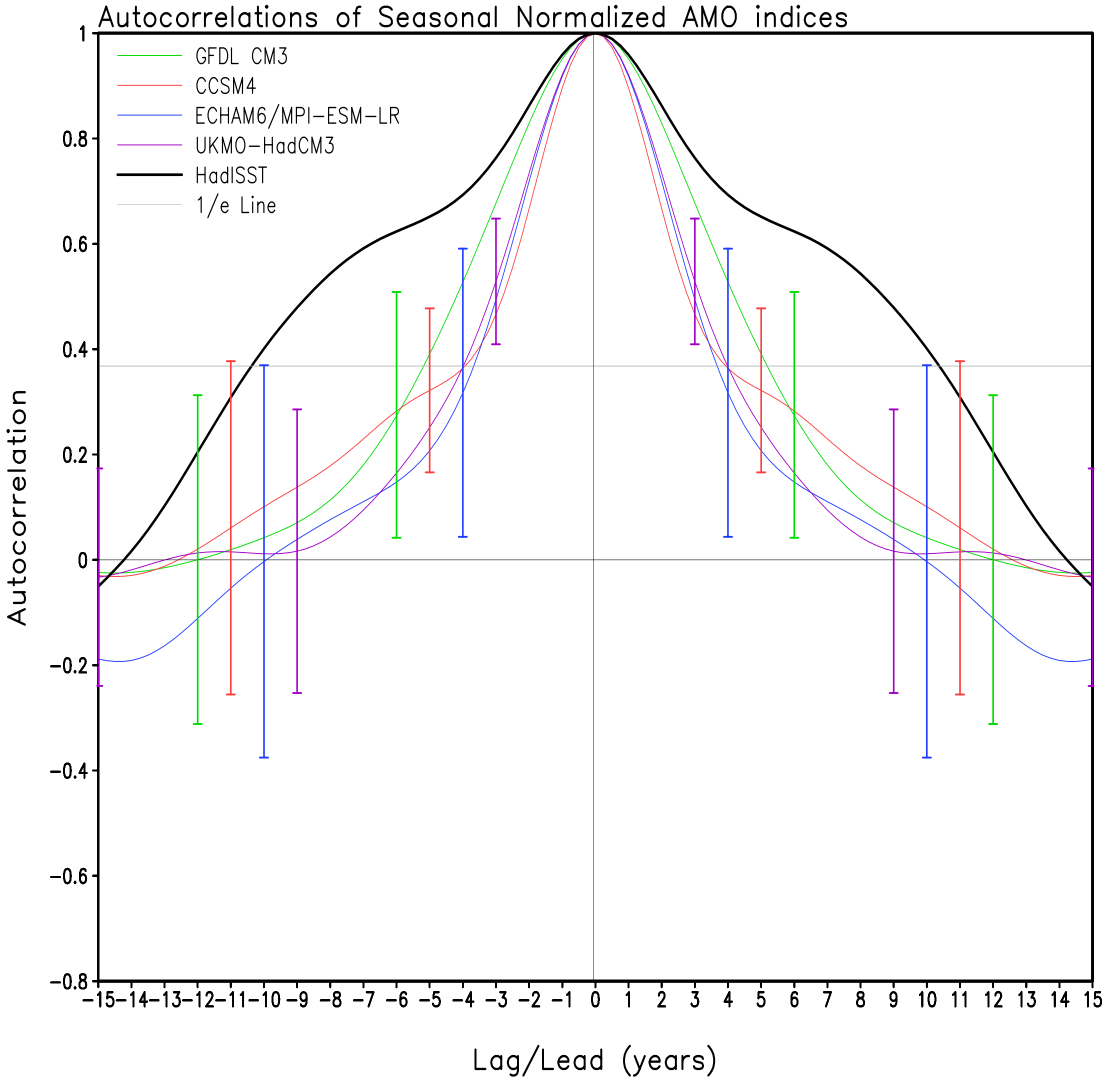

Figure 2.3: Standardized smoothed AMO indices are calculated for each ensemble member of each model; subsequently, their corresponding autocorrelations are calculated and a mean autocorrelation is finally computed and displayed. Autocorrelations are calculated for t-15 to t+15 years and compared to the autocorrelation time series derived from observations (black line). The standard deviation (SD) error bars among the different autocorrelations are also calculated and drawn here, to indicate the dispersion of the individual ensemble autocorrelations for each model from the ensemble mean.

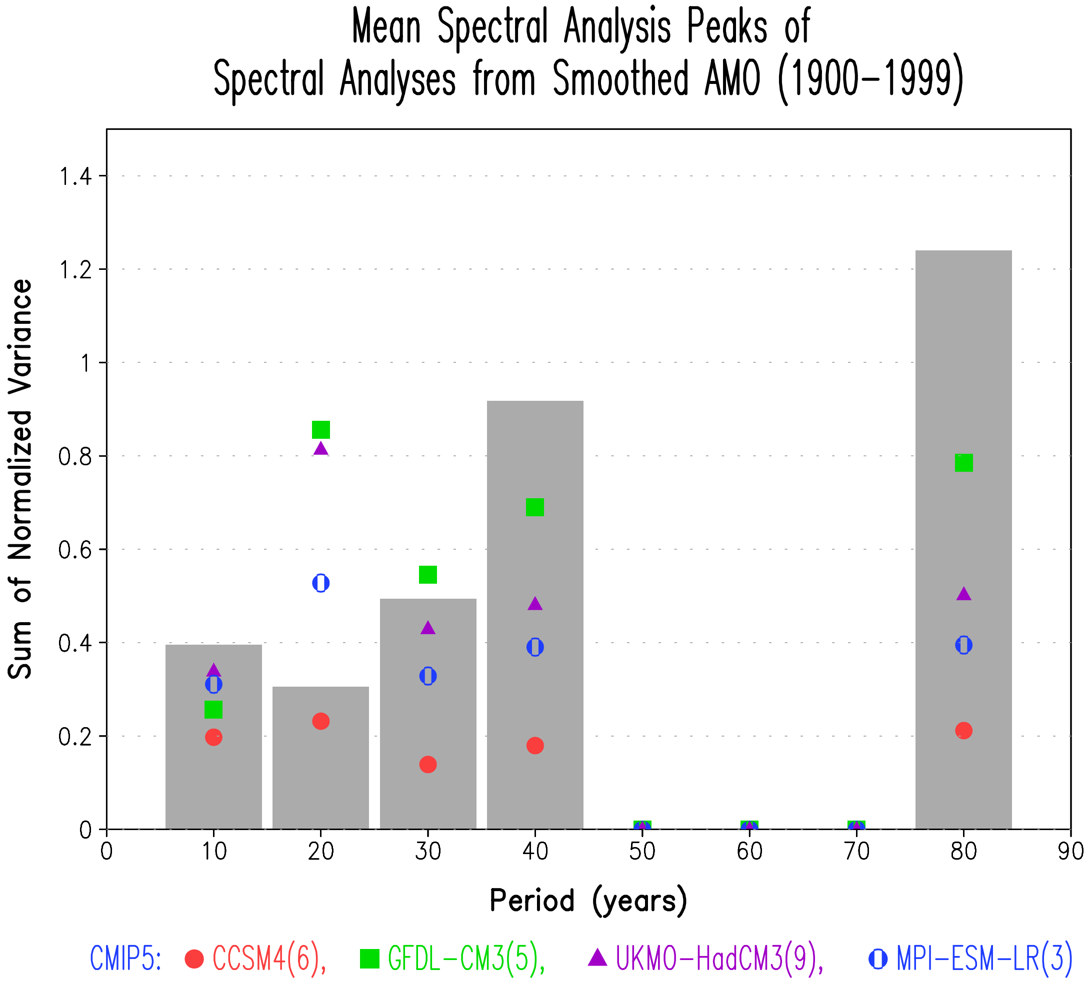

Figure 2.4: Histogram of mean spectral analysis' peaks from smoothed AMO time series. A histogram of the dominant frequency peaks derived from a spectral analysis of the mean smoothed, AMO indices derived from the four models are shown for the January 1900 – October 1999 time period. The sum of normalized variance is shown on the y axis and the dominant periods in years are shown on the x-axis. The dominant frequencies for each model are shown in different colors (see legend) and the number in parenthesis denotes the number of ensembles used from each model to generate the mean spectrum (corresponding to the mean, model-derived AMO time series.)

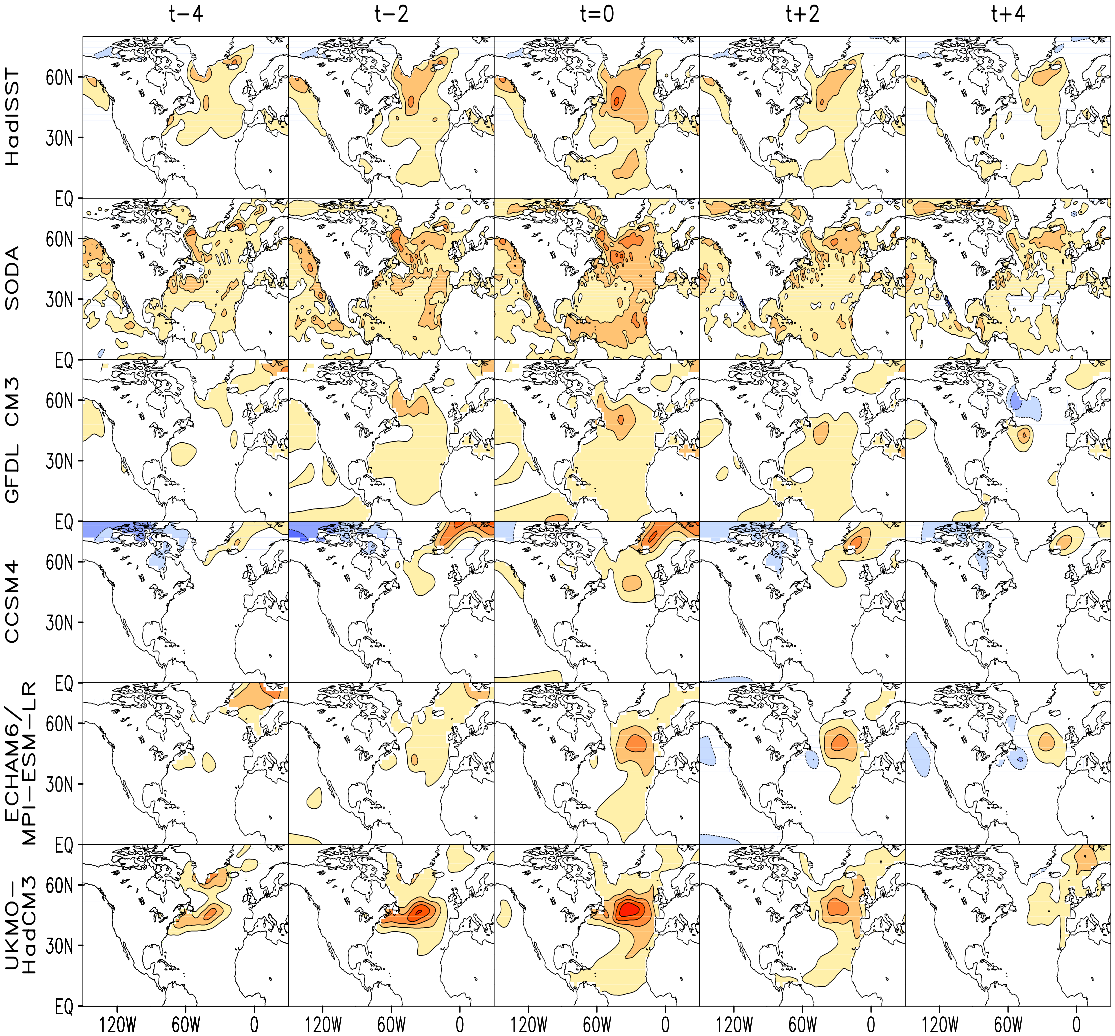

Figure 2.5 All-season lead/lag regressions of the smoothed AMO indices on SSTs for the winter 1900 – fall 1999 period: SST anomalies are shown four years before and after the mature phase: pre-mature conditions are shown 4 years (t-4 column) and 2 years (t-2 column) before the mature phase (t column), while post-mature conditions are shown 2 years (t+2 column) and 4 years (t+4 column) after the mature phase. The upper two rows show regression anomalies from observations by HadISST and by the SODA 2.2.4 ocean reanalysis. The remaining rows show the related AMO SST anomalies from model simulations of the 20th century climate from GFDL CM3, CCSM4, ECHAM6/MPI-ESM-LR and UKMO-HadCM3. Regressions are calculated for each ensemble member separately and a mean regression is subsequently computed. Red/blue shading denotes positive/negative anomalies; contour interval is 0.1K. Regressions are shown after 5 applications of the smth9 function in the GrADS plotting software.

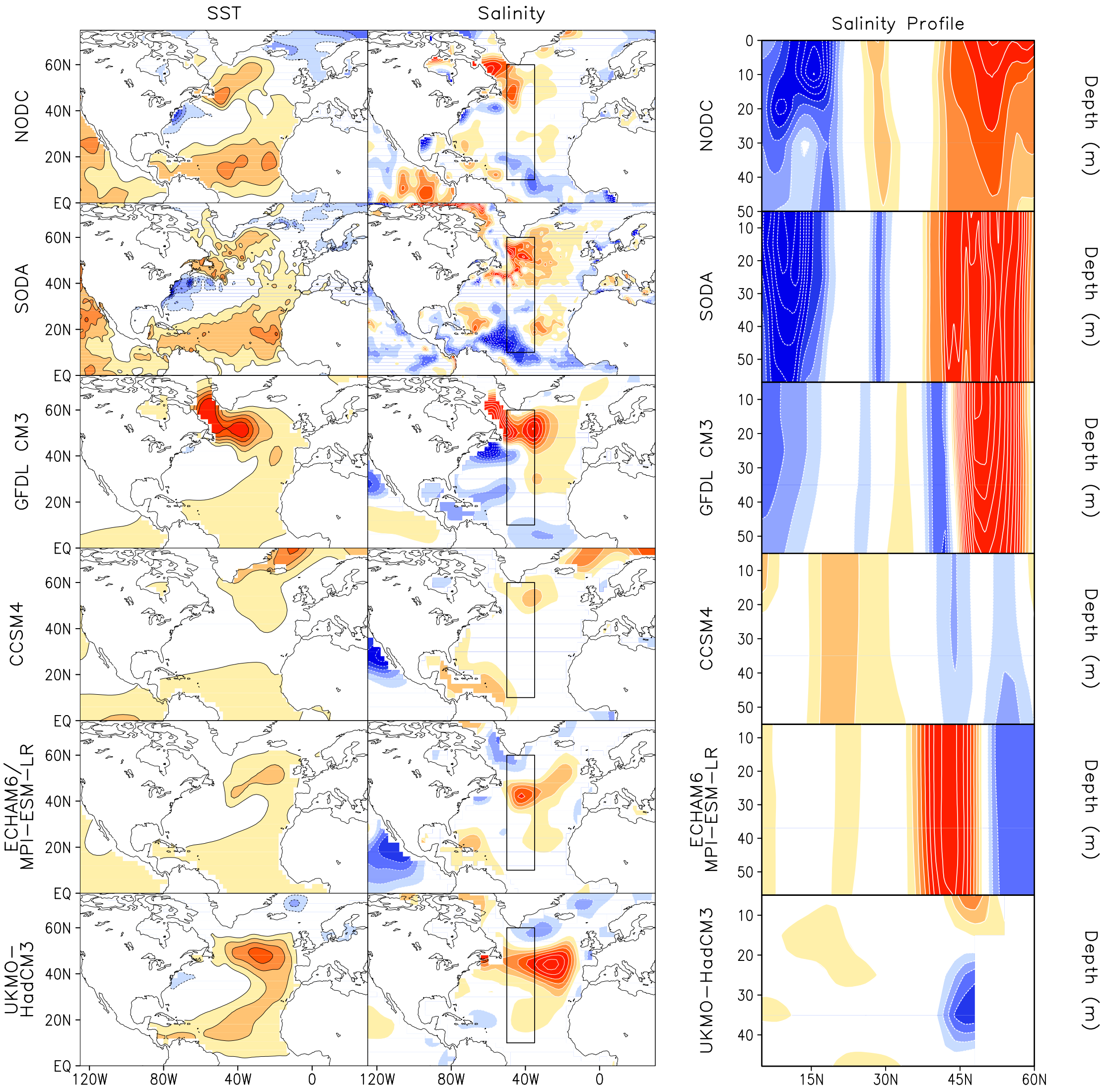

Figure 2.6 All-season regressions of the smoothed AMO indices on SST and salinity for the period winter 1955 – fall 1999. Regressions on SSTs are displayed in the left-hand side panels, on the vertically averaged (0-50m) salinity field are displayed on the central panels, while on salinity latitudinal profiles are shown on the right-hand side panels. Regressions are calculated for each ensemble member separately and a mean value is subsequently computed and shown. Red/blue shading denotes positive/negative SST and salinity anomalies. The contour intervals for the maps are 0.1K and 0.2ppt for SST and salinity anomalies, respectively, having skipped the zero contour line. The right-hand side panels show latitude-depth cross-sections of the longitudinally averaged (35°-50°W) regressions of the AMO index with the 3-dimensional salinity field; the contour interval is 0.1ppt. The upper two rows show regression anomalies from observations by NODC and SODA 2.2.4 ocean reanalysis. The remaining rows show the related AMO salinity anomalies from model simulations of the 20th century climate from GFDL-CM3, CCSM4, ECHAM6/MPI-ESM-LR and UKMO-HadCM3.

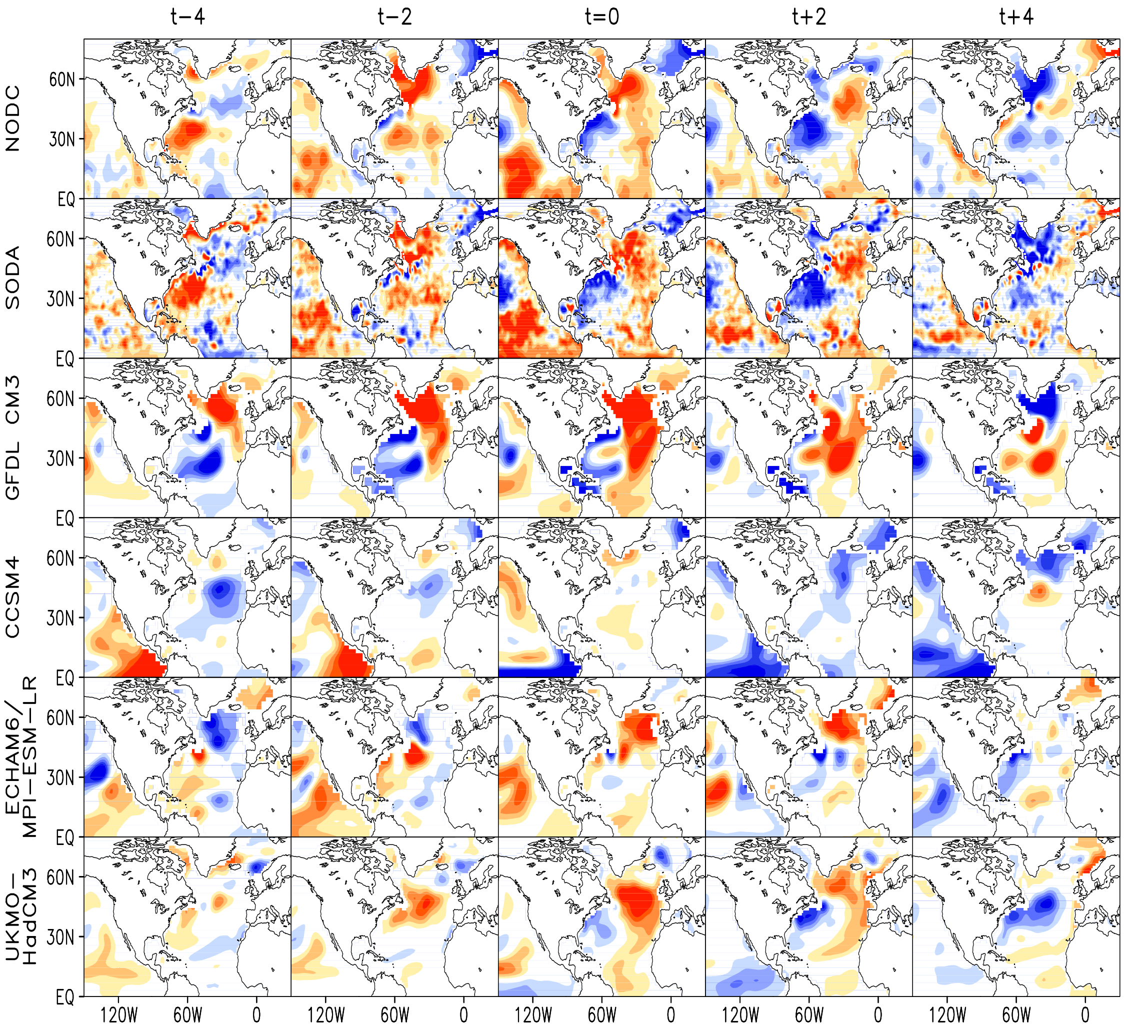

Figure 2.7 All season regressions of the smoothed AMO indices on (0–400m) vertically integrated, detrended ocean heat content for the period, winter 1955 – fall 1999. The upper two rows show regression anomalies from observations by NODC and by the SODA 2.2.4 ocean reanalysis, and the remaining rows show the related AMO heat content anomalies from model simulations of the 20th century climate from GFDL CM3, CCSM4, ECHAM6/MPI-ESM-LR and UKMO-HadCM3. Model regressions are calculated for each ensemble member separately, and a mean value is subsequently computed and plotted here. Red/blue shading denotes positive/negative anomalies; the contour interval is 5×10^{7} J/m^{2}. Regressions are displayed after five applications of the smth9 function in the GrADS plotting software.

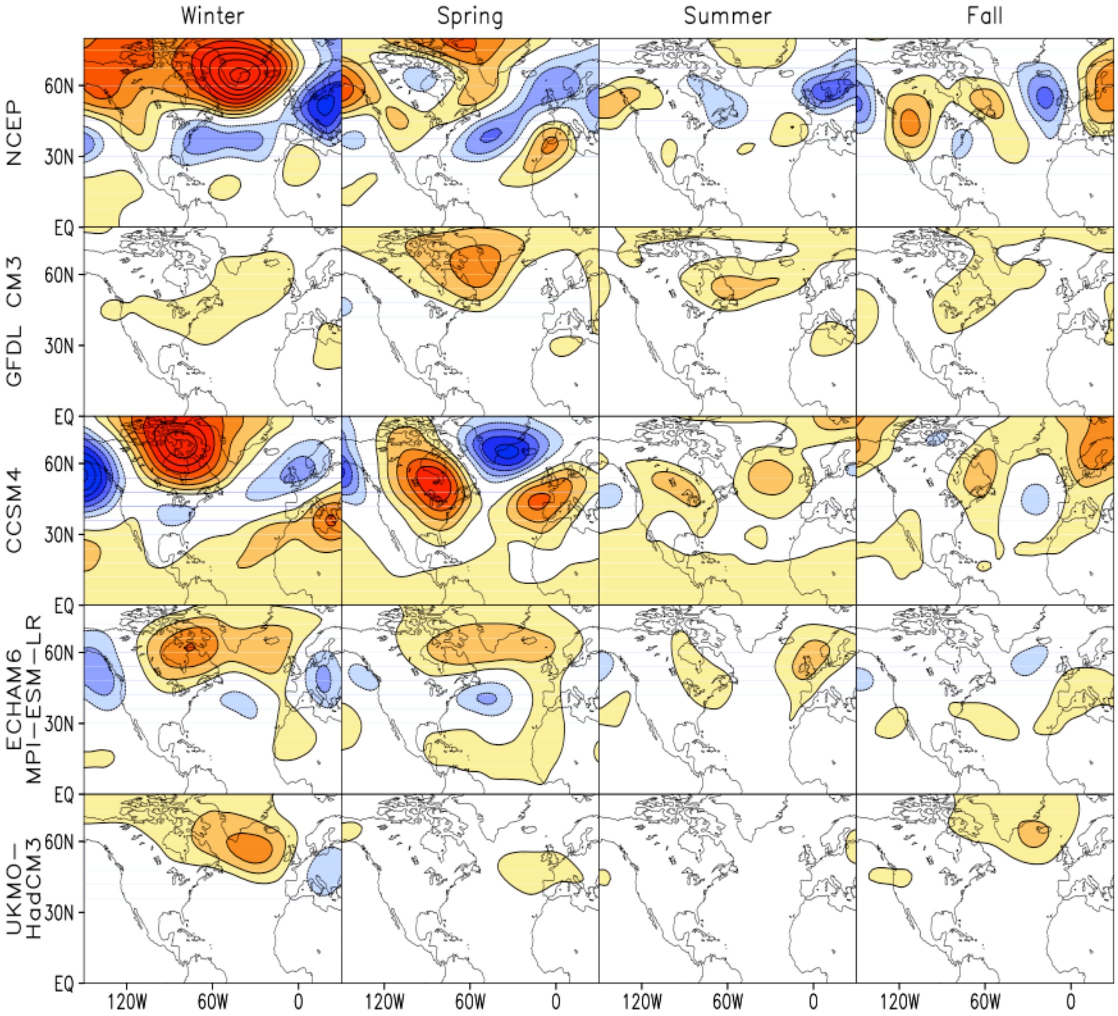

Figure 2.8 Seasonal regressions of the smoothed AMO indices on 500 mb geopotential heights for the period winter 1949 – fall 1999. The upper row was generated by regressing seasonal smoothed AMO indices from the HadISST data set on the NCEP reanalysis heights. The remaining rows show the related AMO height anomalies from model simulations of the 20th century climate from GFDL CM3, CCSM4, ECHAM6/MPI-ESM-LR and UKMO-HadCM3. Model regressions are calculated for each ensemble member separately and a mean value is subsequently computed and plotted here. Red/blue shading denotes positive/negative anomalies; contour interval is 4m. Regressions are shown after two applications of the smth9 function in the GRADS plotting software.

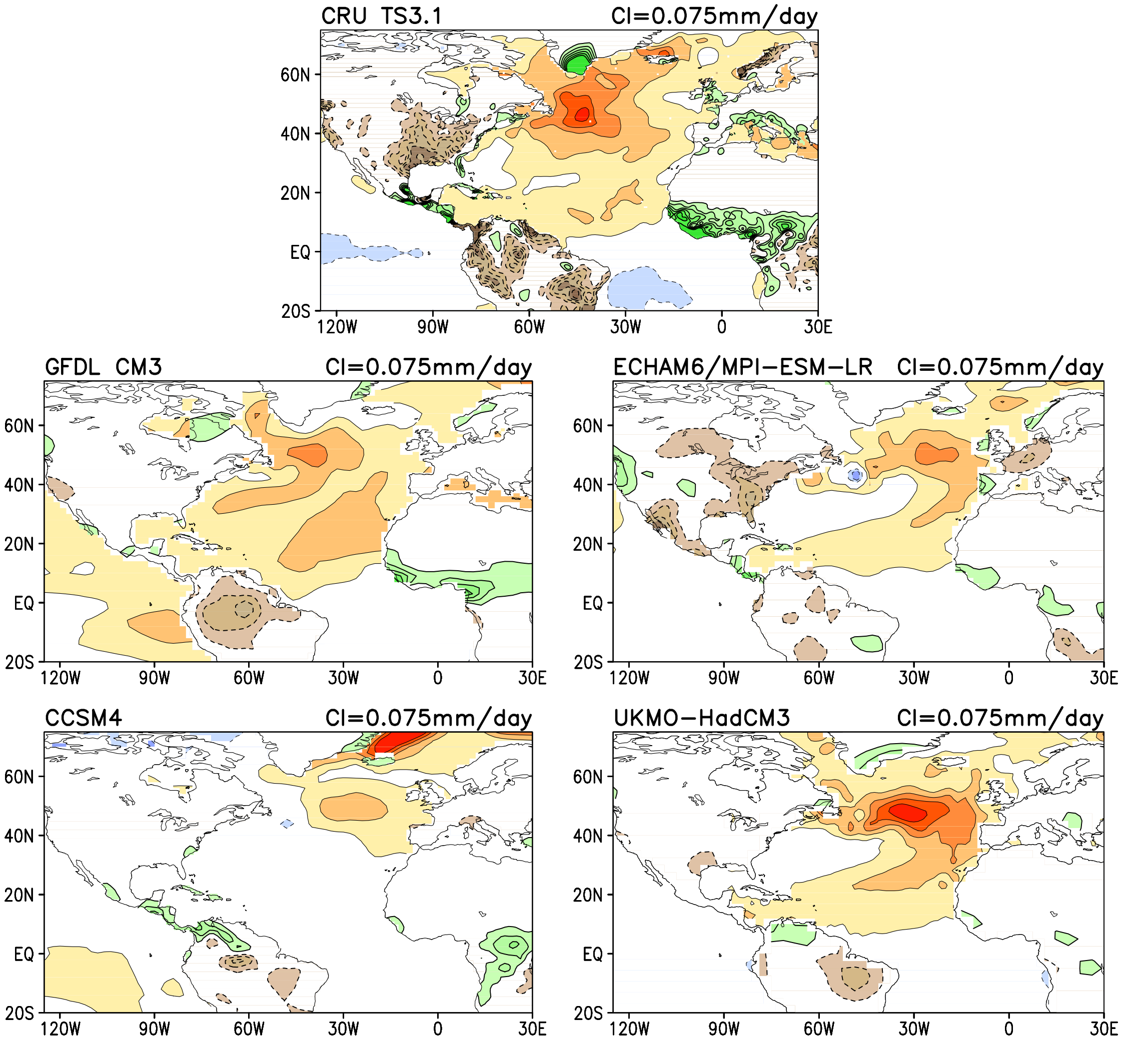

Figure 2.9 Fall regressions of smoothed AMO indices on SST and precipitation for the winter 1901– fall 1999 time period. The upper panel shows the regression of the observed HadISST smoothed AMO index on its own SSTs and CRUTS3.1 precipitation. The remaining panels show the related AMO SST and precipitation anomalies from model simulations of the 20th century climate from GFDL-CM3, CCSM4, ECHAM6/MPI-ESM-LR and UKMO-HadCM3. Regressions are calculated for each ensemble member separately and an average is subsequently calculated and shown here. Blue/red and green/brown denote positive/negative anomalies for SST and precipitation fields, respectively; contour intervals are 0.075mm/day and 0.1K, respectively.

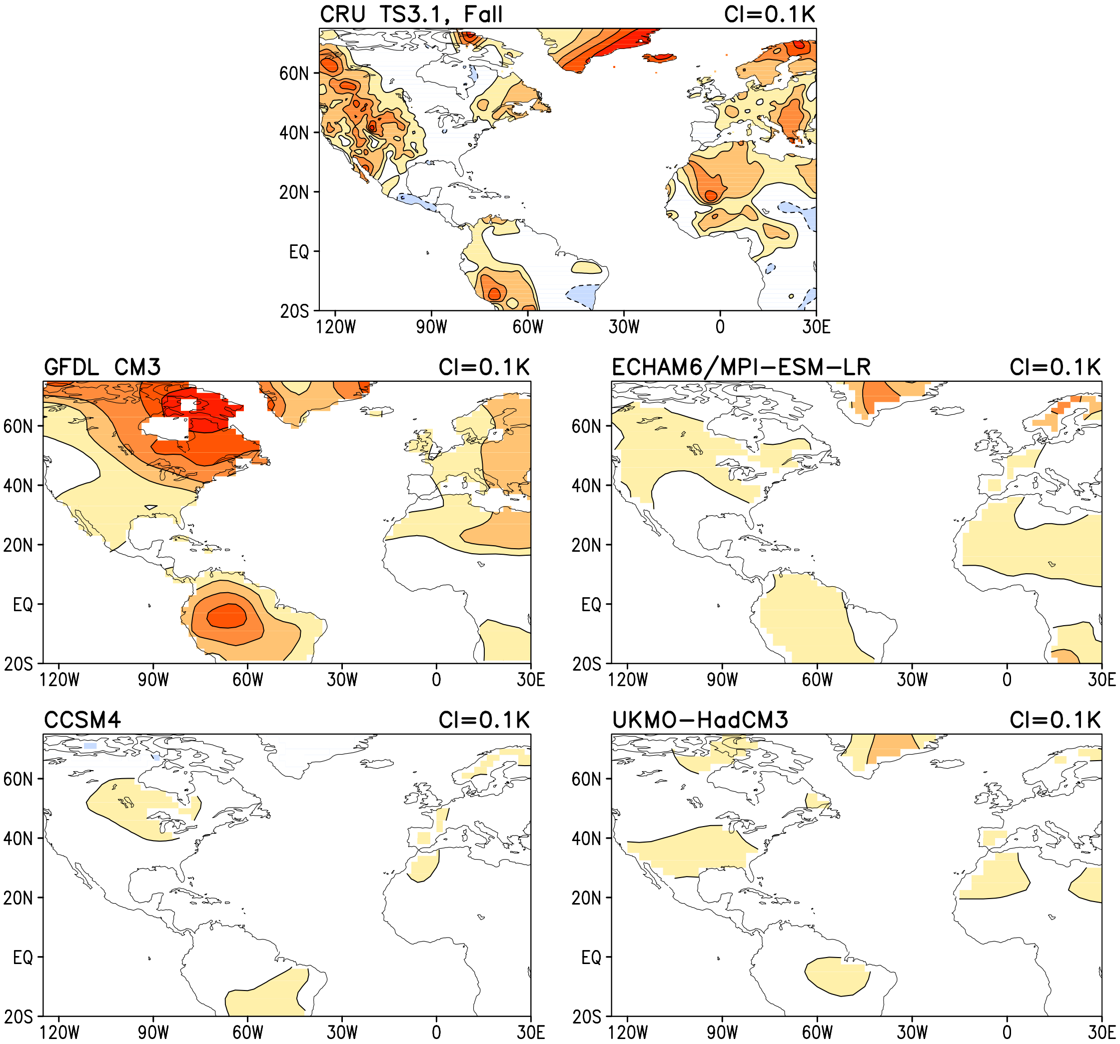

Figure 2.10 Fall regressions of smoothed AMO indices on surface air temperature for the winter 1901–fall 1999 time period. The upper panel shows the regression of the observed HadISST smoothed AMO index on CRUTS3.1 surface air temperature. The remaining panels show the related air temperature anomalies from model simulations of the 20th century climate from GFDL CM3, CCSM4, ECHAM6/MPI-ESM-LR and UKMO-HadCM3. Regressions are calculated for each ensemble member separately and an average is subsequently calculated and shown here. Blue/red denotes positive/negative anomalies; contour interval is 0.1K.

Chapter 3: The Atlantic Multidecadal Oscillation in 20th Century Climate Simulations: Uneven Progress from CMIP3 to CMIP5

3.1 Introduction

Decadal climate prediction has taken a prominent role for the first time in the experiments of the Coupled Model Intercomparison Project Phase 5 (CMIP5; Taylor et al. 2011). The need for useful decadal predictions has been made not only from scientific papers (e.g., Meehl et al. 2009, Hurrell et al. 2010), but also from the impact of climate-related events like the current melting of the Greenland glaciers, the ongoing drought in northern Mexico and central US, as well as past decade-long droughts over the same region in the recent 20th century and over western Africa. Properties of the components of the climate system determine the time scales of the variations within the system: days to weeks for the atmosphere, weeks to years for the biosphere, months to decades for the ice, and months to decades to centuries for the oceans. Thus, perturbations to the slower climate system components can produce climate variability at these long timescales. Therefore, if one aspires to have reliable decadal predictions, climate models have to properly incorporate the processes that give rise to decadal variability in specific components of the climate system, in addition to the mechanisms through which these processes impact the surface climate affecting human societies.

Phenomena with defined decadal variability that climate models must properly include are the Pacific Decadal Oscillation (PDO, Mantua et al. 1997) and the Atlantic Multidecadal Oscillation (AMO, Enfield et al. 2001, Guan and Nigam 2009). However, it is not always clear what drives a given phenomenon, as it is the case of the AMO. One of the most accepted theories relates the Atlantic SST fluctuations to variations in the Atlantic Meridional Overturning Circulation (Latif et al. 2004; Medhaug and Fuverik 2011, Zhang et al. 2013), but one of the newest and most controversial relates the SST variations to fluctuations in atmospheric concentrations of anthropogenic and natural aerosols (Evan et al. 2009; Booth et al. 2012). Decadal control of hydroclimate from the AMO over North America and Africa is one of the main reasons to worry about having this phenomenon properly incorporated in climate models. Multi‐year, summer and fall droughts over North America and Africa have been observationally linked to decadal sea surface temperature (SST) variability in the Atlantic (e.g., Enfield et al. 2001; Ruiz-Barradas and Nigam 2005; Wang et al. 2006; Zhang and Delworth 2006; McCabe et al. 2008; Shanahan et al. 2009; Kushnir et al. 2010; Nigam et al. 2011).

The focus of this chapter is not to unveil the nature of the AMO or assess its predictability but to provide a comparison of the capabilities of the current state-of-the-art models in simulating the AMO. In other words, the main goal of this paper is to assess the way models from the CMIP3 and CMIP5 projects depict the AMO in the 20th century climate, an important component of decadal variability on the climate system, and a key element for decadal prediction. This evaluation will provide elements to find out if AMO-like decadal variability, of great importance for hydroclimate variability over North America and Africa, has improved in the latest CMIP5 models over those from the CMIP3 project. A detailed analysis of the spatiotemporal features of the AMO in the atmosphere and ocean, and its hydroclimate impact over North America, in CMIP5 models has already been carried out (Kavvada et al. 2013), so the focus here will be on the model inter-comparison and assessment against observations.

3.2 Datasets

The present analysis uses SSTs and precipitation from observations and simulations of the 20th century climate from models participating in CMIP3 and CMIP5 projects for the Intergovernmental Panel on Climate Change (IPCC). Observed SST data comes from the U.K. Met Office's Hadley Centre Sea Ice and Sea Surface Temperature dataset, version 1.1 (HadISST 1.1, Rayner et al. 2003). On the other hand observed precipitation is obtained from the University of East Anglia Climate Research Unit high resolution gridded data analysis of station data, version 3.1 (CRUTS3.1; Mitchell and Jones 2005). While the main analysis is carried on with a selected set of models, a complementary analysis is done with an extended set of models. The models used in the main analysis come from leading international climate research centers from the U.S., NCAR and NOAA's GFDL, the U.K. Met Office Hadley Centre, and the German Max Plank Institute for Meteorology (MPI-M). On the other hand, the larger set of models used in the complementary analysis are models that participated in the CMIP3 project and were also used in an updated version in the CMIP5 project. The historical simulations analyzed are run by imposing changing conditions, consistent with observations, which may have included: atmospheric composition, due to both anthropogenic and volcanic influences, solar forcing, emissions or concentrations of short-lived species and natural and anthropogenic aerosols as well as land use.

a. CMIP3 Models

The CMIP3 models analyzed include: 1) version 3 of NCAR's Community Climate System Model CCSM3 (Collins et al. 2006, and additional references in the CCSM special issue in the Journal of Climate), 2) version 2.1 of NOAA's GFDL Coupled Climate Model GFDL-CM2.1 (Delworth et al. 2006), 3) version 3 of U. K. Meteorological Office and Hadley Centre Coupled Climate Model UKMO-HadCM3 (Gordon et al. 2000; Pope et al. 2000), and 4) Germany's version 5 of European Centre Hamburg Model/MPI-M's Ocean Model

ECHAM5/MPI-OM (Roeckner et al. 2003, Marsland et al. 2003). The 20th century climate simulations started from the late 19th century and went through 1999 or 2000 with no apparent standardization of the time series of atmospheric composition greenhouse gases and atmospheric aerosols. The CMIP3 models used in the complementary analysis are listed in Table 1.

b. CMIP5 Models

The CMIP5 models analyzed include: 1) version 4 of NCAR's Community Climate System Model CCSM4 (Gent et al. 2011), 2) version 3 of NOAA's GFDL Coupled Climate Model GFDL-CM3 (Donner et al. 2011; Griffies et al. 2011), 3) UKMO Hadley Centre Global Environment Model version 2, I nits Earth System configuration, UKM-HadGEM2-ES (Collins et al. 2008), and 4) Germany's version 6 of European Centre Hamburg Model/MPI-M's Earth System Model, Low Resolution version, ECHAM6/MPI-ESM-LR (Raddatz et al. 2007; Marsland et al. 2003). The historical 20th century climate simulations started from the mid 19th century and finished in 2005, but unlike the CMIP3 simulations, the forcing was standardized for all models. Note that the CMIP5 versions of the models from NCAR and GFDL are updated versions of the CMIP3 models, but the CMIP5 versions of the models from UKMO and MPI are Earth System models. The CMIP5 models used in the complementary analysis are listed in Table 1.

c) Methods

The current analysis is based on seasonal data. Seasons are defined in terms of their boreal hemisphere 3-month means: winter, December-February; spring, March-May; summer, June-August; and fall, September-November. Seasonal anomalies were created by extracting the long-term mean (1900-1999). AMO indices were generated by taking the spatial average of SST anomalies in the Atlantic domain (5° to 75° West and 0° to 60° North), and then linearly detrended by using the least squares method; the index is then smoothed by applying a (1-2-1) binomial filter 50 times which preserves the decadal-to-interdecadal variability. Smoothed versions of the AMO index are generated for observations and each ensemble member available for the models. Lead/lag regression and correlation analyses are then used to investigate the spatial and temporal structures associated with the smoothed AMO in observations and model simulations of the 20th century climate. Model results are presented as the mean of the all-season regressions/correlations of the different ensemble members in each model, and are compared against all-season regressions/correlations from observations in section 3 and the first part of section 4, while summer and fall regressions/correlations are used in the second part of section 4. The number of ensembles used in each of the CMIP3 and CMIP5 models is: 8 for CCSM3 and 6 for CCSM4, 3 for GFDL-CM2.1 and 5 for GFDL-CM3, 2 and 4 for UKMO-HadGEM2-ES, and 4 for ECHAM5/MPI-OM and 3 for ECHAM5/MPI-ESM-LR. The complementary analysis with the extended set of models relies on the first ensemble member only of the historical simulations.

3.3 Features of the Atlantic Multi-decadal Oscillation

3.3.1 Structure

The warm phase of the mature AMO is characterized by maximum SST anomalies in the north Atlantic, to the south of Greenland and to the east of Newfoundland, and a secondary maximum on the northern tropical Atlantic in front of the Western African coasts; the secondary maximum is enclosed for a subtropical/tropical extension of the anomalies over the north Atlantic (Fig. 3.1a) that reaches the Caribbean Sea and leaves under normal conditions the Gulf of Mexico and western Sargasso Sea. The focus of the SST anomalies on the region of the sub-polar gyre, where major water masses pass from/to higher latitudes, suggests these anomalies may be more than the response to atmospheric conditions and be linked to subsurface ocean processes involving heat content and salinity anomalies as well (Kavvada et al. 2013). Thus, a reasonable depiction of the observed structure of the AMO by the models may suggest that the underlying processes that generate the AMO are reasonably incorporated.

Analysis of the structure of the AMO-related SST anomalies in the 20th century climate simulations from the CMIP3 models (Fig. 3.1b, d, f, h) emphasizes that the region with the largest anomalies are in the Labrador Sea. This region, that is to the northwest of the region of maximum anomalies in observations, has maximum SST anomalies in all models, however, the maximum has an eastward extension in CCSM3 that is placed to the south of Iceland over the northern half of the sub-polar North Atlantic; in any case, the models are misplacing the maximum SST anomalies found in observations. Only CCSM3 depicts negative anomalies in front of Newfoundland over the region of the Grand Banks, which are not present in observations. It is also noted that models tend to put SST anomalies to the north of Iceland, which are not present in observations[8]. The secondary maximum of SST anomalies in the northern tropical Atlantic found in observations is absent from the model simulations, however, the models produce the subtropical/tropical extension of the northern anomalies with a varied degree of success. While the southward extension in CCSM3 and GFDL-CM2.1 models barely reaches the 20°N line, it reaches the deep tropics and Caribbean Sea as in observations in UKMO-HadCM3 and ECHAM5/MPI-OM models. It is interesting to note that while the tropical Pacific has climatological conditions (or close to zero anomalies) associated to the AMO in observations, SST anomalies over that region from the model simulations are extensive.

The Labrador Sea focus in the structure of the AMO-related SST anomalies seen in CMIP3 models is reduced in CMIP5 models (Fig. 3.1c, e, g, i); this is more evident in CCSM4.

---

[8] The region is data-sparse but not data-void, and the quality of the data when compared with in-situ data is reasonable according to an analysis made by Hughes et al. (2009; *J. Mar. Sci., 66 (7): 1467-1479*).

Models also tend to place the maximum SST anomalies farther to the east than observed; these anomalies are in the range of the observed anomalies. Except for the GFDL-CM3 model, all the other models show negative anomalies in front of Newfoundland over the region of the Grand Banks which are no existent in observations. The anomalies to the north of Iceland have also been reduced in the CMIP5 models, except by the CCSM4 model which present the largest anomalies over the Greenland Sea. The structure of the northern tropical Atlantic anomalies still have marked deficiencies; while CCSM4 has no tropical component at all, and ECHM6/MPI-ESM-LR has reduced its extension, GFDL-CM3 has extended it into the deep tropical Atlantic, and UKMO-HadGEM2-ES has increased its magnitude as in observations. The fictitious tropical Pacific signature of the AMO in the models has increased in GFDL-CM3 and CCSM4, but it is reduced in the other two models. From these models, UKMO-HadGEM2-ES seems to be in better accord with observations, while CCSM4 is the one with the most obvious deficiencies.

3.3.2 Characteristic period

The period of the AMO indices can be obtained via their autocorrelation functions (Fig. 3.2). The crossing of the observation-based AMO autocorrelation (thick black line) with the zero line shows a dominant period of approximately 56 years (the intersection point allows for an estimate of the time series' half-period). The continuous colored lines representing the mean autocorrelation for each of the CMIP5 models (Fig. 3.2a) display a general underestimation of the AMO period: 40 years in ECHAM6/MPI-ESM-LR, 44 years in GFDL-CM3, and 52 years in CCSM4; however the period is 68 years in UKMO-HadGEM2-ES. It is interesting to point out that if the temporal comparison is done using the time needed for the autocorrelation to decay to 1/e of its value models are farther apart from observations: while observations indicate a 44 year de-correlation period, models are grouped together around the 16-24 years range! Note that these estimations of the time scale of the smoothed AMO tend to be shorter than others using heavier filters that maximize the low frequency modulation of the decadal pulses (e.g. Enfield et al 2001, Ting et al. 2011).

Comparison of the AMO autocorrelations from CMIP5 models with the corresponding from the CMIP3 models does not show a marked difference between the associated periods of the AMO (Fig.3.2 b-e), except in the case of the UKMO models whose period went from a 16-year period in the CMIP3 model to a 68-year period in the CMIP5 model. De-correlation times decreased in the CMIP5 versions of the NCAR, GFDL and MPI models, while it increased in the UKMO models.

The integrated view of the autocorrelation of the smoothed AMO indices can be expanded via the spectral analysis of the time series (Fig. 3.3) to provide a deeper insight into what may be behind the variability in observations and models. It is clear that both sets of CMIP3 and CMIP5 models underestimate low frequency variability in the 70-80 and 30-40 year ranges while overestimate variability in the 10-20 year range. Variability in the 10-20 year range has increased, and exceeded that variability from observations, in GFDL, UKMO and MPI CMIP5 models with respect to the CMIP3 models, but not in the NCAR models. Conversely, variability in the 70-80 years range has increased, but it is still under that variability from observations in GFDL, UKMO and MPI CMIP5 models with respect to the CMIP3 models, but decreased significantly in the NCAR models.

3.3.3 Evolution

A more complete view of the surface features of the AMO is reached by displaying the evolution of the SST anomalies around the mature stage via all-season lead/lag regressions (Fig. 3.4). During the warm phase of the AMO positive SST anomalies emerge from the Davis Strait and Labrador Sea in observations (Fig. 3.4a) and follow a southeastward propagation in the higher mid-latitudes and a subsequent southwestward displacement toward the lower latitudes which track the east branch of the subtropical gyre as time progresses until they reach maximum amplitude and extension in the mature state; the subtropical anomalies are weaker than those in the mid-latitudes, with a local maximum developing off the western Africa coasts. Anomalies gradually decrease in magnitude, with the signal first dissipating over the tropical latitudes and subsequently further to the north.

The structure and evolution around the mature stage of the SST anomalies associated with the warm phase of the AMO in the models have only a general agreement with observations and have marked differences between the CMIP3 and CMIP5 versions. All modeled SST anomalies associated with the AMO reach maximum values and extension at the mature phase, as in observations, without consideration of the type of model. However the magnitude of the anomalies and structure in general do not match those from observations. The CMIP5 version of the NCAR model, CCSM4, changed dramatically the magnitude and structure of the SST anomalies displayed by the CMIP3 version of the model, CCSM3 (Fig. 3.4b, c): while CCSM3 has a similar propagation to the one in observations originating over the Labrador Sea and anomalies reach a maximum extension on the northern tropical Atlantic, the anomalies from CCSM4 seem to originate over the Greenland Sea and never reach tropical latitudes. The CMIP5 version of the GFDL model, GFDL-CM3, also exhibits notable changes of the AMO-related SST anomalies when compared with the corresponding from its CMIP3 version, GFDL-CM2.1 (Fig. 3.4d, e): while GFDL-CM2.1 has little propagation of the anomalies over the Labrador Sea and anomalies reach tropical latitudes in the mature stage, the anomalies from GFDL-CM3 are smaller, propagate more actively in the mid-latitudes, and reach tropical latitudes 2 years before and after the mature stage similarly to observations, but their structures have some differences, including anomalies over the eastern tropical Pacific and negative anomalies over the Labrador Sea 2 and 4 years after the mature state which are not seen in observations. The CMIP5 version of the UKMO model, UKMO-HadGEM2-ES, similarly to the GFDL model, also has some changes on the SST anomalies when compared with those from its CMIP3 version, UKMO-HadCM3 (Fig. 3.4f, g): while UKMO-HadCM3 has anomalies with little change over the Labrador Sea, with anomalies that reach the tropical latitudes in the mature state and linger just off the African coasts 2 years after it, the anomalies from the UKMO-HadGEM2-ES are smaller, and propagate in the mid-latitudes and reach the tropical latitudes 2 years before and after the mature stage as in observations; UKMO-HadGEM2-ES is the only model that reproduces the magnitude of the observed AMO-related anomalies in the tropical North Atlantic as well as their structure in the mature stage and 2 years before and after it, although negative anomalies are evident over the Greenland Sea which are not displayed in observations. The CMIP5 version of the MPI model, MPI-ESM-LR, is not the exception and also has changes when the AMO-related anomalies are compared with those from the CMIP3 version, ECHAM5/MPI-OM (Fig. 3.4h, i): while ECHAM5/MPI-OM has the largest anomalies over the Greenland Sea and anomalies reach the tropical latitudes only in the mature stage, the MPI-ESM-LR reduces the anomalies over the

Greenland Sea, increases the anomalies in the mid-latitudes but reduces the extension of the tropical anomalies in the mature state.

3.4 Assessment

An objective way to compare the temporal and spatial features of the smoothed AMO indices and regressed precipitation and SST anomalies can be achieved by the use of Taylor diagrams (Fig. 3.5). Comparison of the temporal features of the AMO indices (Fig. 3.5a) indicates the majority of the models have poor correlation with observations and under-estimate the observed variability, except for the GFDL and the UKMO-HadGEM2-ES models. While the CMIP5 version of the GFDL model improves the variability of the smoothed AMO index from the CMIP3 version, it slightly decreases the correlation with the observed index; on the other hand, the CMIP5 version of the UKMO model greatly improves the variability as well as the correlation with the observed index.

Comparison of the spatial variability from the regressed precipitation and SST anomalies on the smoothed AMO indices is carried on summer and fall, the seasons when the AMO impacts the most the regional hydroclimate. It is clear that the models are not up to the task of simulating the impact of the regional hydroclimate yet (Fig. 3.5b, c): the spatial variability of the precipitation anomalies is under-estimated, and the spatial correlations with observations are under 0.3 over the North American domain in either season. On the other hand, the spatial variability and spatial correlations in the SST anomalies improve from CMIP3 to CMIP5 versions of the MPI and UKMO models, being the most successful the UKMO-HadGEM2-ES model in both seasons; the most dramatic degeneration, is in the NCAR models.

While the previous analysis uses the ensembles available of four models, the ensuing comparison uses the first ensemble of a larger sample of CMIP3 and CMIP5 models. Smoothed indices for the AMO were created for each of the models and regressed on SST and precipitation in summer and fall. Regressions from observations, multi-model means and their differences with observations are shown in Fig. 3.6a-c. Observations indicate that SST anomalies increase in the midlatitudes from summer to fall but decrease in extension in the northern tropical Atlantic. Concomitant to the seasonal evolution of oceanic anomalies is the deficit in precipitation over North America in summer, which expands and intensifies from northern Mexico to the US in fall; on the other hand, western Africa experiences wet conditions in both seasons. Both CMIP3 and CMIP5 multi-model means do not simulate the intensification of SST anomalies over the Mid Atlantic from summer to fall, and are colder than observations indicate, especially in fall. The associated impact on the regional precipitation anomalies in the multi-model means show increased precipitation in summer and a very weak deficit in precipitation in fall over North America. In short, the multi-model means show wetter North America and drier western Africa than observations in summer and fall.

Spatial correlations of the observed and simulated anomalies do not indicate an improvement of the CMIP5 vs. CMIP3 models (Fig. 3.6d, e). While there are some CMIP5 models that perform better than their CMIP3 comparison models (refer to Table 1 to identify the models), their multi-model means have smaller spatial correlations with observations than those from the CMIP3 multi-model means: 0.43/0.58 for SST anomalies (over the oceanic domain displayed in the Fig. 3.6) from CMIP5/CMIP3 multi-model mean in summer, and 0.38/0.58 in fall; 0.13/0.14 and 0.06/0.25 for precipitation anomalies (over the continental domain to the west of 60°W shown in Fig. 3.6) from CMIP5/CMIP3 in summer and fall respectively.

It is worth to point out that in the context of North American hydroclimate, particularly over the central US, models are unable to properly simulate the impact of the AMO in summer and fall. This is in spite of having the broad oceanic features of the AMO, better in CMIP3 than in CMIP5 multi-model means. Independently of the version, this problem seems to be related to the inability of the models to modify the regional low level circulation that modulates the moisture fluxes affecting the region (Kavvada et al 2013, Sheffield et al 2013).

3.5 Concluding Remarks

Decadal variability in the climate system from the AMO is one of the major sources of variability at this temporal scale that climate models must aim to properly incorporate because its surface climate impact on the neighboring continents. This issue has particular relevance for the current effort on decadal climate prediction experiments been analyzed for the IPCC in preparation for the Fifth Assessment Report. The current analysis does not pretend to investigate into the mechanisms behind the generation of the AMO in model simulations, but to provide evidence of improvements, or lack of them, in the portrayal of spatiotemporal features of the AMO from the previous to the currents models participating in the IPCC. If climate models do not incorporate the mechanisms associated to the generation of the AMO (or any other source of decadal variability like the PDO) and in turn incorporate or enhance variability at other frequencies, then the models ability to simulate and predict at decadal time scales will be compromised and so the way they transmit this variability to the surface climate affecting human societies.

The current analysis of historical simulations of the 20th century climate from state-of-the-art climate models from the CMIP5 and CMIP3 projects assesses how these models portray the structure of the evolving SST anomalies associated with the AMO and its variability. In addition, spatial variability of SST and precipitation anomalies associated with the AMO is evaluated for summer and fall. Comparisons with observations help to establish if the CMIP5 models are improving over their previous CMIP3 versions.

The mature stage of the warm phase of the AMO has evolved from the CMIP3 to the CMIP5 version but it has not progressed consistently through the models. Observations show that the AMO has a maximum of SST anomalies to the south of Greenland and a secondary maximum in the northern tropical Atlantic. The renditions of the AMO from CMIP3 models have maximum SST anomalies over the Labrador Sea with a secondary maximum to the east of Greenland and weak anomalies over the tropics. The CMIP5 versions of the models in general reduce the double maximum of SST anomalies over the mid-latitudes of the Atlantic to a one maximum southeastward of Greenland and varied representations of the maximum in the tropics: while CCSM4 has no extension over the tropical Atlantic, and GFDL-CM3 highlights more the eastern tropical Pacific than the tropical Atlantic, UKMO-HadGEM2-ES portrays the best the AMO structure, followed by the MPI-ESM-LR.

The evolution of the SST anomalies associated with the warm phase of the AMO in models reaches maximum values and extension at the mature stage as in observations but have marked differences in magnitude and structure between the CMIP3 and CMIP5 versions. Anomalies seem to originate along the Davis Strait and Labrador Sea before the mature stage in observations, then propagate southeastward and reach maximum magnitude south of Greenland and extend into the tropics in the mature stage; in the post-mature stages the anomalies over the tropics start to abate and the anomalies in the mid-latitudes move to the east of Greenland. While the CMIP3 models seem to have this general displacement of anomalies originating along the Davis Strait and Labrador Sea, their CMIP5 versions seem to originate over the Greenland Sea. As in the case of the analysis of the mature stage, the evolution of anomalies is captured poorly by CCSM4, and in a better way by UKMO-HadGEM2-ES.

The evolution of the SST anomalies associated with the AMO is closely related to the characteristic period of the AMO in the models. While observations indicate a period close to 56 years, the NCAR, GFDL and MPI CMIP3 and CMIP5 models underestimate this value with periods in the 40-52 years range; the UKMO models however go from an extremely low period close to 16 years in the CMIP3 version, to an overestimation close to 68 years. On the other hand, if the period is judged using the time at which correlations decay to a 1/e of its value, all models underestimate the 44-year value suggested from observations with periods in the 16-24 years range. It is clear that both sets of CMIP3 and CMIP5 models underestimate low frequency variability in the 70-80 and 30-40 year ranges, while overestimating variability in the 10-20 year range. Variability in the higher 10-20 year range increases from CMIP3 to CMIP5 in three of the models surpassing the variability in this range from observations.

The temporal variability and correlations of the AMO indices from the majority of the models are low when compared with the observed AMO index. The exceptions are for the indices from the CMIP5 versions of the GFDL and the UKMO models with variability close to observations and correlations slightly above 0.5. The success of the CMIP5 version of the GFDL model in these assessments of the AMO indices is surprising considering that the structure and the evolution of the SST anomalies were not the best among the models, as it was the case for the CMIP5 version of the UKMO model.

On the other hand, comparison of the observed spatial variability and spatial correlations of the regressed precipitation and SST anomalies of the AMO indices in summer and fall indicates that models are not up to the task of simulating the impact on the regional hydroclimate. On the other hand, the spatial variability and correlations in the SST anomalies improve from CMIP3 to CMIP5 versions of the MPI and UKMO models, being the most successful the UKMO-HadGEM2-ES model in both seasons; the most dramatic degradation is in the NCAR models.

Analysis of AMO regressions from the extended set of models reveals no improvements in the oceanic and hydroclimate impact associated with the AMO from CMIP3 to CMIP5 projects. Pattern correlations with observed SST and precipitation anomalies are smaller in CMIP5 than in CMIP3 models in summer and fall.

The current chapter does not provide evidence on why the models perform in the way they do but suggests that that the spurious increase in high 10-20 year variability from CMIP3 to CMIP5 models may be behind the unsatisfying progress in depicting the spatiotemporal features of the AMO. This problem, coupled with the inability of the models to perturb the regional low-level circulation, the driver of moisture fluxes, seem to be at the center of the poor representation of the hydroclimate impact of the AMO.

Table 3.1 Models used in the complementary analysis from CMIP3 and CMIP5 projects (Fig. 3.6)

CMIP3 Model	**CMIP5 Model**	**Model # used in Fig. 3.6d,e)**	**Institution**
---	BCC-CSM1.1	1	Beijing Climate Center, China Meteorological Administration, China
CGCM3.1	CanESM2	2	Canadian Center for Climate Modeling and Analysis, Canada
CCSM3	CCSM4	3	National Center for Atmospheric Research, USA
CNRM-CM53	CNRM-CM5.1	4	National Centre for Meteorological Research, France
CSIRO-MK3.5	CSIRO-MK3.6	5	Commonwealth Scientific and Industrial Research Organization/Queensl and Climate Change Centre of Excellence, AUS
GFDL-CM2.1	GFDL-CM3	6	NOAA Geophysical Fluid Dynamics Laboratory, USA
---	GFDL-ESM2G/M	7	NOAA Geophysical Fluid Dynamics Laboratory, USA
GISS-ER	GISS-E2-H/R	8	NASA Goddard Institute for Space Studies, USA
UKMO-HadCM3	UKMO-HadCM3	9	Met Office Hadley Centre, UK

Table 3.1 Continued.

CMIP3 Model	**CMIP5 Model**	**Model # used in Fig.6 d, e**	**Institution**
UKMO-HadGEM1	UKMO-HadGEM2-ES	10	Met Office Hadley Centre, UK
INMCM3	INMCM4	11	Institute for Numerical Mathematics, Russia
IPSL-CM4	IPSL-CM5A-LR	12	Institute Pierre Simon Laplace, France
MIROC3.2	MIROC5	13	Japan Agency for Marine-Earth Science and Technology, Atmosphere and Ocean Research Institute (The University of Tokyo), and National Institute for Environmental Studies

Table 3.1 Continued.

CMIP3 Model	**CMIP5 Model**	**Model # used in Fig. 3.6 d, e**	**Institution**
---	MIROC-ESM	14	Japan Agency for Marine-Earth Science and Technology, Atmosphere and Ocean Research Institute (The University of Tokyo), and National Institute for Environmental Studies
ECHAM5/MPI-OM	MPI-ESM-LR	15	Max Planck Institute for Meteorology, Germany
MRI-CGCM2	MRI-CGCM3	16	Meteorological Research Institute, Japan
BCCR-BCM2	NorESM1-M	17	CMIP3: Bjerknes Centre for Climate Research, Norway CMIP5: Norwegian Climate Center, Norway

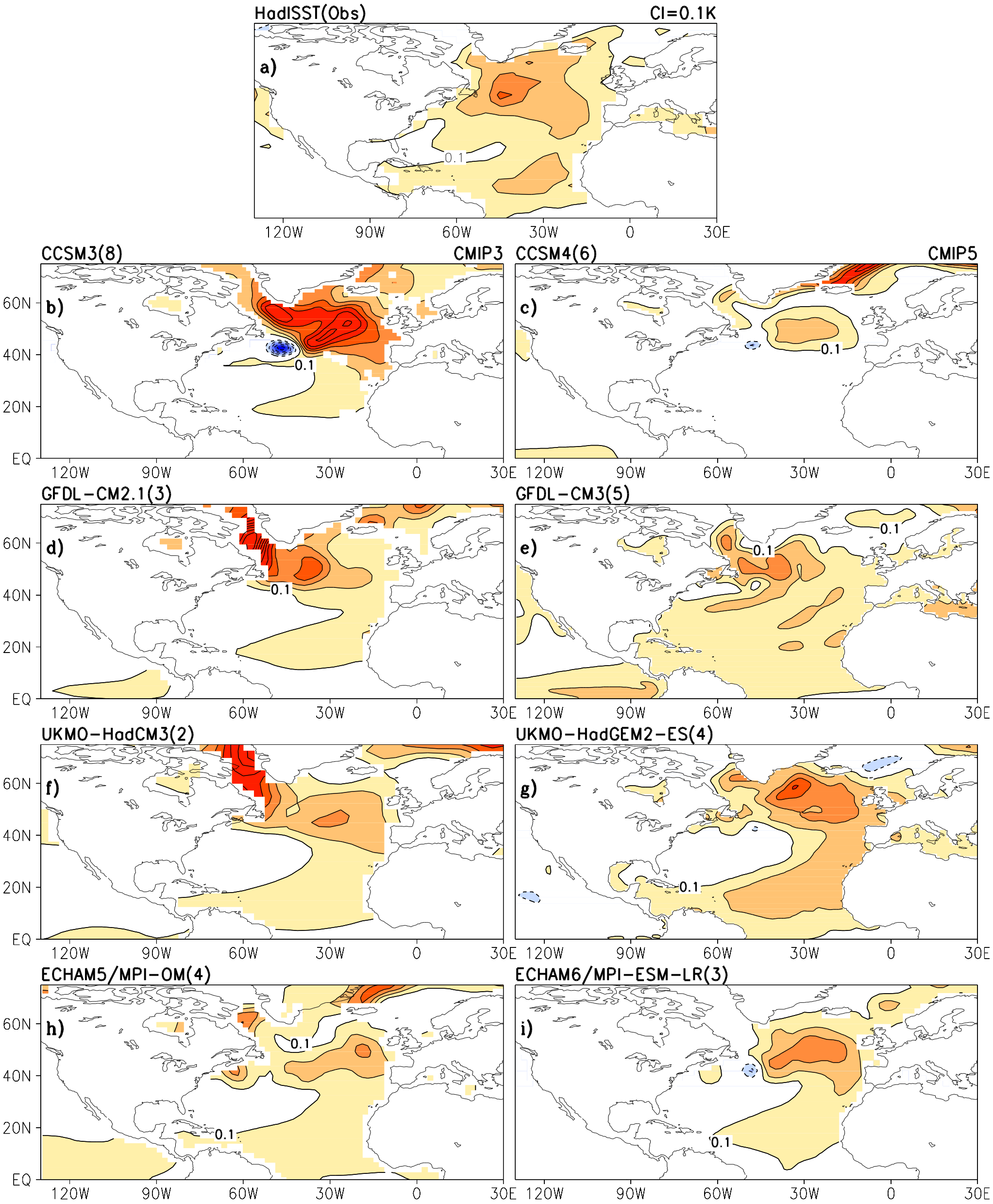

Figure 3.1 All-season regressions of smoothed AMO indices on corresponding SST anomalies in observations (top), CMIP3 (left panels) and CMIP5 (right panels) climate simulations for the period 1900-1999. a) Observed regressed anomalies from HadISST; mean regressed anomalies from CMIP3 simulations from b) CCSM3, d) GFDL-CM2.1, f) UKMO-HadCM3, and h) ECHAM5/MPI-OM models; mean regressed anomalies from CMIP5 simulations from c) CCSM4, e) GFDL-CM3, g) UKMO-HadGEM2-ES, and i) ECHAM6/MPI-ESM-LR models. Regressions from model simulations were calculated for all the ensembles available for a given model, then the mean regression was calculated; the number in parenthesis denotes the number of ensembles used from each model to generate the mean regressed anomalies. Yellow-to-red/blue shading denotes positive/negative SST anomalies plotted with a 0.1K contour interval.

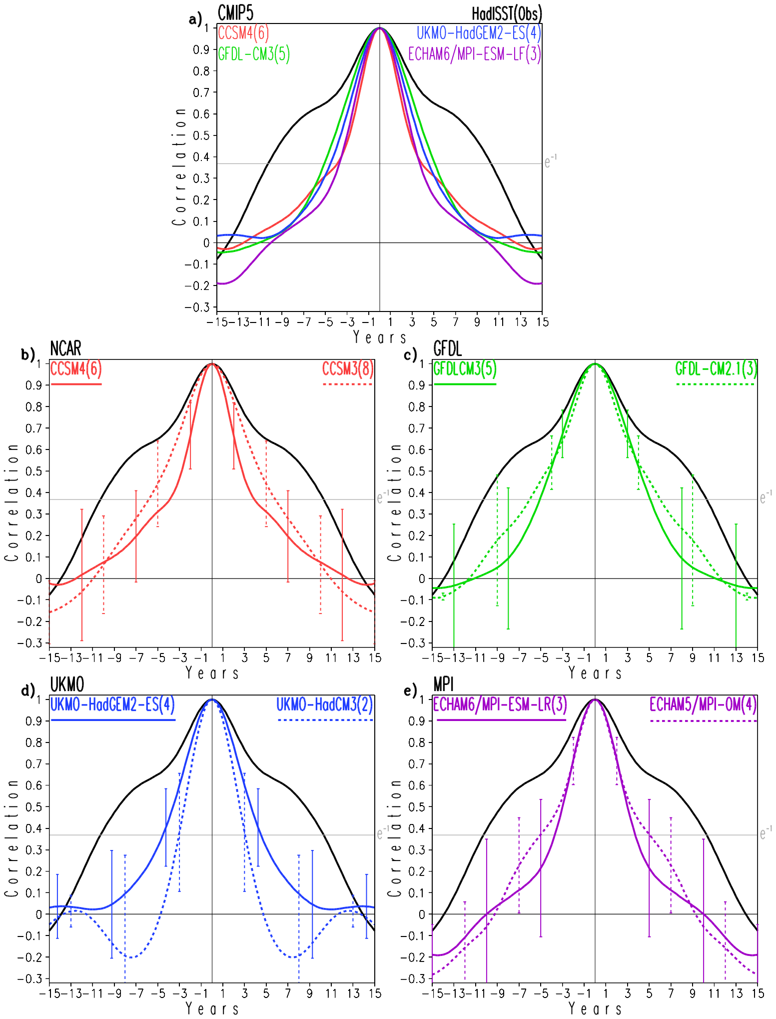

Figure 3.2 Autocorrelations of the smoothed AMO indices from observations and CMIP3 (dashed lines) and CIMP5 (continuous lines) climate simulations for the period 1900-1999. Autocorrelations from observations come from HadISST (black), mean autocorrelations from CMIP5 simulations come from CCSM4 (continuous red), GFDL-CM3 (continuous green), UKMO-HadCM3 (continuous blue), and ECHAM6/MPI-ESM-LR (continuous violet) models, while mean autocorrelations from CMIP3 simulations come from CCSM3 (dashed red), GFDL-CM2.1 (dashed green), UKMO-HadCM3(dashed blue), and ECHAM5/MPI-OM (dashed violet) models. a) Autocorrelations from observations and CMIP5 simulations, mean autocorrelations from b) CCSM4 and CCSM3 simulations, c) GFDL-CM3 and GFDL-CM2.1 simulations, d) UKMO-HadCM3 and UKMO-HadGEM2-ES simulations, and e)ECHAM5/MPI-OM and ECHAM6/MPI-ESM-LR simulations. Autocorrelations from AMO indices from model simulations were calculated for all the ensembles available for a given model, then the mean autocorrelation and the standard deviation among the ensembles were calculated; the number in parenthesis denotes the number of ensembles used from each model to generate the mean autocorrelation, while the error bars represent the standard deviation. The thin gray line represents the 1/e value used to visually estimate the e-folding time of the correlations. The x-axis is given in years.

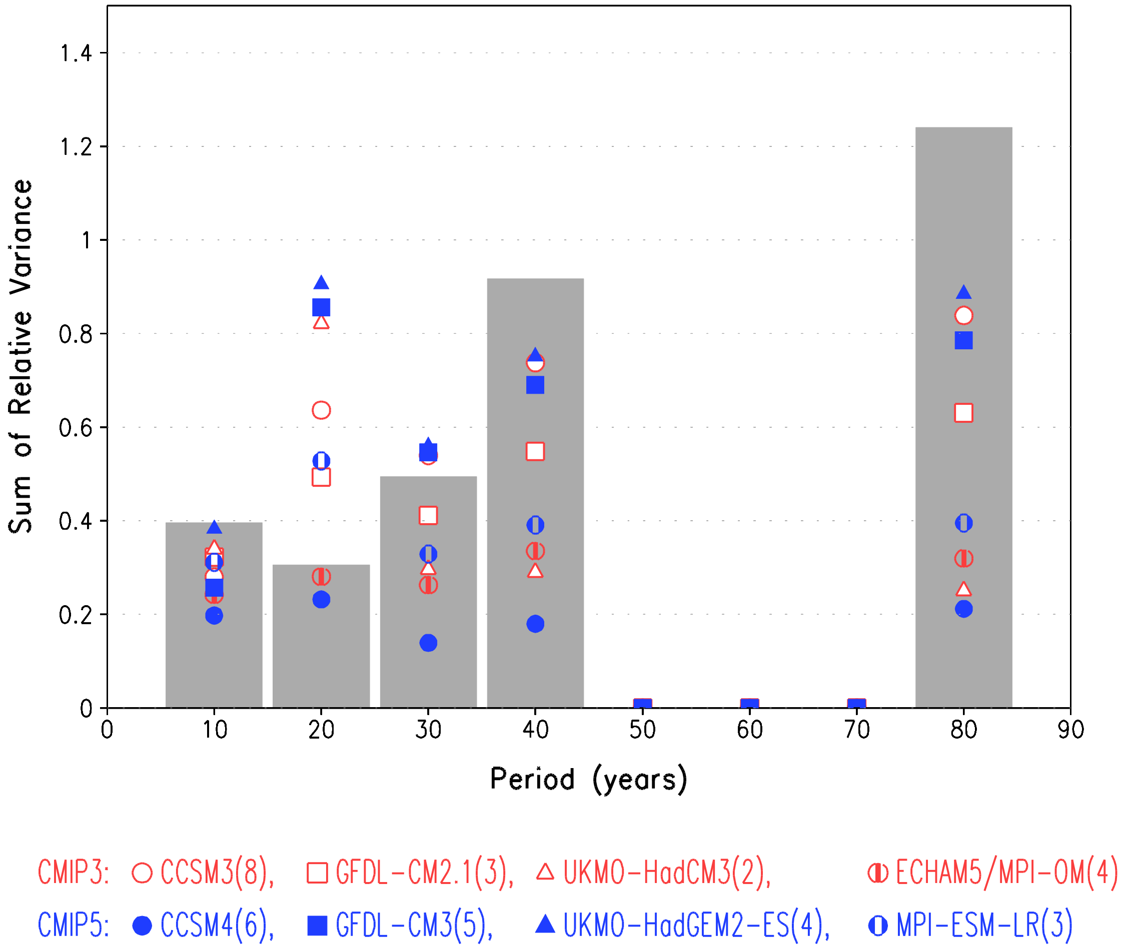

Figure 3.3 Histogram of mean spectral analysis peaks from spectral analyses of smoothed AMO indices for the period 1900-1999. The y-axis denotes the sum of relative variance in the following ranges 2.5-10 years, 11-20 years, 21-30 years, 31-40 years, and 71-80 years. Spectral peaks from the AMO index from observations are shown with the gray bars; the corresponding peaks for the CMIP5 models are shown by the symbols in blue, and those for the CMIP3 models are in red; see legend to identify particular models. The number in parenthesis denotes the number of ensembles used for each model. Spectral analyses were calculated for each ensemble member, and then a mean spectrum was obtained by averaging the spectrum of the ensembles for each model.

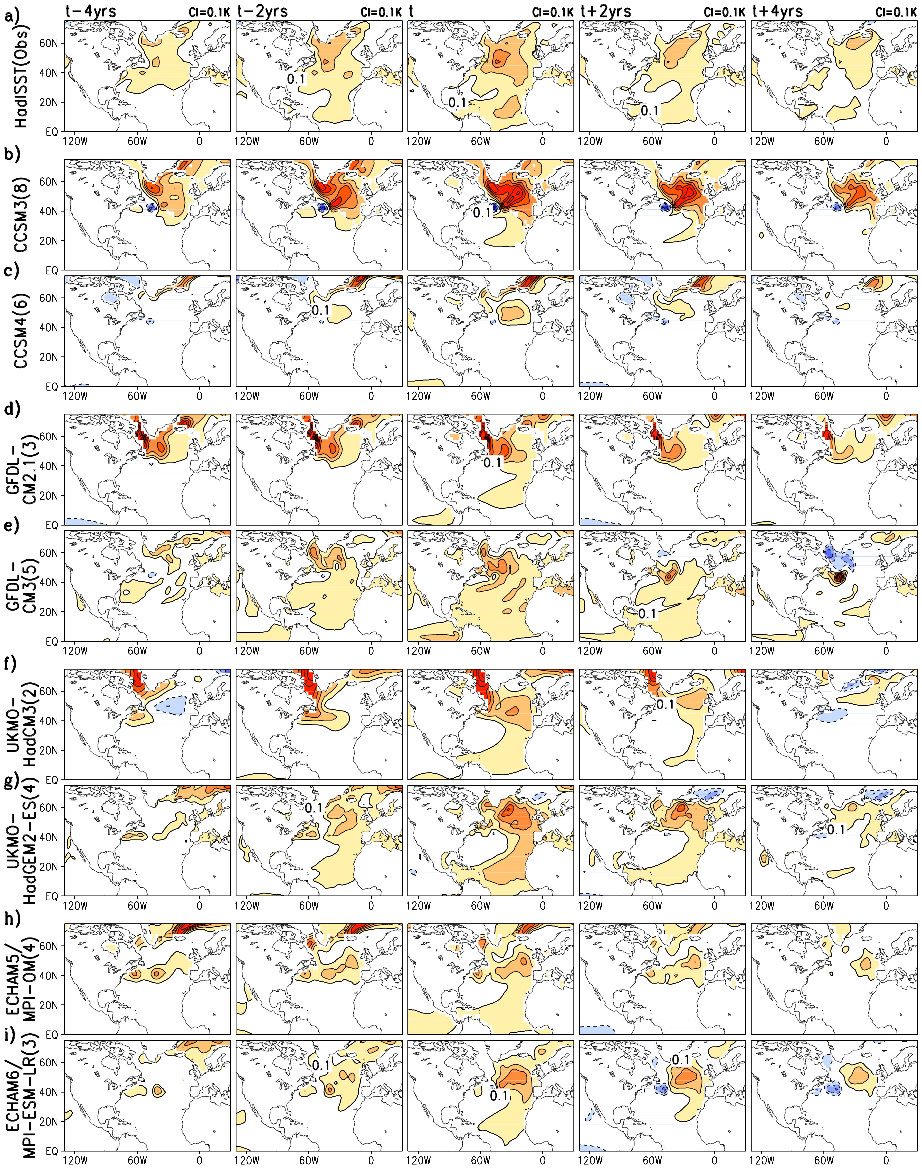

Figure 3.4 Lead/lag regressions of the all-season smoothed AMO indices on SST anomalies from observations and CMIP3 and CMIP5 climate model simulations for the period 1900-1999. The first two columns display regressions 4 and 2 years in advance of the mature phase of the AMO (t-4yrs and t-2yrs respectively), the center column displays the mature phase (t), and the last two columns display regressions 2 and 4 years after the mature phase of the AMO (t_2yrs and t+4yrs). Regressed anomalies from a) HadISST observations, b) CMIP3's CCSM3, c) CMIP5's CCSM4, d) CMIP3's GFDL-CM2.1, e) CMIP5's GFDL-CM3, f) CMIP3's UKMO-HadCM3, g) CMIP5's UKMO-HadGEM2-ES, h) CMIP3's ECHAM5/MPI-OM, and i) CMIP5's MPI-ESM-LR simulations. Regressions from model simulations were calculated for all the ensembles available for a given model, then the mean regression was calculated; the number in parenthesis denotes the number of ensembles used from each model to generate the mean regressed anomalies. Yellow-to-red/blue shading denotes positive/negative SST anomalies plotted with a 0.1K contour interval.

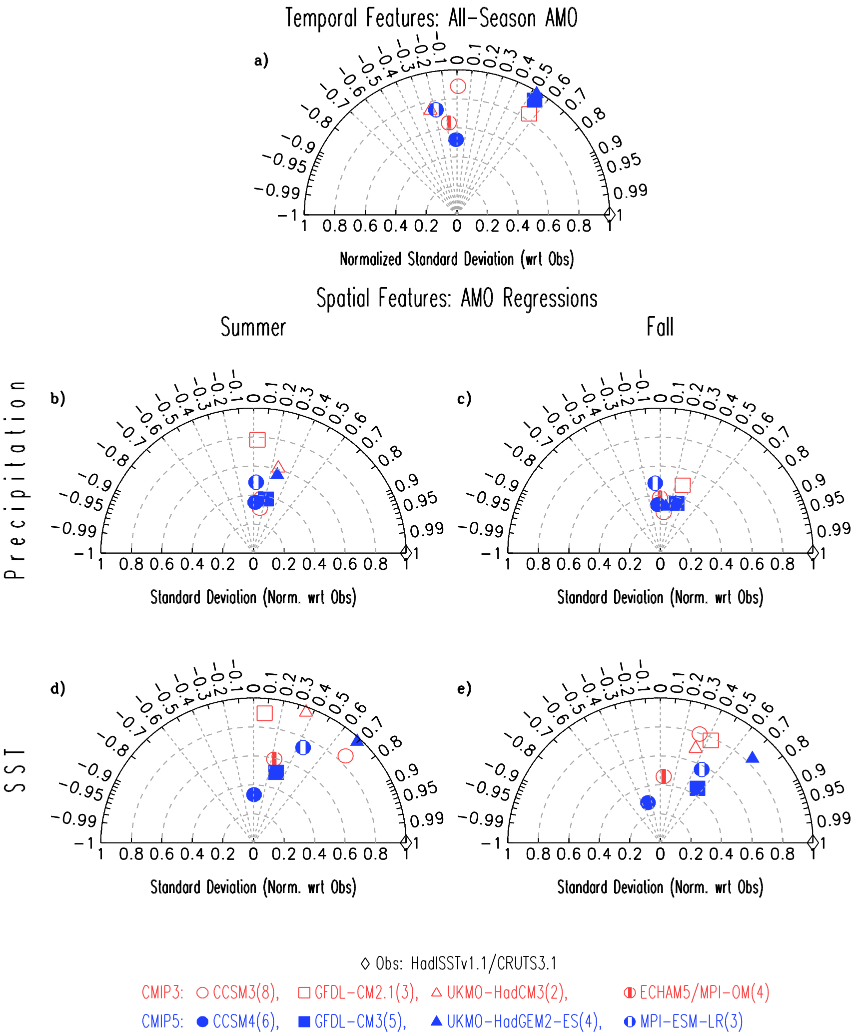

Figure 3.5 Taylor diagrams of smoothed AMO indices and their regressions from observations and CMIP3 and CMIP5 climate model simulations for the period 1901-1999. a) Diagram for temporal features of the all-season smoothed AMO indices; standard deviations have been normalized with respect to the observed standard deviation of 0.17K. b) and c) diagrams for spatial features of regressed continental precipitation anomalies over the (130°-60°W, 0°-60°N) domain in summer and fall respectively; spatial standard deviations have been normalized with respect to the observed standard deviations in summer, 0.16 mm day^{-1}, and fall, 0.18 mm day^{-1}. d) and e) diagrams for spatial features of regressed SST anomalies over the (130°W-10°E, 0°-75°N) domain in summer and fall respectively; spatial standard deviations have been normalized with respect to the observed standard deviations in summer, 0.09K, and fall, 0.10K. Displayed standard deviations and correlations from models are the means of the different ensembles from each model**;** the number in parenthesis denotes the number of ensembles used from each model to generate the mean standard deviation and mean correlation. CMIP3 models are shown in red symbols, and CMIP5 models in blue.

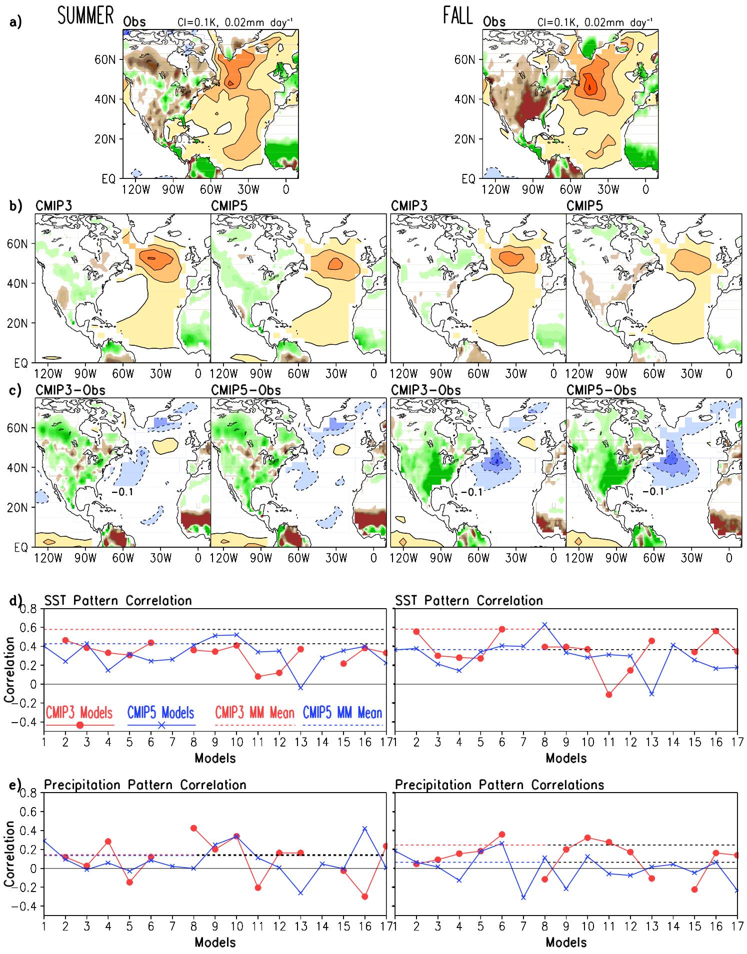

Figure 3.6 Observed and multi-model mean SST and precipitation regressions on smoothed AMO indices and spatial pattern correlations in summer and fall for the period 1901-1999. a) regressions from observations in summer (left) and fall (right), b) mean multi-model regressions from CMIP3 and CMIP5 models in summer (left panels) and fall (right panels), c) difference between multi-model mean regressions and observations in summer (left panels), and fall (right panels). d) diagrams for spatial correlations between regressed SST anomalies over the domain (130°W-10°E, 0°-75°N) from CMIP3 and CMIP5 models with the corresponding from observations in summer (left) and fall (right). e) diagrams for spatial correlations between regressed continental precipitation anomalies over the domain (130°-60°W, 0°-60°N) from CMIP3 and CMIP5 models with the corresponding from observations in summer (left) and fall (right). Yellow-to-red/blue shading denotes positive/negative SST anomalies plotted with a 0.1K contour interval, and brown/green shading denotes positive/negative precipitation anomalies with a 0.02 mm day-^{1} interval in panels a-c). Lines in red/blue denote CMIP3/CMIP5 model correlations in panels d) and e); continuous lines with marks are for the individual models while the dashed lines are correlations for the multi-model means. Spatial correlations for the regressed SST anomalies from the CMIP5/CMIP3 multi-model means are 0.43/0.58 in summer and 0.36/0.58 in fall, and spatial correlations for the regressed precipitation anomalies from the CMIP5/CMIP3 multi-model means are 0.13/0.14 in summer and 0.06/0.25 in fall.

Chapter 4: North Atlantic Upper-Ocean Thermohaline Variability. Decadal-to-Multidecadal Evolution Linked with the AMO.

4.1 Introduction

The previous chapters have shown that the AMO is not a thoroughly understood phenomenon of the climate system. The limited success of the climate models in simulating the spatiotemporal features of the AMO attests to it. The restricted understanding of the AMO starts with the uncertainty in the nature of the AMO, which is a current theme of scientific debate and is further complicated by the spatiotemporal limitations of the data record. The decadal-to-multidecadal time scale associated with the AMO requires access to long data records, which is a particular challenge if one is interested in unraveling the subsurface features of the AMO in the North Atlantic. In this chapter, the spatiotemporal features associated with the AMO are investigated by using a newly released, century-long ocean data set from the UK's Met. Office, and by defining a new way to characterize the decadal-to-multidecadal variability of the Atlantic Ocean; also, the nature of the AMO is explored by analyzing its relationship with the North Atlantic Oscillation (NAO), the main mode of atmospheric variability that has the potential of perturbing the ocean at several levels.

Hydrographic changes in the Subpolar North Atlantic Ocean are of particular importance on interannual to decadal and multidecadal timescales as they provide an insight to the connection that exists between surface and deep ocean circulations. There is considerable evidence that the deep ocean behaves as a damped oscillator on decadal to multidecadal timescales, with the atmosphere providing the energy needed to sustain these oscillations from dissipation (Deser 1996, Danabasoglu 2008, Keenlyside et al. 2008, Latif et al. 2006, Smith et al. 2008).

Atmospheric variability can excite significant fluctuations in the thermohaline circulation (THC), when acting in collaboration with ocean dynamics, in the context of a stochastic, white noise process[9]. An example of this behavior involves the synergy between the enhanced westerly winds and heat fluxes over the subpolar gyre in relation to the positive phase of the North Atlantic Oscillation (NAO) and ocean temperature and salinity anomalies, a combination that helps further intensify deep convection and vertical mixing in the deep-water formation regions. Shifts in the mean atmospheric circulation are also accompanied by changes in the mid-latitude storm tracks' position and the associated synoptic eddy activity, which links these to large-scale variations in the ocean's interior and thermohaline structure. The North Atlantic Subpolar gyre is an oceanic feature of key importance that has the potential to alter the density-driven Atlantic Meridional Overturning Circulation (AMOC) via its influence on freshwater exchanges between the North Atlantic and Arctic basins, and on the advection of salinity and temperature anomalies to and from regions of deep convection and sinking/deep water formation (Yoshimori et al. 2009, Jungclaus et al. 2005).

Propagation of the AMO surface signal into the deeper ocean and its link with changes in the North Atlantic thermohaline (density-driven) circulation remain not fully understood and accounted for, however, due to the lack of consistent spatio-temporal observations, and an incomplete understanding of ocean dynamics and the large-scale, atmosphere-ocean interaction. In an effort to identify long-term trends and decadal to multidecadal climate signals in the North Atlantic and their respective contributions to regional warming (cooling) and fluctuations in oceanic heat uptake, various studies have focused on analyzing the patterns of surface versus subsurface temperature, salinity and potential density across the subpolar and subtropical North

---

[9] "The assumption of white noise is useful for modeling phenomena in which the correlation time of the noise is much shorter than any other time-scales of interest." (Hunter 2009).

Atlantic basins (Polyakov et al. 2010, Colbourne 2004, Mauritzen et al. 2012, Wang et al. 2010). Generally speaking, north Atlantic SST variability has been linked to thermohaline fluctuations (and the enhancement or slowing down of the Meridional Overturning Circulation —MOC) at decadal to multidecadal scales (Polyakov et al. 2010). Some regions such as the Labrador, Irminger and Nordic Seas have been studied due to the occurrence of deep convective ventilation events, which create a bridge between fluctuations in the ocean surface - subsurface structure and the overlying atmosphere (H. M. van Aken et al. 2011, Vage et al. 2011, Femke de Jong et al. 2012). In particular, the AMO signal at the surface can be identified in the subsurface in both salinity and temperature, with the potential density demonstrating compensating contributions from both the salinity and temperature fields (Wang et al. 2010)[3]. Such compensation is notable in parts of the Labrador and Irminger basins examined in the current study; however, this compensation is found to be incomplete, with the temperature and salinity fields contributing unevenly to the potential density field.

Ocean currents and properties are not only influenced by the overlying wind stress but also by the ocean bottom topography (Fig. 4.1). Ocean topography canalizes bottom water from regions of deep-water formation (i.e. the Labrador Sea), while more superficial features, such as the continental shelves, including the Grand Banks also modify surface currents, such as the Gulf Stream, the Labrador Current and the subpolar gyre. However, while the bottom topography is not changing, the atmospheric forcing of the surface ocean features changes, requiring further investigation within the context of the AMO.

While it is known that the NAO can drive changes to the Gulf Stream, the role of the AMO on the latter is little known.Seasonally the Gulf Stream is displaced to the north in fall and to the south during spring (e.g., Tracey and Watts 1986), while it reaches its maximum baroclinic transport in early summer (Sato and Rossby 1995). On the other hand, decadal north to south excursions of the GS position have been linked to large-scale shifts in the atmospheric mass distribution between the subpolar and subtropical North Atlantic (i.e., the NAO —Chaudhri et al. 2011), perturbations in the southward flow of the Labrador surface water (LSW), which in retrospect is associated with large-scale convective variability and the respective strengthening or weakening of the subpolar gyre, as well as fluctuations in the equatorward flow of the Deep Western Boundary Current (DWBC) (Perez-Hernandez and Joyce, 2014). Exploring, thus, the shift between the GS latitude and AMO-related perturbations in the thermohaline structure of the North Atlantic basin is well justified, for the purposes of our study, and provides substantial insight on the lead lag relationship between North Atlantic SSTs, surface-subsurface salinity, changes in ocean heat content and mixed layer depth, as well as high latitude deep water formation and north-to-south movements of the Gulf Stream.

Atlantic multidecadal variability has been traditionally investigated via the analysis of SSTs, however new subsurface ocean data offer us new possibilities. In the current study, we propose an area-averaged AMO index based on deep ocean observations (5-967m vertically-integrated, ocean heat content) in an effort to a) depict a potentially more pristine AMO signal in the subsurface, impartial to atmospheric perturbations; b) characterize AMO variability at deeper levels; c) investigate the variability of thermohaline properties in the northern North Atlantic in two distinct timescales, decadal and multidecadal. We focus on the link between subpolar North Atlantic hydrographic changes and the AMO, while describing the spatiotemporal evolution of related surface temperature, surface salinity, vertically–averaged salinity and vertically-integrated ocean heat content signals, as well as the temporal evolution of the upper 500m profiles of thermohaline properties. Analysis of the thermal and haline anomalies between consecutive winter seasons is also presented in order to identify the vertical propagation and re-emergence of the surface signals of the AMO (Cassou and Deser 2007).

Chapter 4 is divided as follows: Section 2 describes the observational datasets along with the methods and statistical tools that are used to carry out the current analysis. Section 3 discusses the importance of characterizing the AMO by using deep ocean observations and provides a detailed description of the spatial and temporal evolution of AMO-related changes in key hydrographic properties in decadal versus multidecadal timescales. Section 4 examines the vertical thermohaline structure of two 9° areas found in the Labrador and Irminger basins; seasonal profiles are also shown here, in the context of investigating the vertical propagation of surface signals and their re-emergence during consecutive seasons. Section 5 examines important questions pertaining to the role of the NAO and the Gulf Stream in generating subpolar North Atlantic low frequency variability. Section 6 touches upon the general evolution of the subpolar North Atlantic basin's hydrographic properties in the past 60 years.

4.2 Datasets and Methodology

4.2.1 Datasets

In order to characterize Atlantic Multidecadal variability, the current study uses surface and subsurface ocean data as well as surface pressure data from the following Met Office Hadley Centre products.

1. The sea ice and sea surface temperature data set (HAdISST 1.1, Rayner et al. 2005), available on a 1°×1° grid at a monthly resolution for the 1870-present period.

2. The quality controlled subsurface temperature and salinity objective analysis EN4.0.2, a development of the previous versions EN2 and EN3 datasets. This is provided on a grid with 1° spacing in the horizontal, 42 vertical levels at monthly resolution starting in 1900 (Good et al. 2013). EN4.0.2 is comprised of data from all types of ocean profiling instruments that measure subsurface temperature and salinity. The data are subjected to a series of quality control checks and an objective analysis with uncertainty estimates.
3. The mean sea level pressure (MSLP) data set, HadSLP2, available at monthly resolution on a 5°×5° latitude-longitude grid from 1850 to the present.

In order to characterize the variability of the displacements of the Gulf Stream, a Gulf Stream Index (GSI) was sought and provided by Terrence Joyce from the Woods Hole Oceanographic Institution. The index is defined by the use of the 15^{o}C isotherm at 200m-depth in order to characterize the position of Gulf Stream's northern wall and it spanned the period 1954-2012 (Perez-Hernandez and Joyce 2014). Finally, characterization of the atmospheric variability over the North Atlantic was done by means of the North Atlantic Oscillation, which is captured by the widely used Hurrell's NAO index (Hurrell et al. 1995) for the period 1865-2013.

Now, because we were interested in knowing the density changes in ocean water, as density changes can drive the thermohaline circulation, density was calculated from the temperature and salinity fields from the EN4.0.2 data set by using the UNESCO equation of state (Fofonoff and Millard 1983). In this case, we obtained the potential density of seawater, which is the density the sample of ocean water would have if it was raised adiabatically and without change of salinity to the surface, that is, at the conditions of atmospheric pressure.

4.2.2 Methodology

Much of the methodology is based on applied statistical techniques. The mean state of key oceanic and atmospheric fields (i.e. SST, subsurface potential temperature, subsurface salinity, subsurface vertically-averaged heat content, sea level pressure) is obtained at seasonal resolution and calculated from monthly mean quantities. Seasonal anomalies are calculated by removing the seasonal climatology. These anomalies provide the basis for statistical analysis, such as linear regression and correlation. As in the previous chapters, lead-lag regressions and correlations are used to capture the spatiotemporal features of the AMO.

The AMO indices are constructed by spatially averaging the sea surface temperature anomalies (for the traditional SST-based definition of the AMO) and vertically-integrated heat content anomalies (for the proposed subsurface-based AMO index) over the North Atlantic basin (5°-75°W, 0°-60°N); then, the area-averaged indices are: a) linearly de-trended over the January 1950- November 2013 period, using the least-squares method; b) smoothed by applying a local regression filter to remove high-frequency variations without aliasing the decadal-to-multidecadal scale pulses; and c) normalized to unit variance, by dividing each detrended and smoothed index by the respective standard deviation of the calculated index.

Smoothing of the indices is done differently now by using a different technique, the local regression method (aka, LOESS[4]) (Cohen, 1999), to avoid losing information at the ends of the time series as it was the case by using the binomial filter in the previous two chapters. Local regression smoothing is a non-parametric method to fit smooth curves to empirical data, by depicting the “local” relationship between a response variable and a predictor variable over parts of their ranges. It is non-parametric so it does not require knowledge of the specific functional relationship that may exist within the data. Instead, the fitting algorithm follows the empirical concentration of the plotted points. At each point in the data set, a low-degree polynomial is fitted to a subset of data (e.g., 5% in the indices discussed later) using weighted least squares, giving more weight to points near the point whose response is being estimated. The LOESS fit is complete after regression function values have been computed for each of the data points.

4.3 Surface and subsurface fingerprints and timescale of the AMO

Historical and modern hydrographic data show substantial, multidecadal variability in the surface and subsurface temperature, salinity and vertically integrated heat content of the North Atlantic basin. Superimposed on this long-term variability, stand decadal pulses of measurable amplitude, observed in regions of intermediate and deep-water formation (Irminger and Nordic Seas, Icelandic basin, Labrador Sea etc.), as well as in the entire North Atlantic basin. The physical mechanisms associated with this variability remain an issue of debate, due to the lack of consensus regarding the governing feedback processes that drive phenomena like the AMO and its perturbations in the North Atlantic THC. Among them, one can distinguish the temperature and salinity advection mechanisms between the subtropical and the subpolar North Atlantic (Stommel 1961), as well as feedback processes that operate through the atmosphere, such as local air-sea coupling and atmospheric heat transport (Power et al. 1995), changes in atmospheric water vapor (Nakamura et al. 1994) and in wind forcing (Fanning and Weaver 1997a), in response to SST variations. Understanding, thus, the vertical extent and low-frequency propagation of surface signals and their connectivity to the subsurface thermohaline circulation can provide substantial insight with respect to the origins of interdecadal perturbations in the North Atlantic and the respective role of ocean versus atmospheric dynamics in sustaining such patterns of large-scale variability.

Characterization and understanding of the subsurface features associated with the AMO is one of the main goals of this research. Thus, it is apparent that the use of an AMO index based on SSTs will be subject to atmospheric forcing and will have limited information from the subsurface. Therefore in this section an AMO index based on the subsurface thermal structure is defined aiming to 1) have a more pristine AMO signal in the subsurface, 2) capture lower frequencies, and 3) characterize variability at deeper levels with an index. Heat content-based AMO (AMO-HC) indices were calculated for several layers and compared among them and against the traditional SST-based, AMO index (Fig. 4.2). It is found that the subsurface AMO-HC indices lead the surface AMO-SST index and that a good choice for an AMO-HC index is the one using the layer 5-967m (red line), as this is similar to some other shallower indices, and indices using heat content at deeper layers have the shadow of uncertainty due to sparse data. Of particular interest is the very recent period where the subsurface signal suggests that we are past the peak of the AMO phase identified by the traditional AMO index (black line).

Figure 4.3[5] shows the time series of five normalized[6] AMO indices, which differ from each other in the spatially averaged field, the smoothing filter and the method used to construct each one of them, for the common, January 1950 –November 2013 time period. The AMO-SST index (raw data) as well as its respective smoothed (LOESS 5% and 25%) versions are shown, along with the AMO-HC index that is defined using spatially averaged, vertically integrated (5-967m) heat content data, smoothed by LOESS 25%, and finally, the AMO principal component, product of an EEOF analysis (Guan and Nigam, 2008), also smoothed by LOESS 25%. It is noteworthy that the AMO-SST index is shown to lag the AMO-HC index, with maximum correlation of 0.69 (0.49), observed at a 4 year lag between the two (LOESS 25% (5%)) time series (Fig. 4.4). Furthermore, the AMO-HC index is suggestive of a cooling North Atlantic subsurface in the recent years (mid-2000s –present), a feature that is almost absent (minimal) in the ocean surface and could have tremendous implications in a) predicting future North Atlantic climate, b) attributing its variability to human versus natural fluctuations and forcings and c) anticipating its co-variability with global climate, especially in the context of a recent slowdown in the rise of global average temperatures (hiatus) which was noted in the last assessment report of the IPCC.

Autocorrelations of these indices are shown in Figure 4.5, in order to estimate the AMO time period. If the zero autocorrelation is used as a guide to estimate the timescale of the AMO, it is found that this lasts for approximately 50 years when the smoothed (LOESS 25%) AMO-SST and AMO-PC indices are used to characterize the AMO. The decorrelation timescale decreases significantly to about 25 years, when using the subsurface index to describe the phenomenon. An immediate question that arises is what causes the estimated periods to be so different. If the ocean were passively responding to atmospheric variability, its heat capacity would turn the atmospheric high frequency into much lower frequencies in SSTs (e.g., Hasselmann 1974). While the traditional AMO seems to be responding to this type of interaction, this is not the case for the AMO-HC index whose time scale is smaller and seems to be responding to a different atmosphere-ocean interaction in which the ocean circulation plays a more active role in the interaction (e.g., Bjerknes 1964, Bryan and Stouffer 1991).

Several mechanisms have been proposed throughout the years as principal drivers of such diverse periods of North Atlantic low-frequency variability, observed in model simulations and observations of the North Atlantic climate system; these include a) the ocean's response to atmospheric large-scale perturbations (Delworth and Greatbatch, 2000), b) coupled ocean-atmosphere changes that might be influenced by variability in other basins (i.e. the Pacific basin) (Dima and Lohmann, 2007), c) delayed advection of the Atlantic Multidecadal Overturning Circulation (Lee and Wang, 2010), d) interconnectivity between the tropical and the northern North Atlantic (Knight et al., 2005) and finally e) the interaction between the Arctic and the supbolar North Atlantic basins (Frankcombe and Dijkstra, 2011).

Frankcombe and Dijkstra (2011) investigated the role of an internal ocean mode, the so-called *thermal Rossby mode,* in the existence of multidecadal fluctuations and shorter timescales in the North Atlantic variability. The pattern and period of this *thermal Rossby mode* are consonant with westward propagating, subsurface temperature anomalies in the North Atlantic and sea level changes on the European and North American coasts (Frankcombe and Dijkstra, 2011), which occur every 20–30 years. It was thus suggested that such westward-propagating, temperature anomalies, which are moving across the background, basin temperature gradient, along with internal ocean variability integrate stochastic, atmospheric weather patterns to increase the variance and dominant period of dynamic ocean properties, producing in this way a red spectrum in thermocline depth or sea surface height variability (Frankignoul et al. 1997, Kwon et al. 2009). This mechanism might well be responsible for the 25-year AMO time period, which is inferred when using the vertically integrated, subsurface index, in the current study.

To discern the antecedent and latter phases of the AMO and their imprint on surface temperature and salinity, as well as vertically averaged (5-315m) salinity and vertically integrated

(5-315m, 372-967m) heat content, we compute the lead lag regression coefficients using the AMO heat content (AMO-HC; 5-967m) index smoothed with the LOESS 5% filter (Fig. 4.6) and LOESS 25% filter (Fig. 4.7); regressions are shown for a period of T-8 to T+8 (T-16 to T+16) years, in 2-year (4-year) time steps. Evident in the first panel of lead-lag regressions (Fig. 4.6) is the lag relationship between *AMO-SST* and *AMO-HC* indices. Maximum AMO-regressed SST anomalies peak at T+4 years (instead of T=0 years in the case of regressions with the *AMO-SST index*). In the course of the 16-year regression period (which entails a full AMO cycle, based on the discerned time period from the figure of autocorrelations (Fig. 4.5), we observe strong negative anomalies centered in the northern latitudes and around the regions of interest (Labrador and Irminger seas), which are subsequently replaced by warm anomalies in the mature and post-mature phases. Furthermore, a build-up of the link between the subpolar and the subtropical basins is noted at the T=0 phase and the follow-up years.

When focusing on the second and third panels, the salinity signal appears stronger at the surface. Negative (fresh) anomalies, centered over the water around the southern tip of Greenland and over the Gulf Stream region, off of the coast of southeastern US, are gradually dissipating and being replaced by positive (saline) anomalies. At T-8 years, the deep western boundary (DWB) and West Greenland currents appear strengthened, whereas the Gulf Stream has declined and is pushed southward. In the follow-up phases, local saline anomalies develop over the Labrador Sea (T-6 years), without an evident connection with the lower latitudes and the Gulf Stream's northern extension until 2 years before the mature phase of the AMO. At T-2 years and onward, the salinification of the Labrador basin, which seems to be at least partially originating in the Gulf Stream region, is followed by an eastward expansion of the signal toward the Irminger basin, the Denmark Strait and the Nordic seas.

Finally, the heat content anomalies reflect a subsurface footprint of the surface signal, with the upper 315m showing cooling in the northern latitudes during the T-8 and T-6 years, followed by a warming of the central and northern North Atlantic and a subsequent cooling of the Gulf Stream region and the area off of Newfoundland. The penetration depth of the surface warming (cooling) reaches the 372-967m layer in many cases, with the deeper layer displaying a delayed warming by approximately 6 years (compared to the upper ocean layer), over the subpolar North Atlantic regions of interest. Several factors control and influence changes in such vertically integrated properties in the northern latitudes, including the interaction between convectively formed waters (i.e. the Labrador Sea Water (LSW)) and other intermediate waters of the North Atlantic, via mixing and entrainment disseminating vertically.

Regressions of the LOESS 25% smoothed index on the same 5 fields for a T-16 years to T+16 years time range (Fig. 4.7) reveal an entire AMO cycle, imprinted on the surface and subsurface hydrographic features of the North Atlantic. The salinity signal remains primarily focused on the surface, while AMO related, heat content anomalies penetrate throughout the upper and deeper layers in a not-always coherent manner. In the course of a full AMO-cycle, the Labrador and Irminger seas are dominated by fresh and cold anomalies that are subsequently replaced by warm and saline anomalies, after approximately 8 years.

4.4 Decadal-to-multidecadal variability in the Subpolar North Atlantic

The North Atlantic Ocean is a key region for the thermohaline circulation, which drives the so-called global conveyor belt. Water is cooled by arctic air masses in the subpolar North Atlantic, which also gets saltier because the salt is left behind in the surrounding water after ice forms. In this way, the cold water gets denser due to the added salts, and sinks toward the ocean bottom. Surface water moves in to replace the sinking water, and the process is repeated, to create the deep ocean currents that drive the conveyor belt. Two regions of great importance within the suboplar North Atlantic are the Labrador and Irminger Seas. The Labrador Sea, situated between the Labrador Peninsula and southern Greenland, and the Irminger Sea, situated between southern Greenland and the Reykjanes Ridge (an underwater mountain range that extends from Iceland – see Fig. 4.4 for reference) are critically important areas of the North Atlantic. While the Labrador Sea hosts a region of deep-water formation (as explained above), the Irminger Sea is a region where ocean currents meet, forming new kinds of dense water. Thus, due to the importance of these regions, changes in their water properties linked to the AMO are analyzed next.

4.4.1 AMO-related evolution of hydrographic properties in the Labrador Sea

The Labrador Sea is a region of particular importance in characterizing the subpolar North Atlantic climate and in investigating the interconnectivity between the Arctic and North Atlantic Basins, as well as in refining our understanding of deep water mass production, large-scale, North Atlantic air-sea interactions and the influence of northern North Atlantic latitudes in the Meridional Overturning Circulation (MOC), which in its turn, regulates the great ocean conveyor belt (Haupt and Seidov 2007). Among the principal water inflows that affect the Labrador basin are the Labrador and West Greenland currents, two distinct baroclinic boundary currents originating in the Canadian Arctic Archipelago and the East Greenland shelf, the Irminger current stemming from the Irminger sea, as well as an inflow of Subpolar Mode Water emerging from a branch of the North Atlantic Current (warm and salty water). Finally, the Nordic Seas deep and bottom water masses also intrude into the Labrador basin, crossing the Greenland-Scotland Ridge and mixing with the Labrador Sea intermediate Waters (LSW) (Yashayaev, 2007). Additional factors influencing long-term, LSW changes include perturbations in the winter North Atlantic atmospheric circulation (i.e. NAO) and the associated intensity of westerly winds and wintertime convection, as well as in other, non-local processes such as Arctic sea ice melting, Arctic inflow and continental runoff (Peterson et al. 2006).

Labrador Sea intermediate Waters properties -temperature, salinity, and thickness- exhibit significant variability through time. Igor Yashayaev (2007) describes some of the key hydrographic variations that have been observed in the Labrador basin during the period of 1960-2005. Distinct warm and salty conditions prevailed between the mid-1960s and early 1970s; these were subsequently replaced by fresher and colder conditions between the late 1960s and early 1970s, as well as the late 1980s and mid-1990s, which were reversed again to a phase of positive thermal and haline anomalies, from the mid-1990s and onward. It is important to note here the distinct, low salinity and low surface density conditions that prevailed during the 1967-72 and the early 1980s periods, known as the Great Salinity Anomalies (GSA), which inhibited convection in the Labrador Sea.

In our study, we concentrate in a similar time period to the one examined by Yashayaev (2007) –extended by approximately 20 years (1950-2013), to characterize the thermohaline oceanographic conditions in the Labrador Sea, in relation to low-frequency North Atlantic surface variability (AMO). To carry out our observationally based analysis, we choose a 4° longitude x 4° latitude area in the Labrador basin (51° -55°W, 56°-60°N) (Fig. 4.6). The results have been compared to the ones derived, when choosing one single grid point (i.e. 53°W, 58°N)-not shown here, to assure that they are not an area-averaging artifact, but represent the temporal evolution and propagation of the AMO-related signal through the top 500m ocean layer. The AMO-SST index (classical definition, see §4.2.2) is used in this part of the analysis, as our goal is to capture the vertical extent and propagation of AMO-related surface signals through time; a vertically-integrated property (i.e. AMO-HC index) would tend to lessen the magnitude of signal differences between surface and subsurface and is therefore discarded for this part of the analysis. Lead-lag regressions (correlations) of the AMO SST-index on the 0-500m potential temperature, salinity, and potential density fields are shown for a T-10 years to T+10 years period and are shaded blue-to-red (drawn using white contour lines) when the index is smoothed with the LOEES 5% filter (Fig. 4.8), and the LOESS 25% filter (Fig. 4.9). Before carrying out the regressions, the AMO index is smoothed for the January 1950 –November 2013 period, using the LOESS 5% (25%) local regression filter, to underline the AMO-linked decadal (multidecadal) evolution of the Labrador Sea thermohaline features, and normalized by its standard deviation. The individual contributions of potential temperature and salinity to LSW's net potential density are being examined separately, to emphasize the relative importance of each field in shaping density changes in the region, in an effort to deduce possible mechanisms driving these surface-subsurface footprints.

The potential temperature, salinity and potential density based only on temperature/salinity profiles indicate a downward propagation of positive, surface anomalies through time, with the penetration depth increasing as we move forward in time. Surface salinity maxima seem to precede surface temperature and are constrained to the top ~100m; fluctuations in the net density field are dominated by salinity changes. Finally, two distinct surface signals with duration of about 8 years and a subsurface signature extending to the top 500 m of the ocean are discernible in the net density profile, characteristic of the decadal pulses embedded in the multidecadal North Atlantic surface variability. These features are less noticeable when carrying out the same lead-lag regression analysis with the more highly smoothed (LOESS 25%) AMO-SST index. In this case (Fig. 4.9), we arrive at similar patterns of downward propagation of temperature, salinity and density anomalies through time, with a more temporally coherent signal at different depths. In the interest of examining the statistical significance of these results, we use a *two-tail student t-test* at the 5% (0.05) level and found that correlations above the |±0.27| value are considered statistically significant at all lags.

Next, we focus on the seasonal variability over the Labrador sector, by extracting the smoothed AMO-SST index corresponding to each season and using the seasonal versions to regress on potential temperature, salinity and potential density fields. Figure 4.10 shows the case for a winter index extracted from the LOESS 5% smoothed AMO-SST index: persistent year-to-year thermal anomalies extend to 100-150m below the surface and reach deeper and deeper levels with time (~ 450-500m at T+10 years). Winter anomalies persist within the stratified thermocline through spring and summer, due to reduced surface winds and a shallow mixed layer, and reemerge in the following fall/early winter with the deepening of the ocean mixed layer due to the late fall/early winter, extratropical atmospheric forcing (Cassou and Deser, 2007). The detection of such seasonally recurring anomalies that are linked to low-frequency variability is a non-trivial task as a. advection of such mixed-layer anomalies by mean ocean currents can lead to their zonal or meridional propagation and reemergence at different regions and b. the amplitude of the reemergence mechanism depends on a variety of factors including mixed layer depth, the strength of summer surface anomalies and the magnitude of vertical mixing (Frankignoul 1997).

The winter pattern in Fig. 4.10 contains year-to-year temperature and salinity signals that extend to ~500m depth at lags of ~ T+10 years. Observed near-surface temperature and salinity anomalies tend to persist with a relatively uniform magnitude for approximately 4 consecutive winter seasons. Potential density anomalies also demonstrate year-to-year variability in the vertical, in a less homogeneous way, due to the partial compensation of the temperature and salinity influence on density. Despite the relatively shallow mixed layer, the wintertime persistence is high, due in part to the redness of the SST anomaly timeseries that is linked to the AMO. Finally, we note that the amplitude of the reemergence of the wintertime anomalies in the follow-up seasons is more evident when focusing on the top 250m layer. Fig 4.11 shows a close-up of the regressed SST and salinity anomalies in this layer during a period of T-3 to T+3 years that indicate the existence of a re-entrainment mechanism linked to the seasonal cycle of the mixed layer depth that helps maintain the SST and salinity anomalies and with them the decadal signal.

4.4.2 AMO-related evolution of hydrographic properties in the Irminger Sea

The Irminger basin is another highly influential region of the subpolar North Atlantic, due to its key position in the intersection of Arctic freshwater outflow and the dense overflows from the Nordic seas, which contribute to the formation and propagation of the Deep Western Boundary Current (Vage et al. 2011). Water from the Irminger Sea can also be of importance for the Labrador Sea as relatively less cold and saltier waters from the Irminger Sea can be identified in the Labrador Sea (Pickart et al. 2003). Figures 4.12 and 4.13 show the lead-lag time-versus-depth profiles in the Irminger Sea of the same regressed anomaly fileds that we examined over the Labrador basin, in the previous section; Fig. 4.12 shows anomalies when the AMO index is smoothed with the LOESS 5%, and Fig. 4.13 when it is smoothed with the LOESS 25%. Overall, the Irminger basin displays a similar temperature and salinity vertical structure to the one over the Labrador Sea (positive/negative salinity anomalies coincide with warm/cold temperature anomalies), with positive surface anomalies being noted at about T-2 years, propagating downward to about 450-500m, while the AMO-SST time series is leading potential temperature and salinity by 0-12 years[7]. The increases in temperature and salinity do not compensate completely, leading to negative (lighter) potential density anomalies. Temperature appears to be more influential than salinity in determining the sign and magnitude of the aforementioned density changes, in contrast to what happens in the Labrador Sea where the density anomalies are driven by the salinity anomalies.

To efficiently interpret such downward propagating signals, a thorough knowledge and understanding of the ocean currents that dominate the region's circulation, as well as of the oceanic and atmospheric processes that are present in the Northeastern North Atlantic is necessary. Furthermore, topography not only below the ocean's surface (as shown in Fig. 4.1) but also high topography over land becomes very important. The high topography of Greenland, for instance, forces the westerly winds to go around the continent, causing them to accelerate. In addition, river runoff and melting of the Greenland ice sheet can lead to supplemental freshening of the Northeastern, North Atlantic region.

The effect of local convective mixing on the thermohaline structure in the Irminger Sea remains unclear, despite various studies on the gyre circulation and convection over the Irminger basin (Vage et al. 2011, McCartney and Talley, 1984, Pickart et al. 2003). Deep convection, which occurs during winter due to large heat loss from the ocean surface to the atmosphere, leads to mixing down to about ~400m (~1000m during the 2007-2008 cold winter event ―Vage et al. 2009). This can potentially influence the stability of the Labrador Sea water, via advection by the East Greenland and Irminger currents. Additional small-scale processes, such as lateral and vertical turbulent mixing (salt fingering) of adjacent water masses (Ruddick and Kerr, 2003) caused by differences in the molecular diffusion of heat and salt (double diffusion), as well as mechanical forcing such as wind stirring processes can lead to changes in the hydrographic properties of neighboring water masses and surface signal intrusions into the subsurface, with a vertical extension of a few hundred meters.

Smaller scale, seasonal variability is discerned via regressions of the seasonal AMO-SST time series on the temperature, salinity and density fields; regressions using the winter smoothed (LOESS 5%) AMO index are shown in Fig. 4.14. The horizontal scale (lead-lag time) shows us that it takes about two to three years (i.e. winters) for vertical intrusions of a few hundred meters to occur. As noted earlier, density anomalies are driven by temperature anomalies so the year-to-year variability of the water properties could be the result of mesoscale eddy shedding by the boundary currents and shifts in the seasonal eddy kinetic energy, which have a substantial signature in both Irminger and Labrador Seas (Volkov 2005, Flatau et al. 2003). Re-entrained winter anomalies can contribute to the winter to-winter persistence of the same SSTA pattern, which may subsequently project upon the overlying atmospheric circulation via transient eddies (Rodwell and Folland, 2002). This can influence the weather patterns over the subpolar North Atlantic, leading to milder or stronger winters, via modulation of the North Atlantic Oscillation (NAO), an atmospheric mode of variability reflecting a surface pressure correlation pattern within the North Atlantic.

4.5 NAO and the Gulf Stream influence

The NAO-AMO relationship is a subject that requires supplemental research and understanding, due to the possibility of the atmospheric forcing of the AMO. While a non-stationary relationship between the NAO and the AMO has been identified before (Walter and Graf, 2002), a 10-15 years leading window of the AMO over the NAO in winter has also been proposed in the more recent years (Peings and Magnusdottir, 2014). On the other hand, while the Gulf Stream appears to be responding to the NAO variability (Taylor and Stephens, 2002), it is also capable of altering the NAO (Wu and Rodwell, 2004). However, it was clear from the lead/lag regressions in SSTs, salinity and heat content shown in the previous sections that the Gulf Stream is experiencing important changes, while under the AMO influence. Thus, this section will focus on the interplay among these climatic features.

In the early twentieth century, Walker analyzed the spatial correlation of seasonal weather patterns and noticed a surface pressure correlation signature within the northern North Atlantic that he referred to as the "North Atlantic Oscillation" (NAO) (Walker and Bliss 1932). About 30 years later, Bjerknes also discussed air-sea interactions in the northern North Atlantic (Bjerknes 1964), to address the driving mechanisms of year-to-year and longer-term variations in the surface temperature of the Atlantic Ocean. In the more recent years, the NAO has been accepted as a leading atmospheric mode of key significance for local as well as global climate variability (Hurrell et al. 2001, Marshall et al. 2001). Hurrell et al. (2001) showed that the NAO forcing is stronger during the late fall and winter / early spring months (November through April), when the ocean mixed layers are deep and ocean-atmosphere heat fluxes are the greatest. In the current study we use a widely used NAO index (Hurrell et al. 1995) to investigate the lead-lag relationship between the AMO-SST and AMO-HC time series, as well as the relationship between the NAO and the Gulf Stream (which is closely connected to low-frequency, subpolar North Atlantic variability via its northern extension). The Gulf Stream index (GSI) used provides an estimate of the latitudinal shifts of the Gulf Stream, measured by using the 15°C isotherm at 200m depth (Perez-Hernandez and Joyce 2014). The following analysis is focused on the period 1954-2012 due to availability of the GSI.

Lead/lag relationships between the NAO and GS indices (Fig. 4.15 and the GS and AMO indices (Fig. 4.16) are analyzed now. We find the simultaneous correlation between the GS and NAO indices to be 0.58 when smoothed heavily (LOESS 25%) and 0.40 when the smoothing is less severe (LOESS 5%) The two time-series are best correlated at one-year lag, with the NAO leading the Gulf Stream Index (maximum correlation of 0.59).[8] On the other hand, the lead-lag correlations between the GSI index and the two AMO indices (Fig. 4.16 indicate that the GSI index leads both AMO-HC and AMO-SST indices. Maximum correlation between GSI and AMO-SST indices is -0.64 when the indices are heavily smoothed (LOESS 25%), and -0.52 when the smoothing is less severe (LOESS 5%) at 35 seasons. Maximum correlation between the GSI and AMO-HC indices is 0.49 when the indices are heavily smoothed (LOESS 25%) at 10 seasons lag, and 0.43 when the smoothing is less severe (LOESS 5%) at 13 season lag.

The simultaneous regression maps of the influence of the North Atlantic Oscillation and Gulf Stream indices on mean sea level pressure for the common period January 1954- November 2012 are also examined (Fig. 4.17[9]) in order to discern the full structure of sea level pressure anomalies and the dominant circulation conditions in response to the NAO and Gulf Stream variability. As expected by the suggestion that the NAO drives the GS latitudinal interannual variability, both regressed pressure anomaly patterns exhibit a meridional dipole consisting of a zonally elongated band of negative anomalies constrained in the northern latitudes (north of 55°N, with a center north of Iceland) and a band of positive anomalies in the subtropics with a center around 35°N. The spatially coincident (to a certain extent) regression patterns in MSLP can be attributed to the coordination between the Gulf Stream's excursions in mean position and the wind stress associated with NAO (Joyce et al. 2000; Frankignoul et al., 2001). During a high NAO index phase, the Gulf Stream flow path is displaced to the north of its climatological position while it is displaced southward in the low index phase. We expect anomalous southerly geostrophic winds across the Greenland and Barents Seas, consistent with enhanced ice melting and thus reduced ice extent and enhanced freshening, as well as northwesterly winds over the Labrador Sea, consistent with colder conditions and increased sea ice.

Hydrographic features of the GS index are reminiscent of the NAO. Lead-lag regressions of the GS index on SSTs (top panel, Fig.4.18) show an incipient tripole SST pattern at T-2 lags that reaches maximum anomalies at T=0 lag, with negative anomalies situated south of Greenland and off of the western African coast in the tropics and a band of positive anomalies between them over the Gulf Stream region. This pattern is also discernible in the subsurface (heat content panels, Fig. 4.18). As time evolves, the northern latitudes become warmer (T+4 phase and onward), while the anomalies over the Gulf Stream region weaken. At lags T-8 to T-2, we note a southward propagation of fresh (negative salinity) anomalies originating from the northwestern, subpolar North Atlantic and Labrador Sea, which is accompanied by a retreat of the saltier Gulf Stream water further to the south. This southward influx of freshwater is halted and then replaced by a northward propagation of saltier water, at lag 0 and forward in time. The intrusion of saline waters at T+8 years lag is first directed toward the Labrador basin, with a subsequent propagation toward the Irminger Sea, southeast of Greenland. During this time, more saline and warmer waters characterize the entire northern North Atlantic latitudes.

4.6 Multidecadal signal in the Subpolar North Atlantic

Decadal-to-multidecadal variability in the subpolar North Atlantic is very similar to that from the AMO. To conclude this chapter, area-averaged subpolar North Atlantic (75°W-5°E, 45°-75°N) vertically-averaged (~sfc-700m) hydrographic properties are analysed (Fig. 4.19); the chosen depth (700m) is used not only for reference purposes (e.g., Wang et al. 2010), but because there is more confidence on the quality of the subsurface data at these levels than in data from deeper levels. It is apparent that a cooler and fresher subpolar North Atlantic emerges, in accordance with AMO's cold phase during the 1970-1990 period (Fig. 4.19, top panel); the opposite is observed during the warm phases of the AMO, before 1970 and 1995 and onward. The net density is shown to be tracking salinity (temperature) in the post (pre)-1980s period (Fig. 4.19, bottom panel). A vertical profile of the subpolar North Atlantic temperature and salinity (Fig. 4.20) reveals that it takes about 5 years for the surface signal to propagate downward, with no compensation occurring in the vertical. These observations are suggestive of the link between the ocean surface and sub-surface perturbations in hydrographic properties in the northern North Atlantic, in relation to low-frequency modes of variability (AMO, AMOC) (e.g., Delworth and Mann 2000, Dijkstra et al. 2006, Wang et al. 2010).

4.7 Summary and Conclusions

This chapter focuses on the vertical extension of the AMO signal in the deeper ocean and the link between surface variability and low-frequency changes in the North Atlantic thermohaline (density-driven) circulation. We have proposed an ocean heat content-based AMO index (AMO-HC) in an effort to capture the thermal state of the ocean (0-1000m heat content) and to understand the origin of AMO variability, especially its surface-subsurface link on decadal- to-multidecadal timescales in the North Atlantic basin. The most traditional SST based AMO index is found to lag the AMO-HC index by about 5 years, with maximum correlation of 0.69 at a 4-year lag when the two indices are smoothed (LOESS 25%). This lead of the heat content index over the SST index, along with the indication of a decadal respite in warming which is indicated by the subsurface index, has profound implications for both decadal prediction and more accurate estimations of the anthropogenic warming. In addition, the AMO timescale is found to shrink by about 25 years, when using the heat content based index to describe the phenomenon; this result suggests that the ocean circulation (via the thermal Rossby mode and/or ocean currents) is playing an active role in the integration of the ocean-atmosphere interactions associated with the AMO. Under this view, it is not surpising to find out that exists a coherent AMO evolution and northward excursions of the Gulf Stream that precede the AMO, as envisioned by Bjerknes (1964).

The AMO signal in the subsurface hydrographic properties is not the same in the entire subpolar Atlantic domain. In the Labrador basin, the potential temperature, salinity and potential density based only on temperature/salinity profiles indicate a downward propagation of positive, surface anomalies through time, with the penetration depth increasing as we move forward in time. Surface salinity maxima seem to precede surface temperature and are constrained to the top, near surface layers (~300-400m); fluctuations in the net density field are dominated by salinity changes. In the Irminger basin, changes in temperature and salinity do not compensate completely, leading to negative (lighter) potential density anomalies. Here, temperature appears to be more influential than salinity in determining the sign and magnitude of the potential density fluctuations. As both cold-fresh (negative density) anomalies in the Labrador Sea during the negative phase of the AMO, and warm-salty (negative density) anomalies in the Irminger Sea during the positive phase of the AMO mix downward, wind-induced turbulent mixing must dominate; AMO's temperature and salinity anomalies take about 8 years to reach a depth of approximately 400m. A year-to-year variability is also noted in both basins, when focusing on season-to-season variations, indicative of recurring wintertime SST anomalies that are being sequestered below the seasonal thermocline during the spring and summer seasons and re-emerge in the following late fall/early winter.

Finally, while the evolution of the AMO-related oceanic anomalies seem to be associated with surges of the Gulf Stream, the NAO seems to be linked with the AMO via the Gulf Stream. It is found that the Gulf Stream Index leads both the AMO-HC and traditional SST based AMO indices by 10 (35) seasons, but it lags the NAO index by 4-8 seasons; the lagged relationship with the NAO-wind forcing is consistent with enhanced or reduced Ekman transports within the North Atlantic basin, indicative of a potential mechanistic interaction between the AMO, NAO and the GSI.

Figure 4.1. Topography of northern North Atlantic Ocean. The acronyms of the topographic features indicated in the figure are (from west to east): ER:Eirik Ridge, MAR: Mid-Atlantic Ridge, CGFZ: Charlie-Gibbs Fracture Zone, RR: Reykjanes Ridge, RHB: Rockall-Hatton Plateau and Rickall-Hatton Bank, RT: Rockall Trough, FBC: Faroe Bank Channel, WTH: Wyville Thomson Ridge. (*Atlantic Ocean Floor* by Heinrich Berann, 1977, National Geographic, 2012)

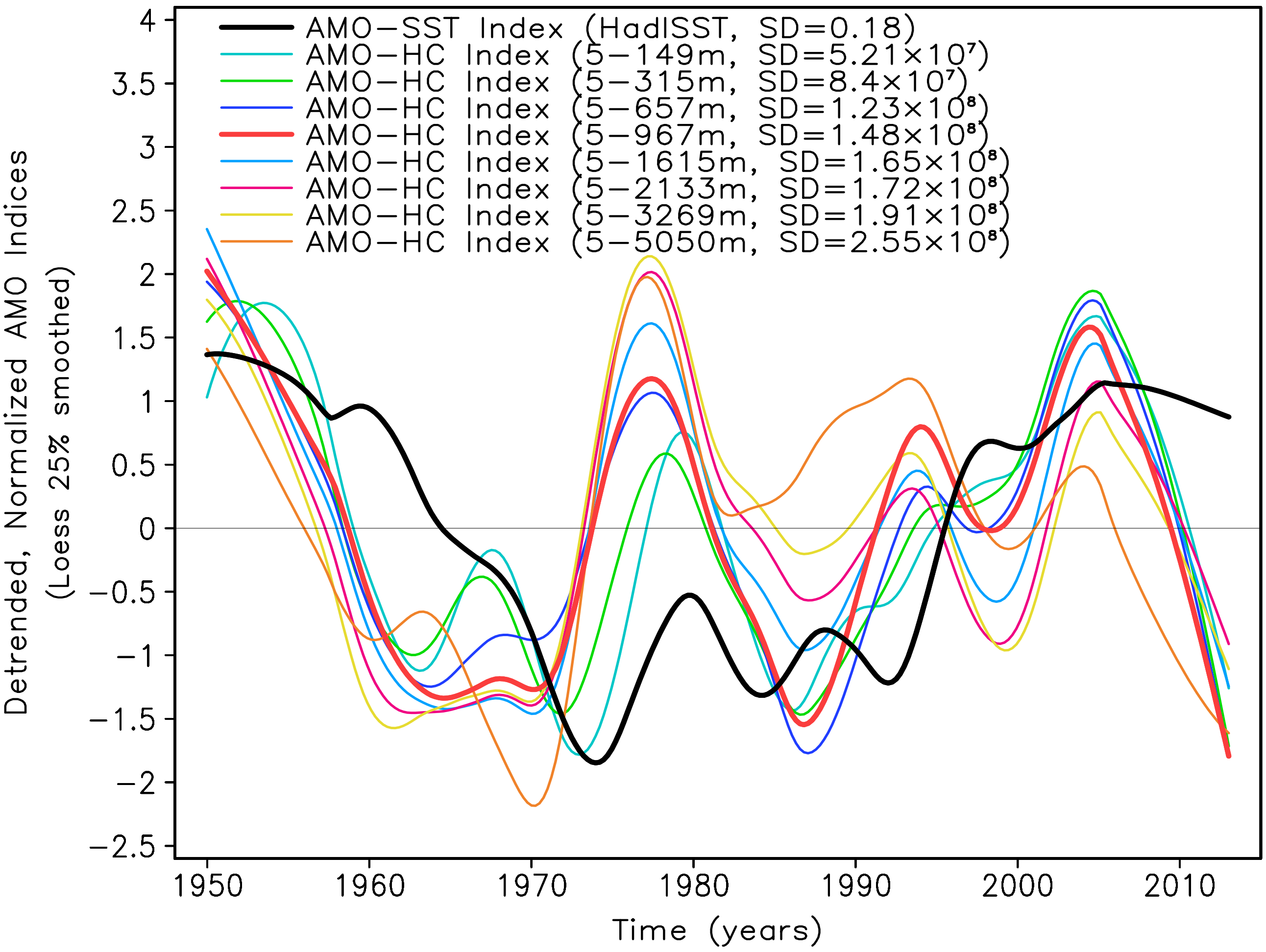

Figure 4.2 The plotted indices are calculated as the area average of seasonal SST and vertically-integrated heat content anomalies over the North Atlantic domain (75°W-5°E, 0°-60°N) for the January 1950- November 2013 period. They are shown after applying the LOESS 25% smoothing filter and subtracting the linear trend for the same, aforementioned time period. The de-trending is intended to remove the influence of greenhouse-gas induced global warming from the analysis. In addition, the standard deviation of the data points of each index from its corresponding mean value is also shown in parentheses (legend). In sum, we are showing the SST index from the HadISST v1.1 dataset and eight heat content (HC)-based indices from the EN4 v2.a dataset.

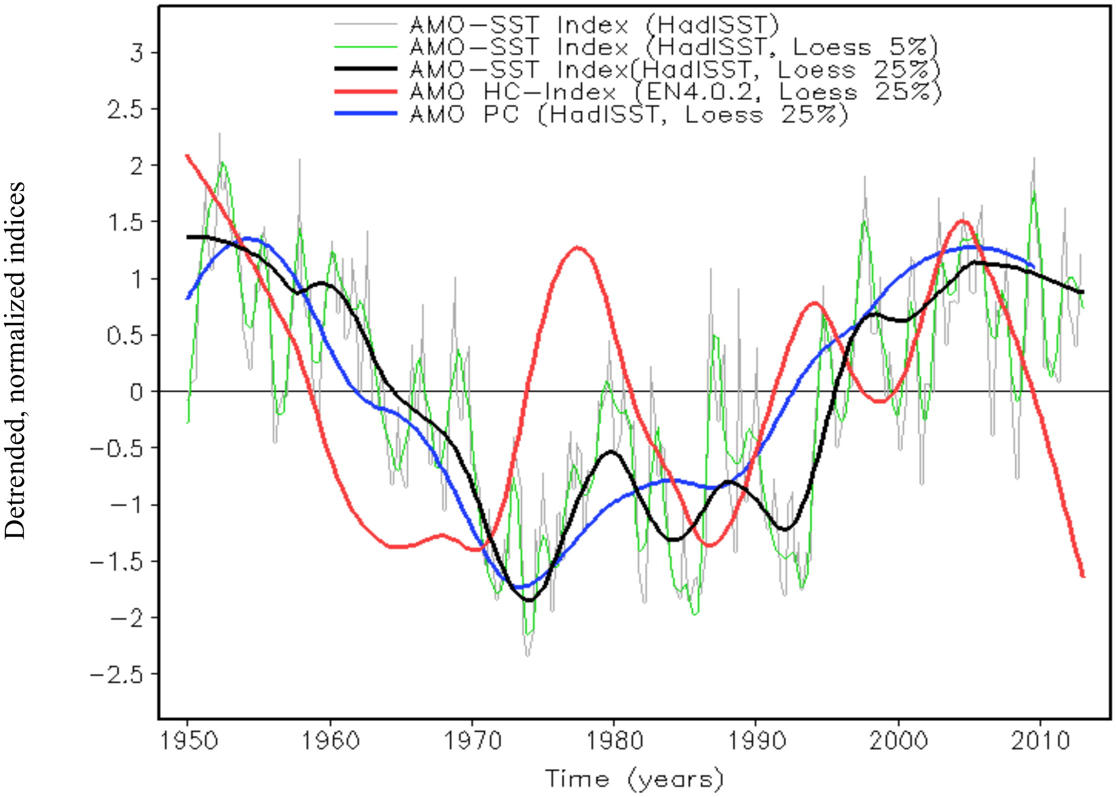

Figure 4.3 AMO-SST and AMO-HC, normalized indices are shown here for the period January 1950 – November 2013. Indices are calculated by spatially averaging seasonal anomalies over the North Atlantic domain (75°W-5°E, 0°-60°N) and subsequently de-trending them, by removing the linear trend calculated based on the least squares method and finally, normalizing them. The raw AMO-SST index (derived from the HadISST v1.1 dataset) is shown, along with two smoothed versions, one using a LOESS 5% filter and one using a LOESS 25% filter, to discern decadal vs. multidecadal signals, respectively. The AMO-HC index is calculated by spatially averaging seasonal, heat content anomalies over the same, aforementioned domain, and subsequently de-trending and smoothing them by a LOESS 25 % filter. The heat content anomalies are calculated by a. vertically integrating subsurface temperatures (EN4 .0.2 dataset) from 5m to 967m depth and b. removing the long-term seasonal mean.

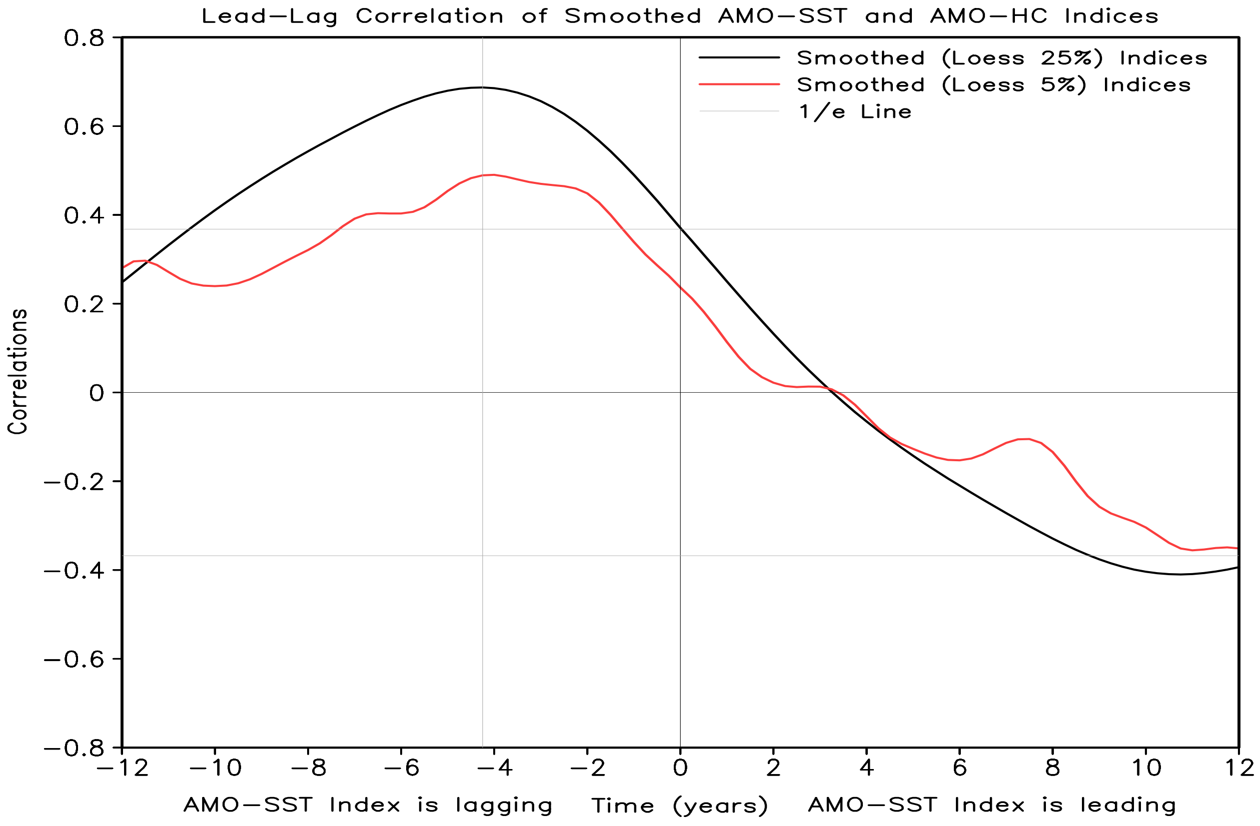

Figure 4.4 Lead-Lag Correlations of AMO-SST index smoothed by LOESS 5% (25%) with AMO-HC index, smoothed by LOESS 5% (25%), respectively, are shown for a lead-lag period of T-12 to T+12 years. Positive (negative) correlations indicate that the AMO-SST index is leading (lagging) the subsurface (AMO-HC) index.

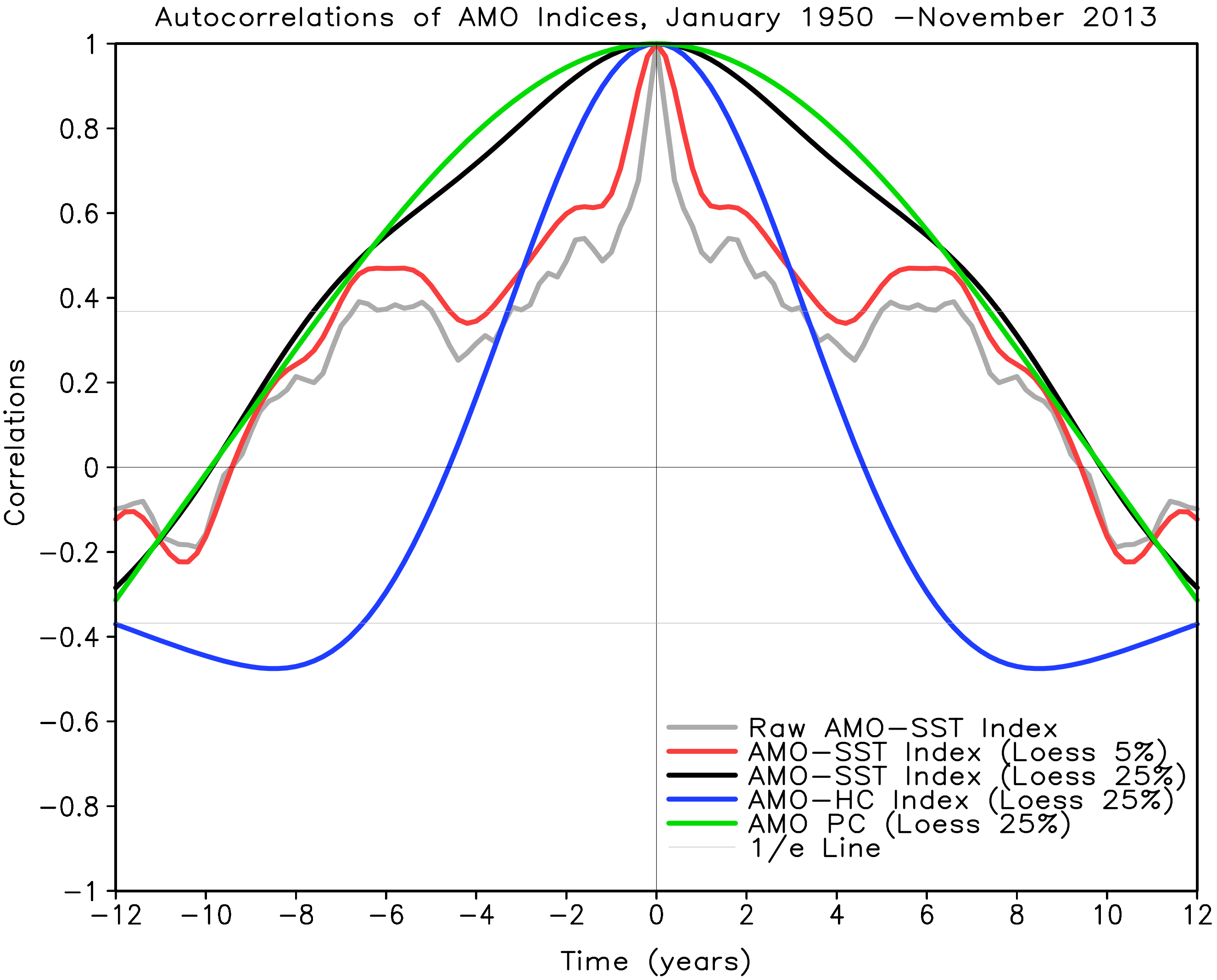

Figure 4.5 Autocorrelations of AMO-SST indices from the HadISST v1.1 dataset (raw, smoothed by LOESS 5%, smoothed by LOESS 25%), AMO-HC index (EN4.0.2) smoothed by LOESS 25% and finally AMO principal component (PC) smoothed by LOESS 25%. The indices are calculated as in Fig 1. The AMO PC is derived from an EEOF analysis (Guan and Nigam, 2009). Autocorrelations are shown for a time span of T-12 to T+12 years.

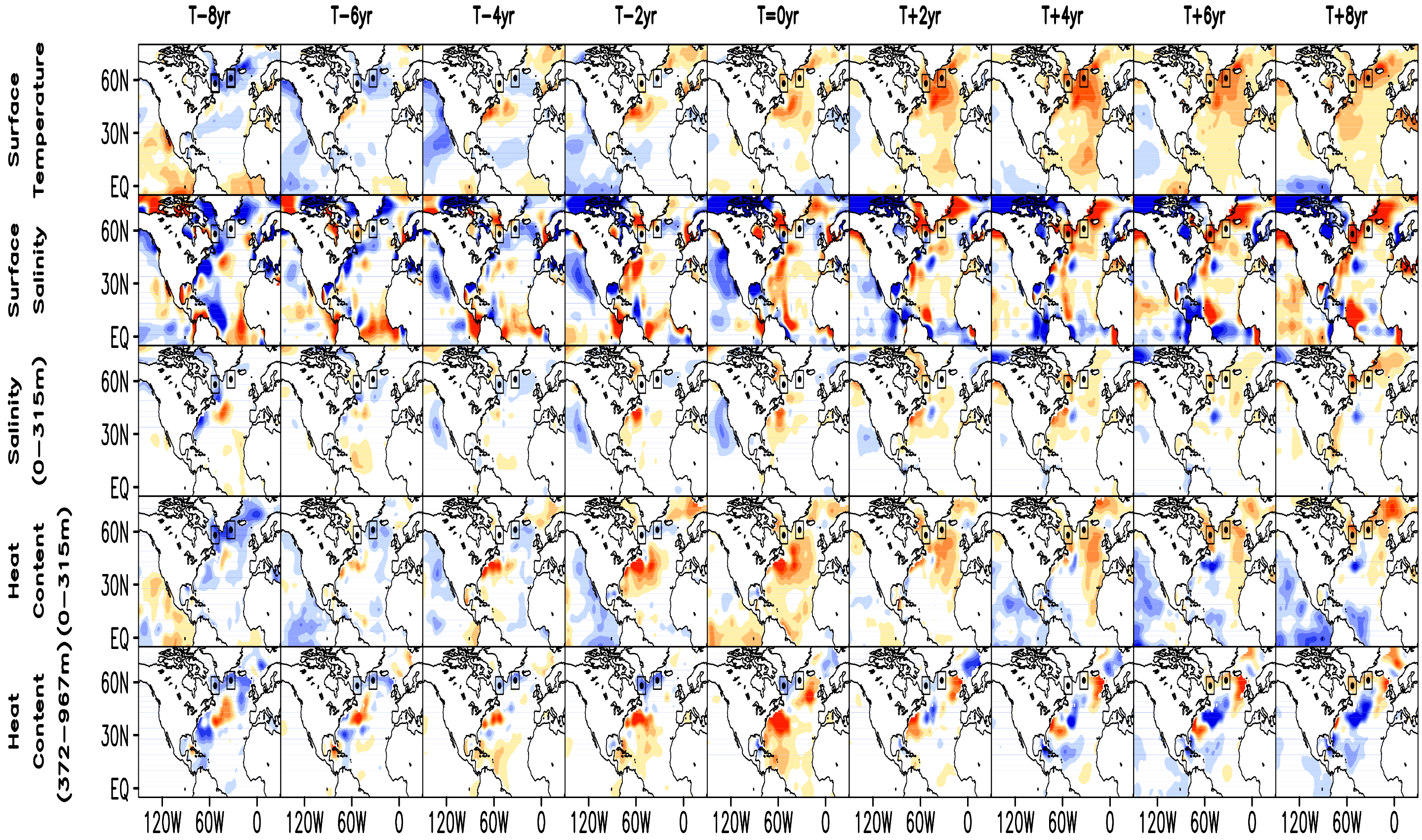

Figure 4.6 Lead-Lag regressions of sea surface temperature (HadISST, v1.1), EN4.0.2 surface and 0-315m vertically averaged salinity, 5-315m and 372-967m vertically integrated heat content on smoothed (by a 5% LOESS filter) and normalized by its standard deviation, heat content (5-967m)-AMO index (EN4.0.2). Regressions are calculated for the period January 1950 –November 2013 and are shown for a time span of T-8 to T+8 years, after 5 applications of the smooth9 function in the Grads plotting software. The contour intervals are: 0.05K, 0.01 PSU and $5\times10^{7}07$ J/m^{2}, respectively. The boxed areas and marked grid points represent two regions, one over the Labrador Sea (48°-58°W, 53°-63°N, Grid point: 53°W, 58°N) and one over the Irminger basin (28°-38°W, 56°-66°N, Grid point: 33°W, 61°N).

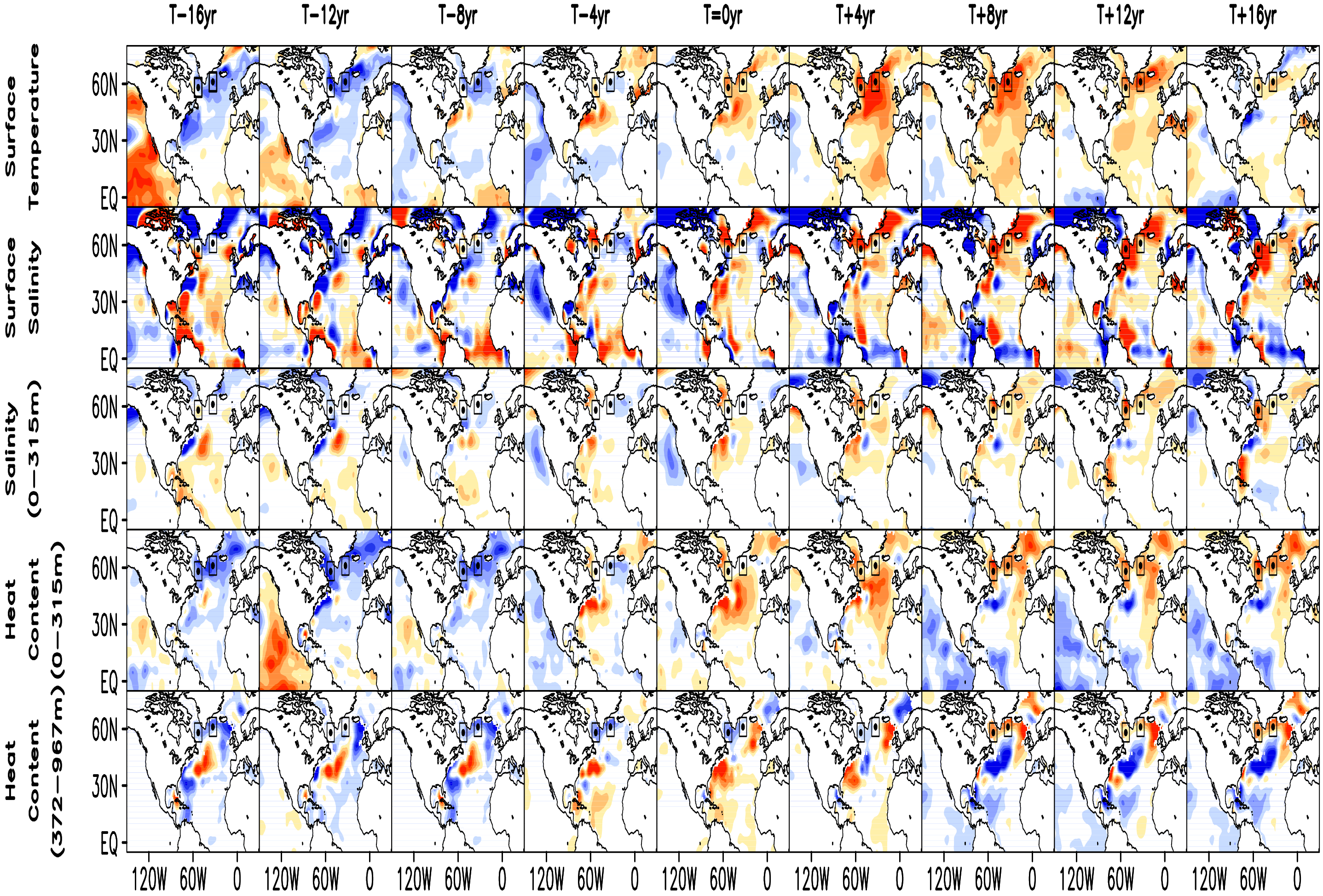

Figure 4.7 Lead-Lag regressions of sea surface temperature (HadISST, v1.1), EN4.0.2 surface and 0-315m vertically averaged salinity, 5-315m and 372-967m vertically integrated heat content on smoothed (by a 25% LOESS filter) and normalized by its standard deviation, heat content (5-967m)-AMO index (EN4.0.2). Regressions are calculated for the period January 1950 –November 2013 and are shown for a time span of T-16 to T+16 years, after 5 applications of the smooth9 function in the Grads plotting software. The contour intervals are: 0.05K, 0.01 PSU and 5×10^{7}07 J/m^{2}, respectively. The boxed areas and marked grid points represent two regions, one over the Labrador Sea (48°-58°W, 53°-63°N, Grid point: 53°W, 58°N) and one over the Irminger basin (28°-38°W, 56°-66°N, Grid point: 33°W, 61°N).

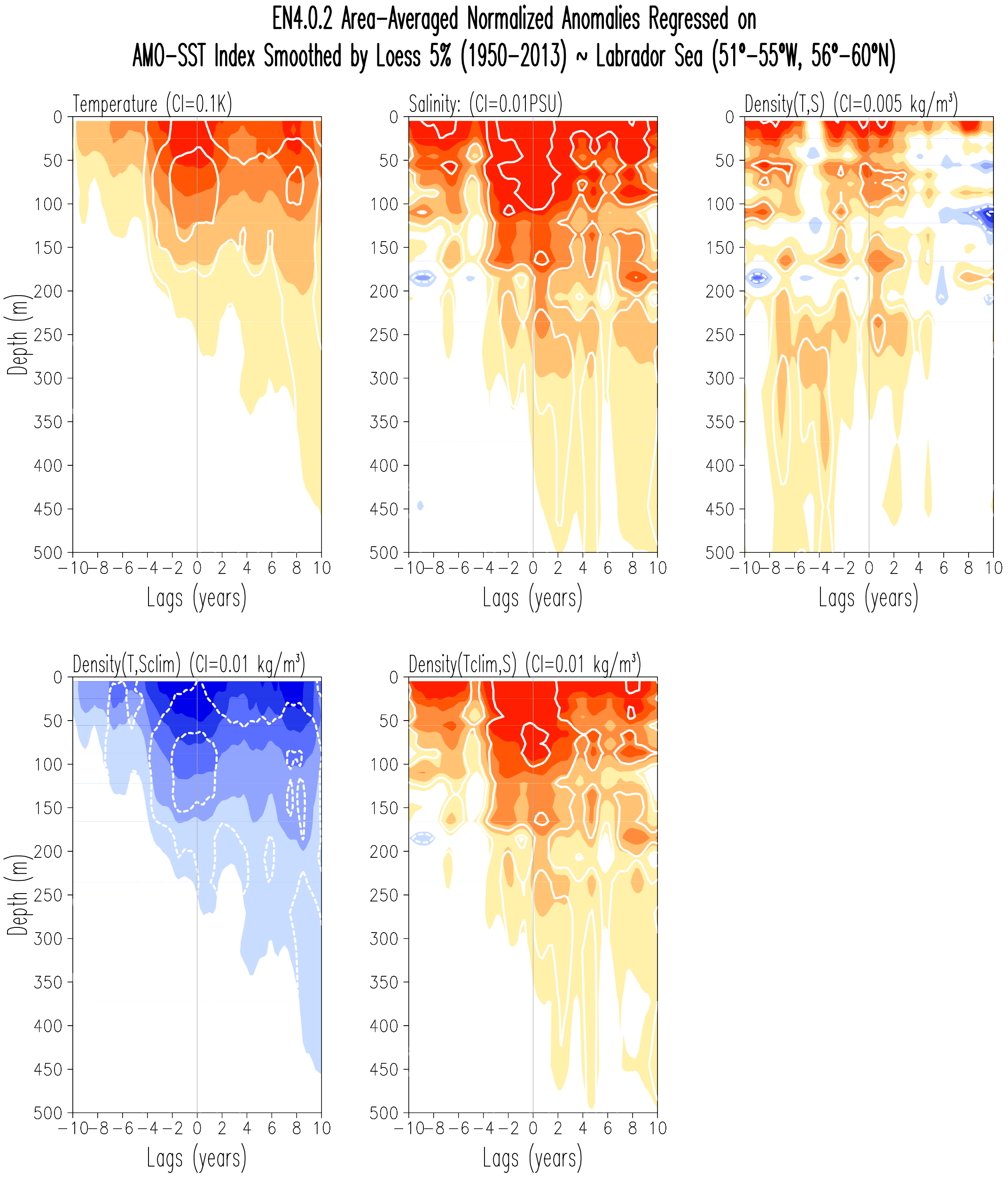

Figure 4.8 Profiles of lead-lag regressions/correlations of potential temperature, salinity and potential density on normalized smoothed (LOESS 5%) AMO-SST index. Density in the upper row is calculated by using both the anomalous temperature and salinity, while density in the lower left panel is calculated using only the anomalous temperature while maintaining the climatological salinity, and density in the lower right panel is calculated using only the anomalous salinity while maintaining the climatological temperature. All fields are products of the EN4.0.2 dataset. Regressions are calculated for the period January 1950- November 2013 and shown for a span of T-10 to T+10 years and a depth of 0-500m. We have used one application of the smooth9 function in the Grads plotting software. Profiles are shown for the boxed area: 51-55°W, 56-60°N in the Labrador Sea region. Correlations are shown as white contour lines with contour interval 0.1.

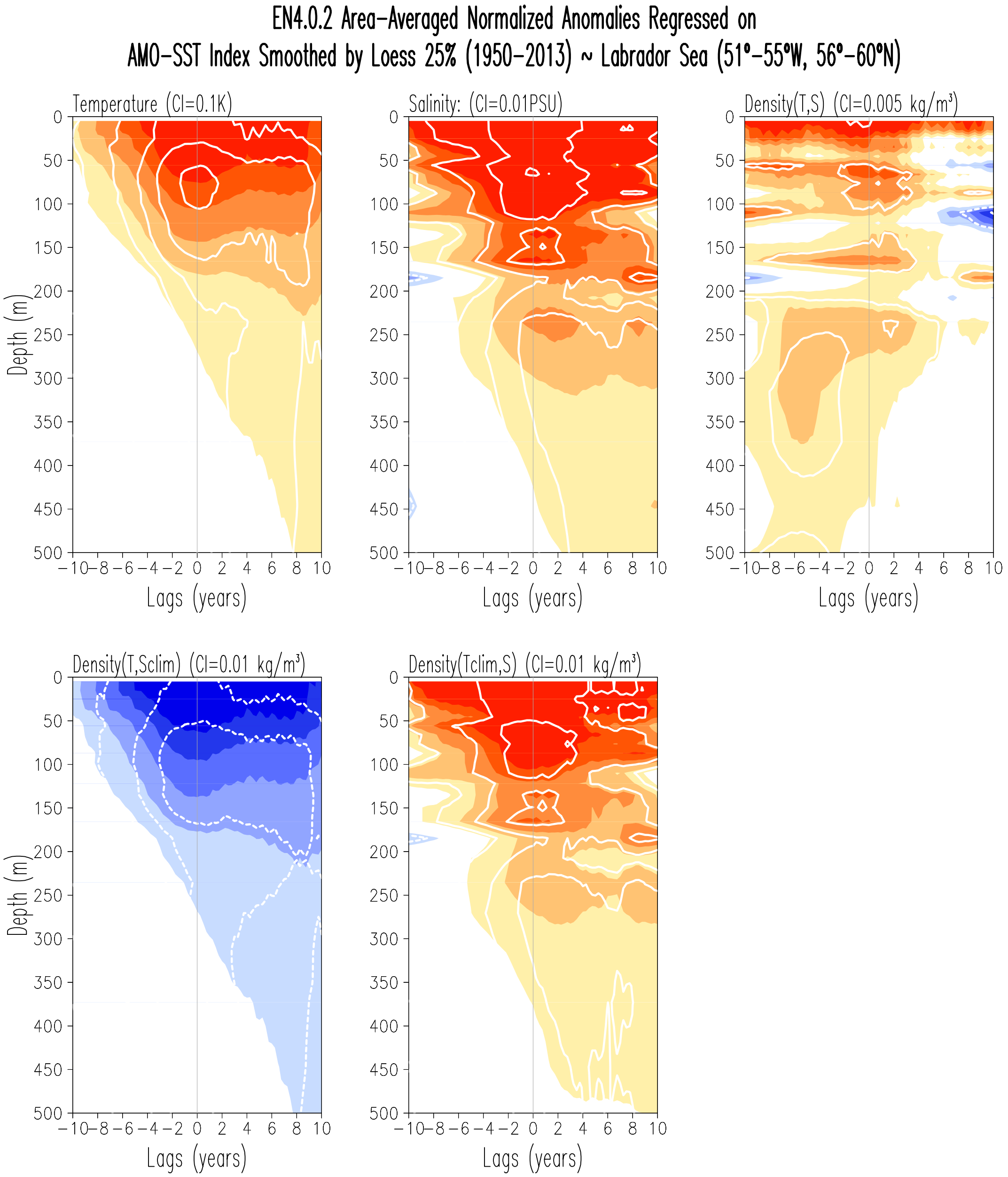

Figure 4.9 Profiles of lead-lag regressions/correlations of potential temperature, salinity and potential density on normalized smoothed (LOESS 25%) AMO-SST index. Positive (negative) values correspond to AMO leading (lagging) the potential temperature/salinity /potential density field. Density in the upper row is calculated by using both the anomalous temperature and salinity, while density in the lower left panel is calculated using only the anomalous temperature while maintaining the climatological salinity, and density in the lower right panel is calculated using only the anomalous salinity while maintaining the climatological temperature. All fields are products of the EN4.0.2 dataset. Regressions are calculated for the period January 1950- November 2013 and shown for a span of T-10 to T+10 years and a depth of 0-500m. We have used one application of the smooth9 function in the Grads plotting software. Profiles are shown for the boxed area: 51-55°W, 56-60°N in the Labrador Sea region. Correlations are shown as white contour lines with contour interval 0.1.

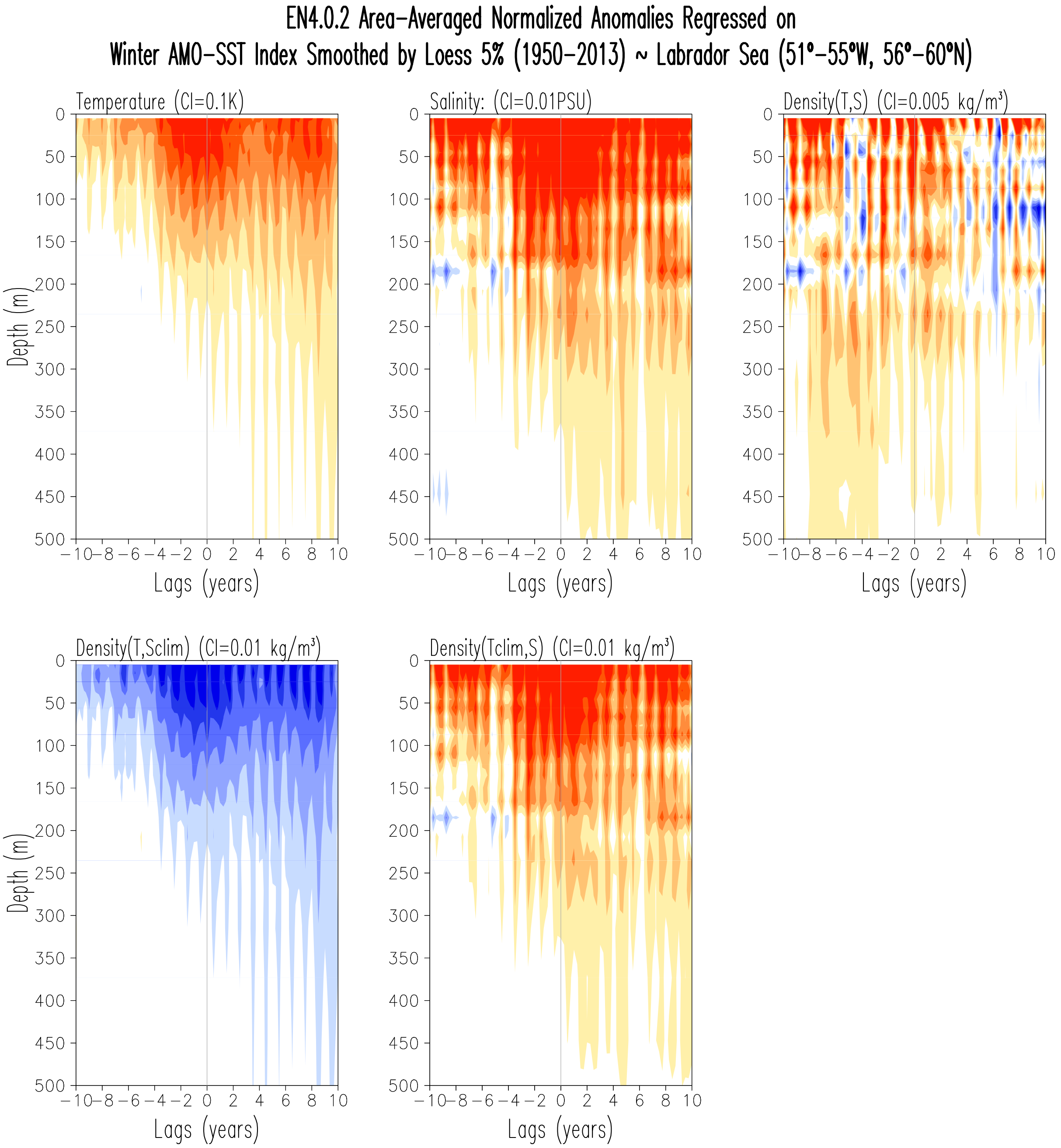

Figure 4.10 Profiles of lead-lag regressions of potential temperature, salinity and potential density on normalized smoothed (LOESS 5%) AMO-SST index for winter only. Density in the upper row is calculated by using both the anomalous temperature and salinity, while density in the lower left panel is calculated using only the anomalous temperature while maintaining climatological salinity, and density in the lower right panel is calculated using only anomalous salinity while maintaining climatological temperature. All fields are products of the EN4.0.2 dataset. Regressions are calculated for the period January 1950- November 2013 and shown for a span of T-10 to T+10 years and a depth of 0-500m. We have used one application of the smooth9 function in the Grads plotting software. Profiles are shown for the grid point 51-55°W, 56-60°N in the Labrador region.

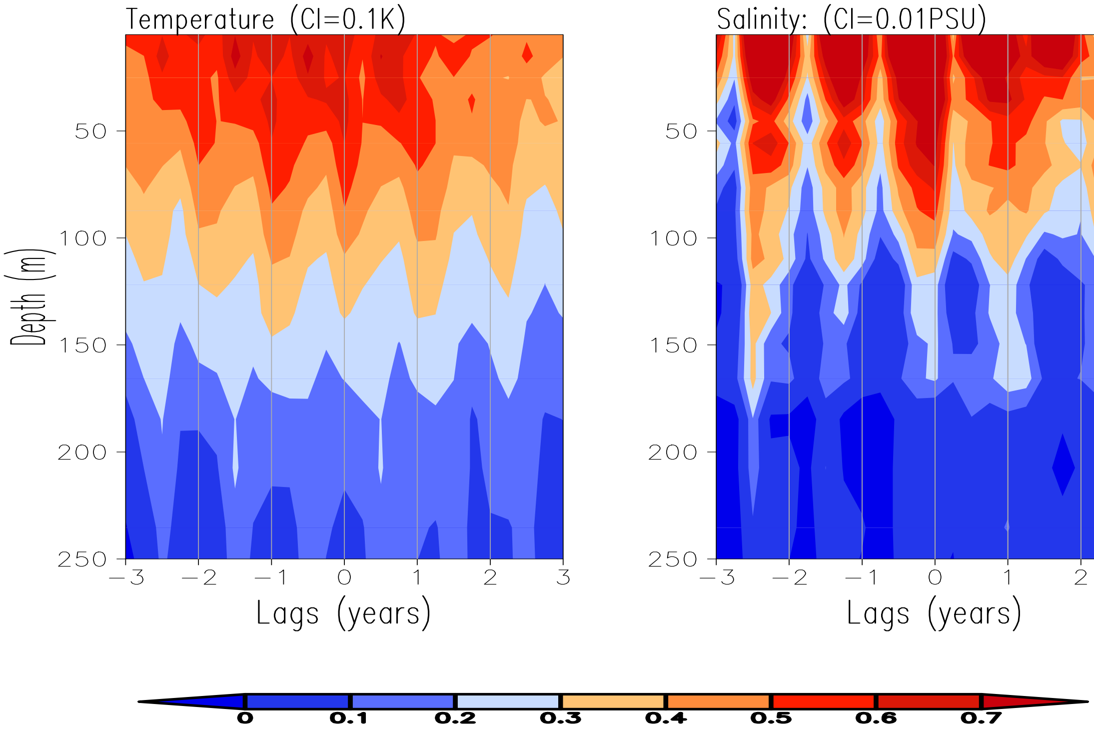

Figure 4.11 Profiles of lead-lag regressions of potential temperature and salinity on smoothed (LOESS 5%) and normalized AMO index for winter. All fields are products of the EN4.0.2 dataset. Regressions are calculated for the period January 1950- November 2013 and shown for a span of T-3 to T+3 years and a depth of 0-250m. We have used one application of the smooth9 function in the Grads plotting software. Profiles are shown for the grid point 51-55°W, 56-60°N in the Labrador region; vertical lines mark winter.

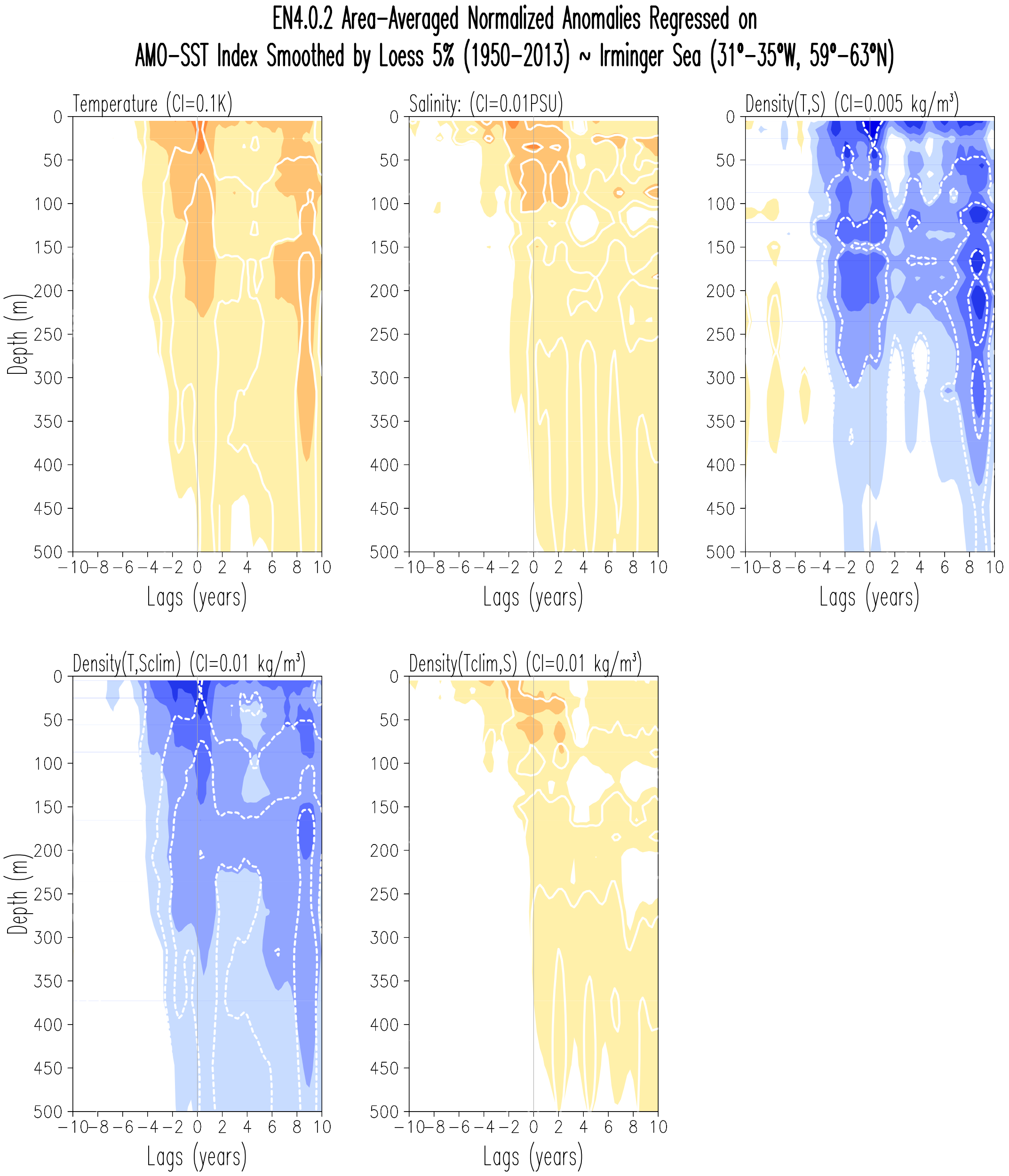

Figure 4.12 Profiles of lead-lag regressions/correlation of potential temperature, salinity and potential density on normalized smoothed (LOESS 5%) AMO-SST index. Positive (negative) values correspond to AMO leading (lagging) the potential temperature/salinity /potential density field. Density in the upper row is calculated by using both the anomalous temperature and salinity, while density in the lower left panel is calculated using only the anomalous temperature while maintaining climatological salinity, and density in the lower right panel is calculated using only anomalous salinity while maintaining climatological temperature. All fields are products of the EN4.0.2 dataset. Regressions are calculated for the period January 1950- November 2013 and shown for a span of T-10 to T+10 years and a depth of 0-500m. We have used one application of the smooth9 function in the Grads plotting software. Profiles are shown for the grid point 57°W, 61°N in the Irminger Sea region. Correlations are shown as white contour lines with contour interval 0.1.

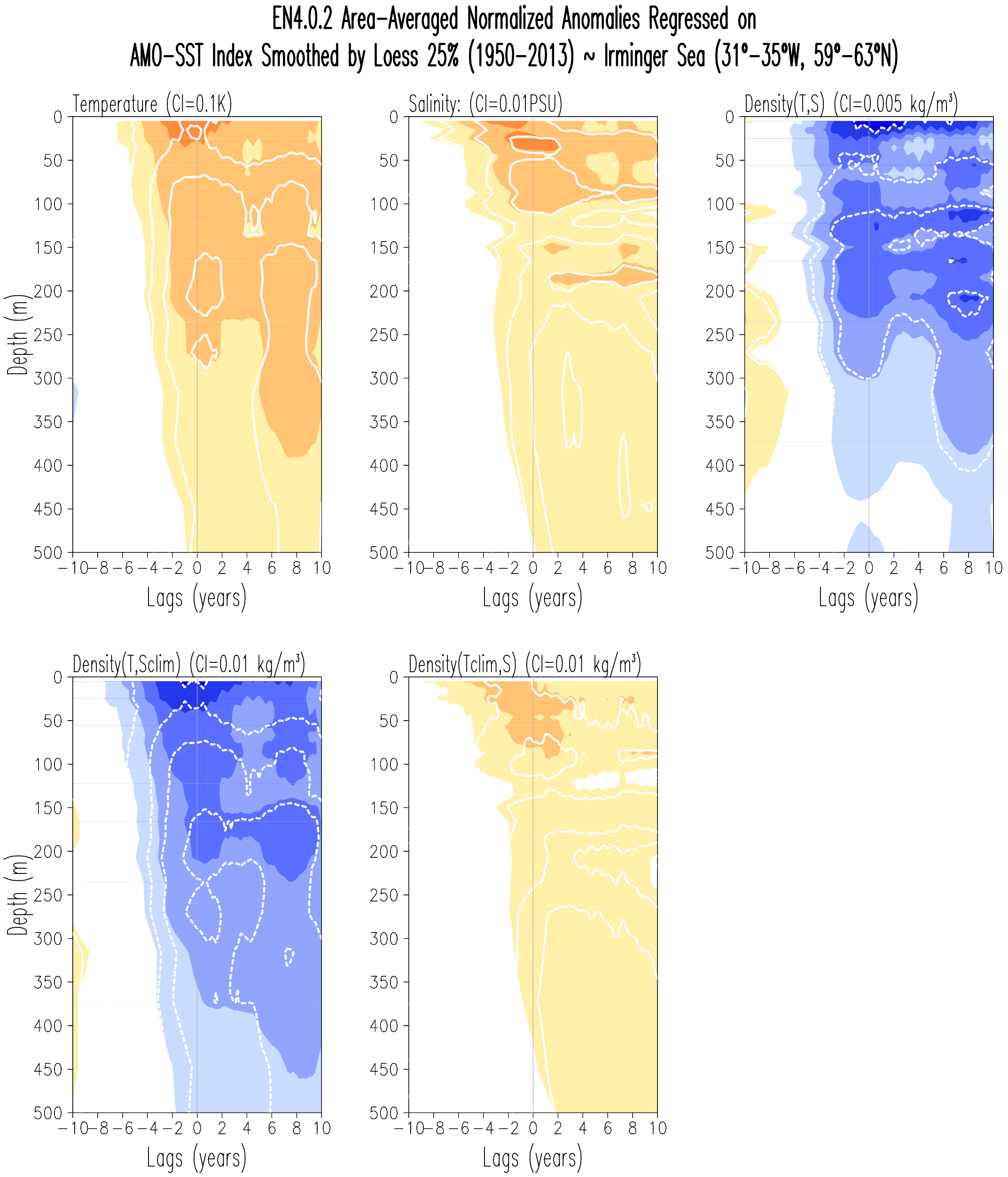

Figure 4.13 Profiles of lead-lag regressions/correlation of potential temperature, salinity and potential density on normalized smoothed (LOESS 25%) AMO-SST index. Positive (negative) values correspond to AMO leading (lagging) the potential temperature/salinity /potential density field. Density in the upper row is calculated by using both the anomalous temperature and salinity, while density in the lower left panel is calculated using only the anomalous temperature while maintaining climatological salinity, and density in the lower right panel is calculated using only anomalous salinity while maintaining climatological temperature. All fields are products of the EN4.0.2 dataset. Regressions are calculated for the period January 1950- November 2013 and shown for a span of T-10 to T+10 years and a depth of 0-500m. We have used one application of the smooth9 function in the Grads plotting software. Profiles are shown for the grid point 57°W, 61°N in the Irminger Sea region. Correlations are shown as white contour lines with contour interval 0.1.

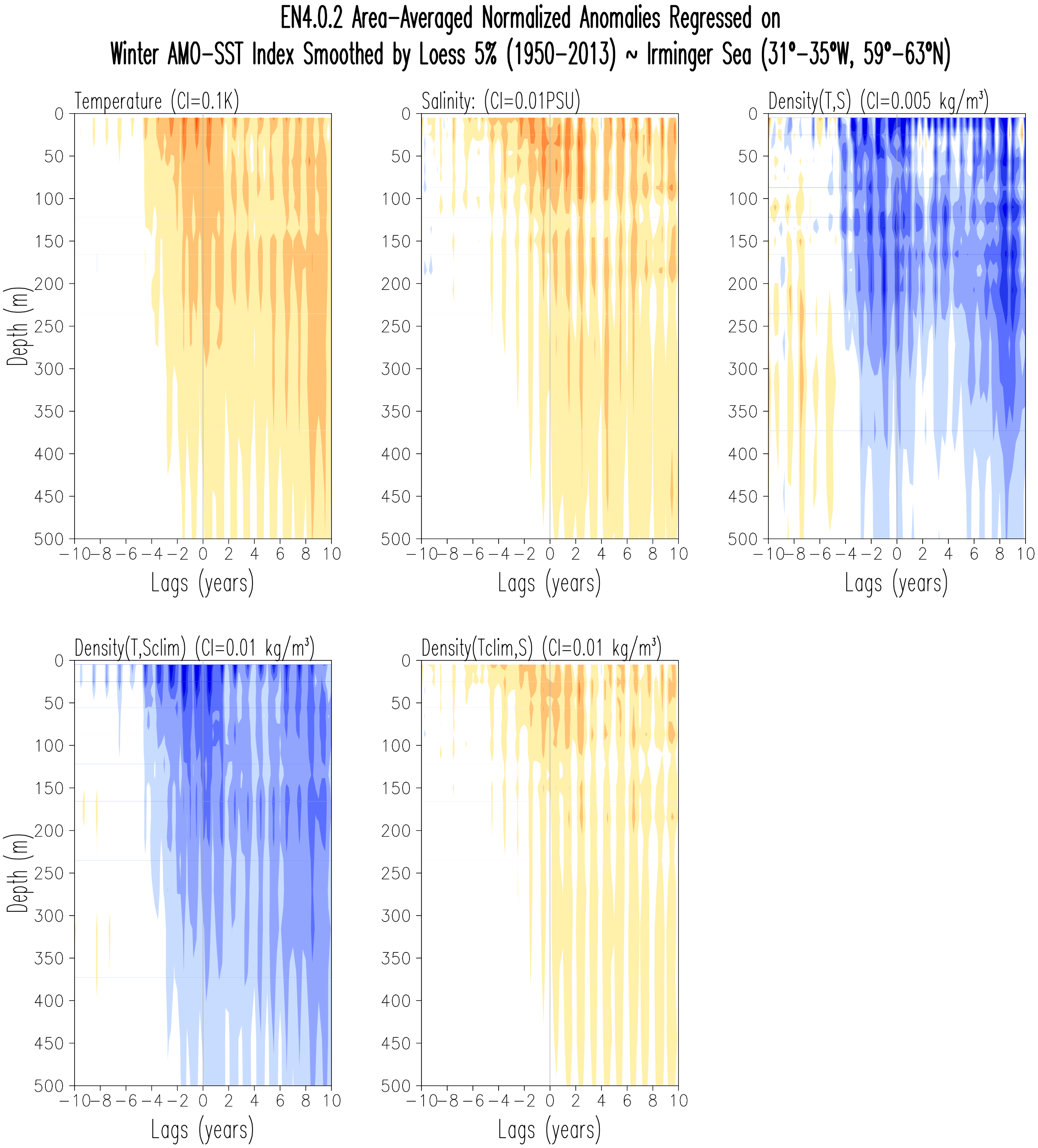

Figure 4.14 Profiles of lead-lag regressions of potential temperature, salinity and potential density on normalized smoothed (LOESS 5%) AMO-SST index for winter only. Density in the upper row is calculated by using both the anomalous temperature and salinity, while density in the lower left panel is calculated using only the anomalous temperature while maintaining climatological salinity, and density in the lower right panel is calculated using only anomalous salinity while maintaining climatological temperature. All fields are products of the EN4.0.2 dataset. Regressions are calculated for the period January 1950- November 2013 and shown for a span of T-10 to T+10 years and a depth of 0-500m. We have used one application of the smooth9 function in the Grads plotting software. Profiles are shown for the grid point 31-35°W, 59-63°N in the Irminger region.

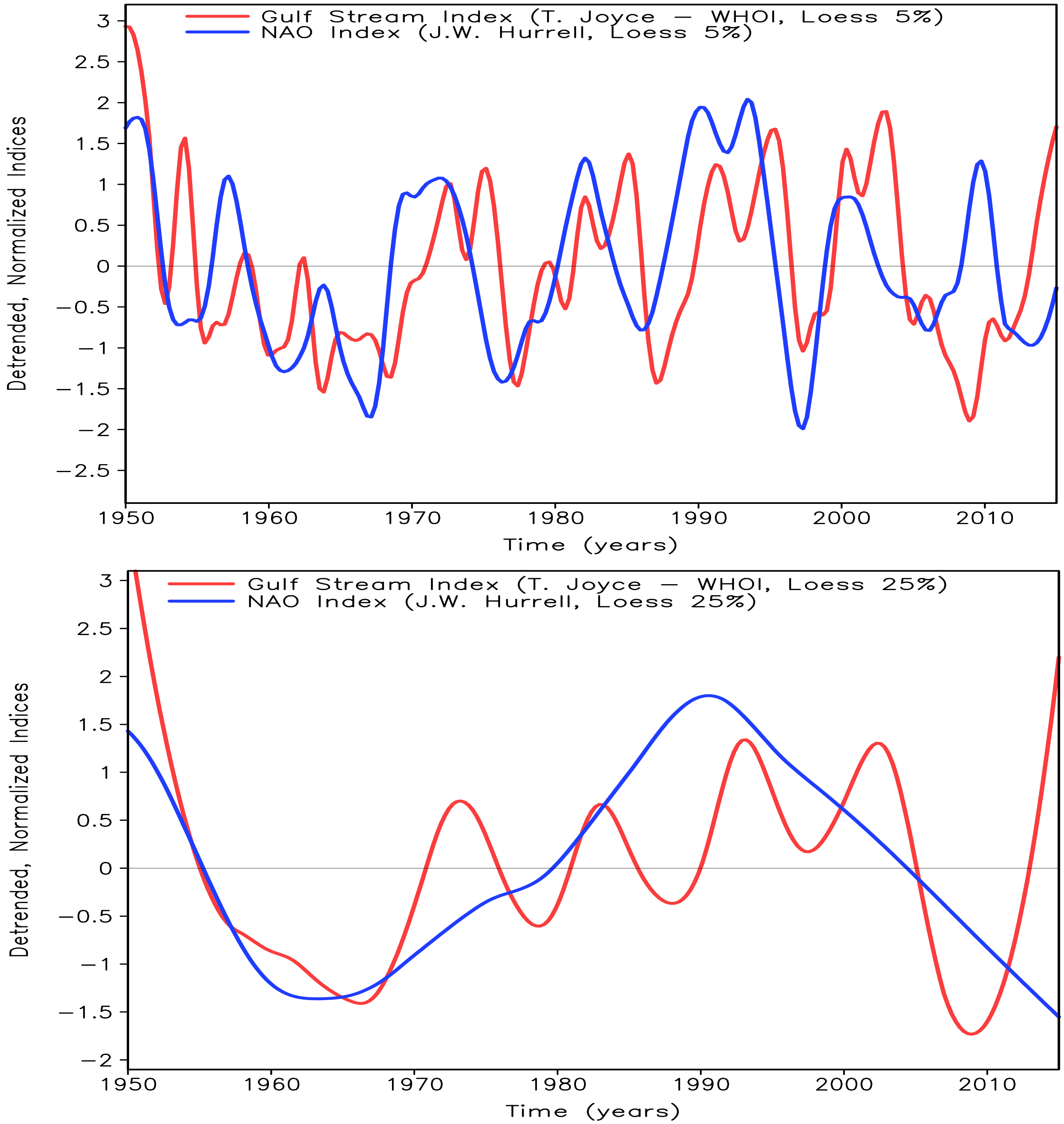

Figure 4.15 Time series of the Gulf Stream (GSI) (Joyce 2013) and NAO indices (Hurrell et al. 1995) are shown after having been de-trended by subtracting the linear trend for the period January 1954-October 2012 (common period among the data sets), smoothed by using LOESS 5% (25%) in the top (bottom) panel and finally normalized by dividing by the standard deviation. At t=0, correlation between the GSI and NAO-Hurrell is 0.58 for the LOESS 25% case and 0.40 for the LOESS 5% smoothed indices.

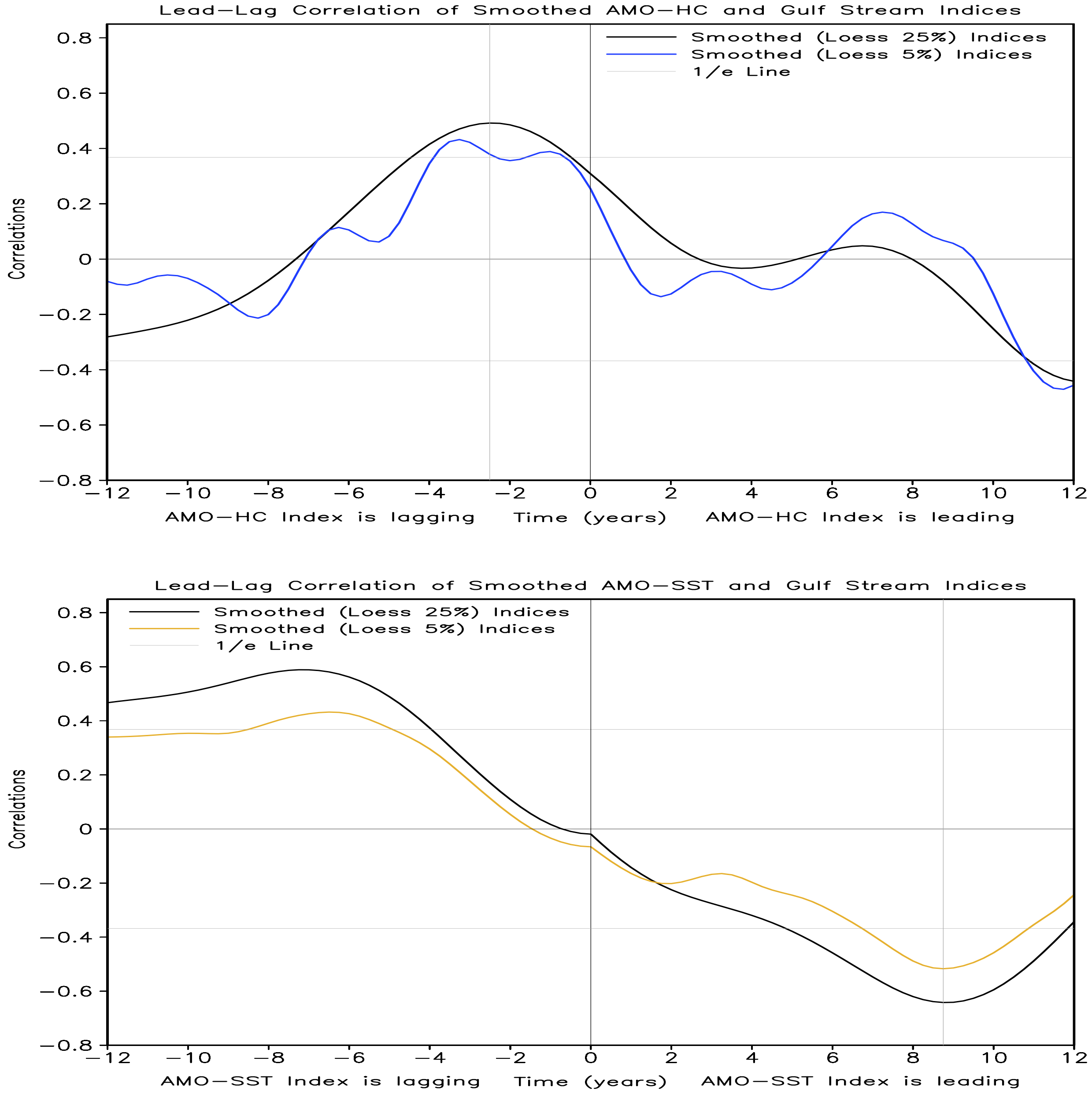

Figure 4.16. Lead-Lag Correlations of AMO-SST index smoothed by LOESS 5% (25%) with AMO-HC and Gulf Stream indices, smoothed by LOESS 5% (25%) respectively are shown for a lead-lag period of T-12 to T+12 years. Positive (negative) correlations indicate that the AMO-SST index is leading (lagging) the subsurface (AMO-HC) and Gulf Stream indices.

Regressions of NAO (Hurrell et al. 2005) (smoothed, LOESS 5%) on MSLP, 1954-2012

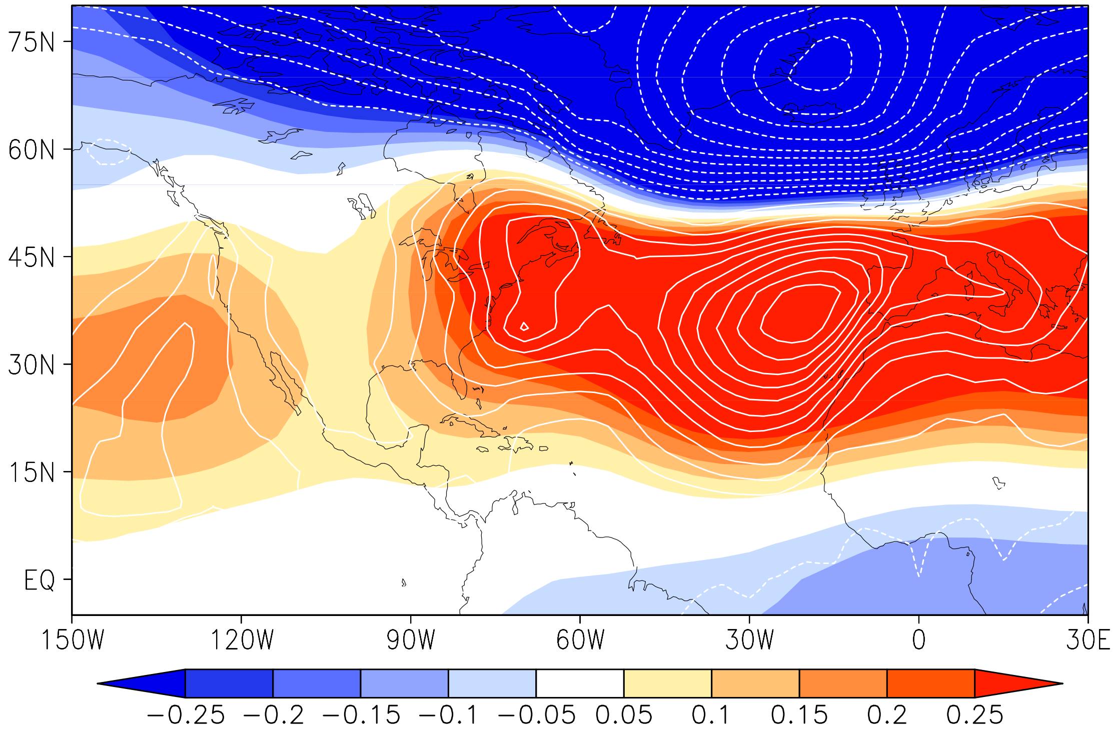

[10]

Regressions of GSI (Joyce 2013) (smoothed, LOESS 5%) on MSLP, 1954-2012

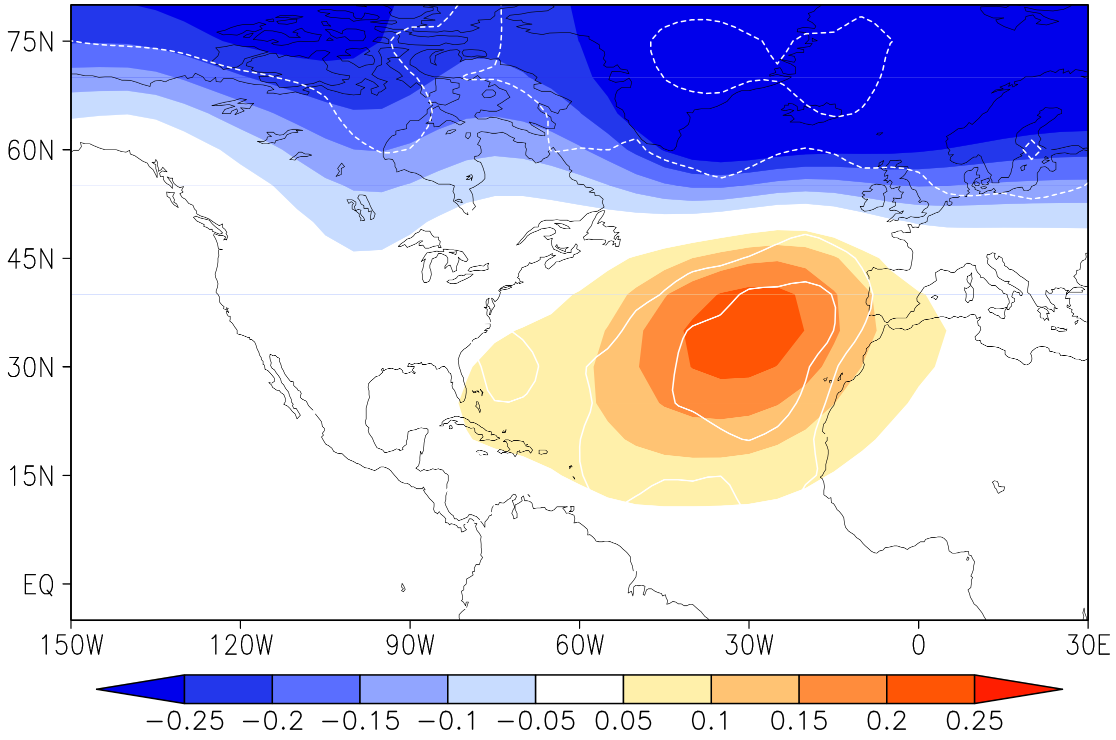

Figure 4.17 Simultaneous regressions (shaded blue-to-red) and correlations (white contours of 0.05) of smoothed (LOESS 5%) NAO (Gulf Stream) index on the seasonal, mean sea level pressure field, derived from the HadISST data set, for the January 1954 – October 2012 time period (common period between the different datasets).

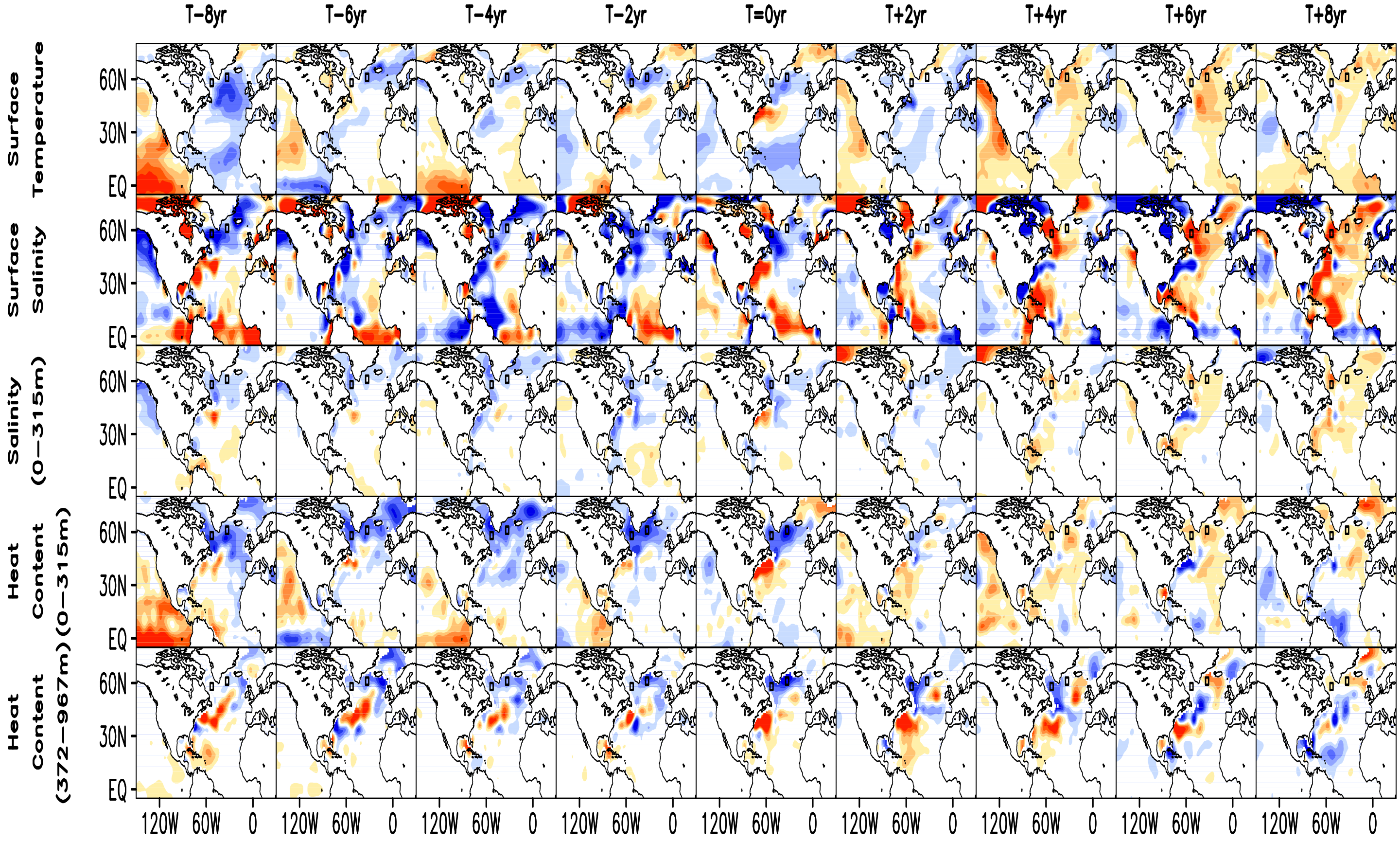

Figure 4.18 Lead-Lag regressions of sea surface temperature (HadISST, v1.1), EN4.0.2 surface and 0-315m vertically averaged salinity, 5-315m and 372-967m vertically integrated heat content on smoothed (by a 5% LOESS filter) and normalized by its standard deviation Gulf Stream index (T. Joyce). Regressions are calculated for the period January 1954 – November 2012 and are shown for a time span of T-8 to T+8 years, after 5 applications of the smooth9 function in the Grads plotting software. The contour intervals are: 0.05K, 0.01 PSU and 5×10^7 J/m^2, respectively. The boxed areas and marked grid points represent two regions, one over the Labrador Sea (48°-58°W, 53°-63°N, Grid point: 53°W, 58°N) and one over the Irminger basin (28°-38°W, 56°-66°N, Grid point: 33°W, 61°N).

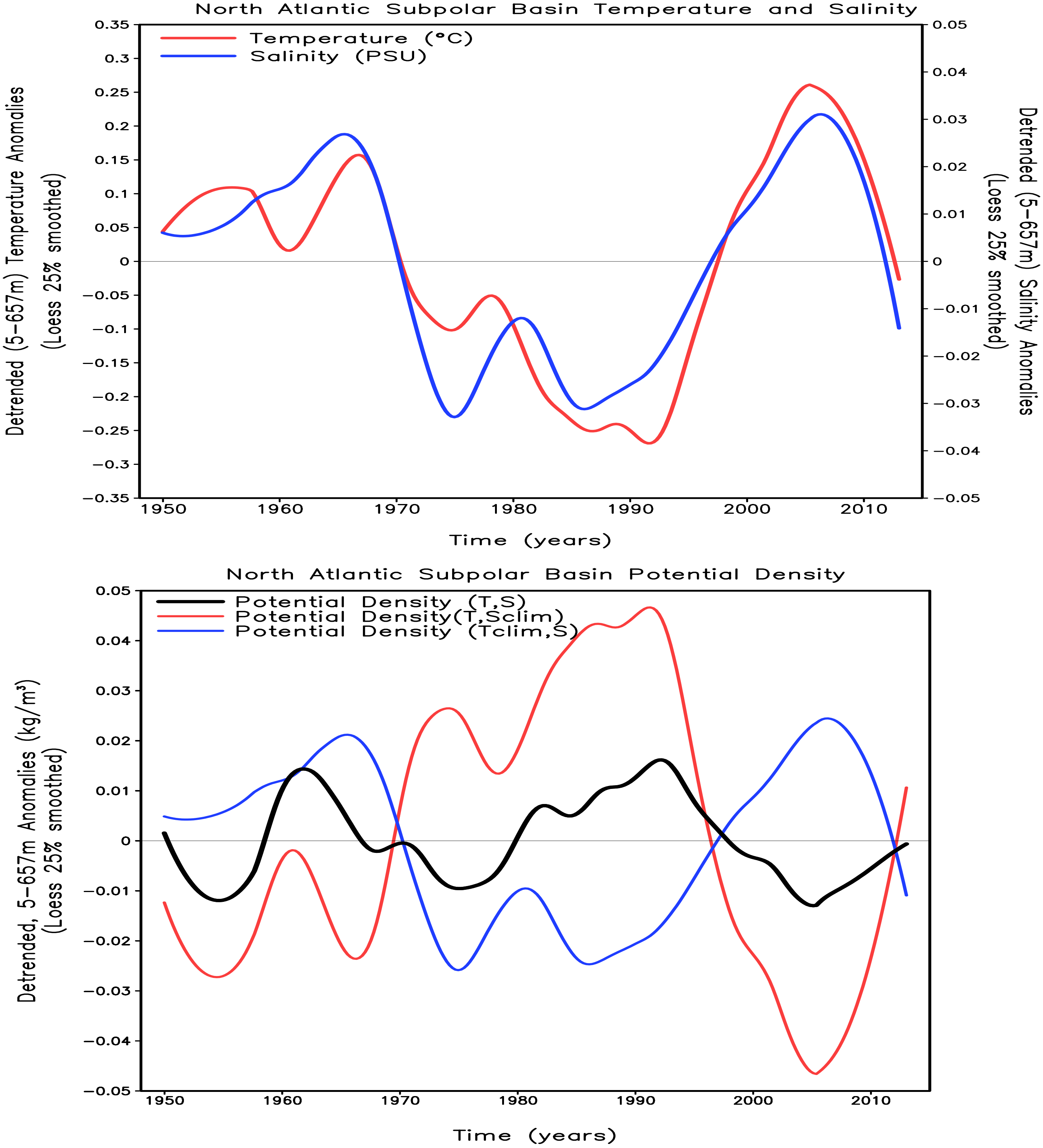

Figure 4.19 Vertically averaged (5-657m) temperature, salinity and potential density seasonal anomalies are spatially averaged over the North Atlantic Subpolar basin (75°W-5°E, 45°-75°N) and shown for the period January 1950-November 2013 after applying Loess 25% smoothing to detect the AMO-related, decadal to multidecadal pulses embedded in the time series. The EN4.0.2 temperature and salinity profiles are used to calculate the corresponding domain's potential density time series and the individual contributions of temperature and salinity.

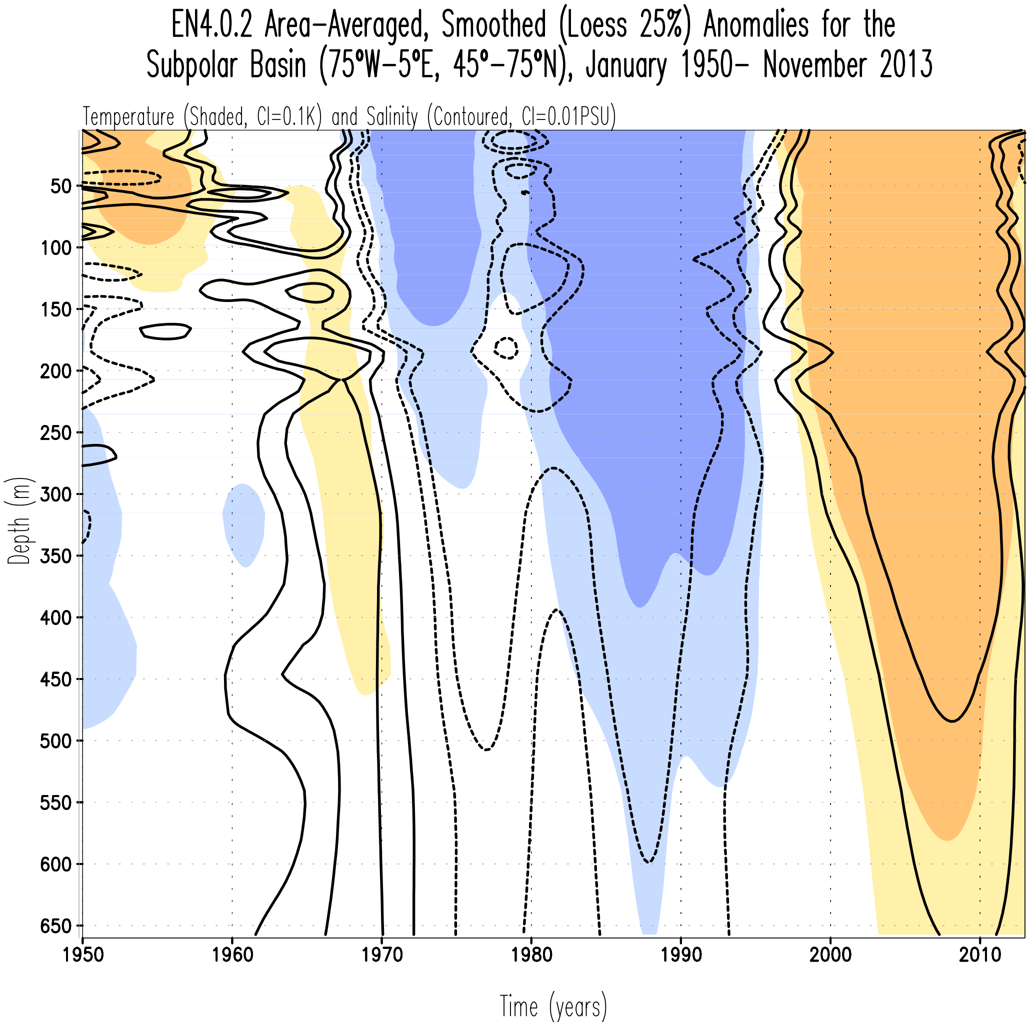

Figure 4.20 Depth versus time temperature (shaded blue-to-red) and salinity (contoured) profiles (EN4.0.2) are shown for the spatially averaged, seasonal anomalies over the North Atlantic Subpolar Basin (75°W-5°E, 45°-75°N) for the January 1950-November 2013 period. The profiles are smoothed using Loess 25% filter, to discern the decadal and multi-decadal pulses embedded in the AMO time series. We have used one application of the smooth9 function in the Grads plotting software. Positive (negative) salinity values are contoured using solid (dashed) black lines.

Chapter 5: Summary and Concluding Remarks

5.1 Outline and main issues

In this thesis, we have examined the variability of the North Atlantic Ocean on decadal to multidecadal timescales, focusing on the surface-subsurface thermohaline structure and the overlying atmospheric circulation (Chapter 2). The spatial pattern and time scale of the AMO has attracted considerable attention in recent decades, particularly in the context of the attribution of large-scale climate variations, such as the recent upward trend in Atlantic hurricane activity, the rapid increase in North Atlantic sea surface temperatures as well as in the frequency of extreme events. Additionally, there is growing debate on the origin of the AMO itself, especially the role of external forcing (i.e. aerosols) versus natural variability. Despite a growing body of literature on the characterization of AMO's spatiotemporal evolution and its impact on regional as well as global climate, there is considerable uncertainty and little consensus on the driving mechanisms of low frequency variability in North Atlantic thermal structure, especially the propagation of the temperature signal in the vertical.

Climate models remain challenged when it comes to portraying the AMO structure and evolution through time, as well as its hydroclimate impact over neighboring continents. Chapter 3 provides a detailed comparison of the CMIP3 vs. CMIP5 coupled ocean-atmosphere model simulations, along with a parallel comparison with observations, in an effort to assess any substantial improvements of the CMIP5 models over their CMIP3 versions in capturing decadal-to-multidecadal pulses in North Atlantic climate and in improving their decadal prediction skill of AMO's robust hydroclimate impacts.

Chapter 4, finally, seeks to characterize the AMO variability at deeper ocean levels, motivated by the prospect of detecting a pristine signature of AMO variability – one that is sequestered from atmospheric forcing (e.g., surface fluxes). Decadal-scale thermohaline pulses embedded in the AMO time series, along with AMO-related hydrographic changes are therefore targeted, with a particular focus on the subpolar North Atlantic basin and more specifically, the Labrador and Irminger Seas. The current study uses salinity and potential temperature data from the Met Office Hadley Center's EN4.0.2 dataset that extend to the present time, and consist of subsurface profiles derived from the ARGO global observing system, which is based on profiling floats and is complemented by Conductivity Temperature Depth (CTD) profilers and mooring data.

The central issues of the thesis can be summarized as follows:

- The 3-dimensional structure of the AMO, based on observations and CMIP5 20th century historical climate simulations (chapter 2).
- Uneven progress in the representation of AMO and its hydroclimate impact between CMIP3 and CMIP5 simulations of 20th century climate by coupled ocean-atmosphere-land-surface models (chapter 3).
- Proposed definition of the AMO, using (5-967m) vertically integrated heat content data, in an effort to capture low-frequency variability in the deeper ocean layers (chapter 4).
- Decadal-to-multidecadal variations in the thermohaline structure of the subpolar North Atlantic in relation to the AMO, with a particular focus on the Labrador and Irminger Seas (chapter 4).

- Link between AMO's decadal variability and meridional surges of the Gulf Stream, and thus with the low-frequency North Atlantic Oscillation.
- Hints of subpolar, North Atlantic subsurface cooling leading the surface during the past decade (chapter 4).

5.2 Summary and Concluding Remarks

A clarified description of AMO's spatiotemporal structure and evolution emerges from century-long observations. A period of 58 years is inferred for the smoothed AMO from observations, which is smaller than other estimations in the 65-75 years range (e.g., Enfield et al. 2001, Sutton and Hodson 2005); these other estimates are based on the use of heavy smoothing of the area-averaged SST anomalies, as compared with the 1-2-1 binomial filter used in chapter 2. Spectral analysis shows that oscillations in the 70-80 year range are dominant in the observed smoothed AMO index; these are combined with oscillations in the 30-40 year range and shorter periods. Models, however, underestimate the life span of the phenomenon by exhibiting more power in the 10-20 year range, to the extent that it becomes more dominant than variability in the 70-80 year range.

Sea surface temperature anomalies are shown to be associated with vertically-integrated heat content anomalies (sfc-400m) that evolve coherently in time, as well as vertically integrated (sfc.-50m) salinity anomalies - particularly the positive anomalies developing over the Labrador Sea and the negative ones off of the US coast. While this configuration of SST/salinity/heat content anomalies over the deep water formation region of the sub-polar gyre points toward a more active thermohaline circulation during the warm phase of the AMO, the cold phase of the AMO suggests a weaker thermohaline circulation and fresh water anomalies, similar to the ones evolving during Great Salinity Anomaly events. The atmospheric anomalies associated with the North Atlantic low-frequency SST variability was obtained from regressions of the seasonal AMO index on the 500 hPa geopotential height field. This regional height anomaly potentially includes the impact of synoptic transients (i.e., weather noise) which also influences regional SST evolution (through surface-flux modulation) as well as the feedback of the altered SST distribution on the atmosphere. The tropospheric height signal is stronger in winter and weaker during summer, but present year-round.

The fall season appears to be of critical importance as far as interactions between the AMO and the regional surface climate of the adjacent continents are concerned; an anomalous wave pattern extending from North America to eastern Europe is linked to reduced (enhanced) rainfall over large portions of the Americas (western Africa, over the Guinean region) and generalized warming over the western Americas, Greenland, Europe and northwestern Africa, during that season.

The modeled AMO structure that emerges via the CMIP5 historical simulations demonstrates limited success, particularly on the continental climate impact front. Furthermore, spatial correlations of the observed and simulated anomalies do not indicate significant improvement between the CMIP5 20th century climate simulations and their previous, CMIP3 versions. For instance, the representation of the mature warm phase of the AMO shows some improvement, but not across all the models. As far as the AMO timescale is concerned, while observations indicate a period close to 56 years, the NCAR, GFDL and MPI CMIP3 and CMIP5 models underestimate this value, whereas the UKMO models go from exhibiting an extremely low period (~16 years) in their CMIP3 version to overestimation (~68 years) in their CMIP5 version. It is clear that both sets of models underestimate low frequency variability in the 70-80 and 30-40 year ranges, while overestimating variability at higher frequencies (10-20 year range). Finally, analysis of the AMO regressions in model simulations reveals no significant CMIP3-to-CMIP5 improvement in the related oceanic and hydroclimate impacts. Pattern correlations with observed SST and precipitation anomalies are smaller in CMIP5 than in the CMIP3 simulations in both summer and fall!

The final chapter of the thesis focuses on the vertical extension of the AMO signal in the deeper ocean and the link between surface variability and low-frequency changes in the North Atlantic thermohaline (density-driven) circulation (THC). We have proposed a vertically integrated, ocean heat content AMO index definition, in an effort to capture the thermal state of the ocean (0-1000m heat content) and not just of the sea surface as in the canonical AMO-SST indices. The principal findings of this part of the analysis are:

- The AMO-SST index lags the AMO-HC index by about 5 years, with maximum correlation of 0.69, observed at a 4-year lag between the two smoothed (Loess 25%) time series.
- The AMO-HC index is suggestive of a cooling North Atlantic subsurface in the recent years (mid-2000s –present), a feature that is almost absent (minimal) from the ocean surface and one with significant implications in a) predicting future North Atlantic climate, b) attributing its variability to human versus natural fluctuations and forcing, and c) anticipating its co-variability with global climate, especially in the context of a recent slowdown in the rise of global average temperatures (hiatus) which was noted in the last assessment report of the IPCC.

- The AMO-HC index's lead over the SST index and its indication of a decadal respite in warming has profound implications for both decadal prediction and estimation of anthropogenic warming.
- The AMO timescale shrinks significantly (by almost 25 years) when estimated using the subsurface (i.e., heat-content) based index to describe the phenomenon; the timescale estimated using the surface (i.e., SST) based index, in contrast, is close to 50 years. The difference is potentially attributable to the *thermal Rossby mode,* an internal oceanic mode representing westward-propagating temperature anomalies in the ocean subsurface, with a period of 20-30 years. This propagation is not expected to be pronounced at the surface (i.e., manifest in SSTs) as it can be overwhelmed by the influence of atmospheric 'weather noise' and the presence of the eastward-propagating Gulf Stream. It can however remain uncorrupted at subsurface levels, and could possibly be responsible for the dominance of the 20-30-year time period in the AMO-HC index.
- Lead-lag regressions of AMO-HC index on SST and upper-ocean (5-315m) salinity and heat content reveal coherent AMO evolution beginning with northward excursions of the Gulf Stream, as envisioned by Vilhelm Bjerknes in 1964.
- In the Labrador basin, the potential temperature, salinity and potential density based only on temperature/salinity profiles indicate a downward propagation of positive, surface anomalies through time, with the penetration depth increasing as we move forward in time. Surface salinity maxima seem to precede surface temperature and are constrained to the top, near surface layers (~300-400m); fluctuations in the net density field are dominated by salinity changes.

- Thus, with positive salinity anomalies, the water density increases in the Labrador Sea, in the positive AMO phase.
- In the Irminger basin, changes in temperature and salinity do not compensate completely, leading to negative (lighter) potential density anomalies. Temperature appears to be more influential than salinity in determining the sign and magnitude of the potential density fluctuations.
- As both cold-fresh (negative density) anomalies in the Labrador Sea during the negative phase of the AMO, and warm-salty (negative density) anomalies in the Irminger Sea during the positive phase of the AMO mix downward, wind-induced turbulent mixing must dominate; AMO's temperature and salinity anomalies take about 8 years to reach a depth of approximately 400m.
- On seasonal timescales, we note year-to-year variability in both basins, indicative of recurring wintertime SST anomalies that are being sequestered below the seasonal thermocline during the spring and summer seasons and re-emerge in the following late fall/early winter. This is consistent with past studies on the *re*-emergence of wintertime SSTs (i.e. Cassou and Deser 2007, Deser et al. 2000).
- Salinity and temperature profiles are characterized by statistically significant correlations, at the given lags.
- Analysis of the vertically averaged (5-657m) thermohaline anomalies in the subpolar North Atlantic shows net density to track salinity (temperature) in the post (pre)-1980s period. It is shown that it takes about 5 years for the surface signals to propagate downward into the subsurface, with no compensation of the anomalies occurring in the vertical. This feature can be further explored in future research, both in context of North

Atlantic subsurface cooling in the 2005-onward period (Fig. 4.2) and the evolution of extreme interannual conditions in the subpolar North Atlantic, such as the years 2008 and 2012 (years with extremely cold winter seasons and a deeper, more expanded mixed layer, starting from the Labrador Sea, including all of the Irminger Sea and progressing southward along the coast of northeastern US).

- Finally, and importantly, our quest to understand the origin of AMO variability, especially its surface-subsurface variability on decadal-multidecadal timescales in the subtropical, midlatitude, and subpolar basins of the North Atlantic led us to the Gulf Stream, and its variability index (GSI, Joyce, WHOI, personal communication). Our analysis of GSI's temporal relationship with the AMO indices shows AMO's decadal variability to be linked with meridional surges of the Gulf Stream, and thus with the low-frequency NAO.
- The Gulf Stream Index is found to lead both the AMO-HC and AMO-SST indices by 10 (35) seasons, while lagging the NAO index by 4-8 seasons; the lagged relationship with the NAO-wind forcing is consistent with enhanced or reduced southward Ekman transports within the North Atlantic basin.

5.3 Future Research

The current work is in early stages in context of the understanding of AMO variability – its structure and mechanisms. Additional research will clearly be necessary to advance our understanding of AMO-related surface, subsurface and overlying atmosphere variability in various North Atlantic basins, and especially their links to the other slowly-varying phenomena in this basin. First, a more refined description of the links between thermohaline variability at the ocean's surface and the vertical propagation of AMO signals on intraseasonal-to-decadal and multidecadal timescales needs to be obtained from various observational data sets and climate simulations.

Much remains unknown also about the drivers of net sinking processes leading to different mixed layer depths in key regions, such as the Labrador and Irminger Seas. Second, an extended-EOF analysis of the AMO-HC is warranted as an index-based analysis is not keyed to spatiotemporal recurrence and inter-basin connections. Finally, the Gulf Stream's latitudinal shifts and their link to the North Atlantic atmospheric circulation and hydrographic changes in the northern latitudes require additional investigation.

A mechanistic model of the NAO-GSI-AMO decadal interaction is proposed based on the thesis findings. Coupled ocean-atmosphere modeling will be helpful in corroborating or invalidating this model. The model building blocks include:

- NAO (linked with -ve SSTs and +ve westerlies in subpolar Atlantic) leads to northward excursion of the Gulf Stream; the dynamical processes leading to northward excursion of the Gulf Stream remain to be elucidated.
- Inundation of the Labrador and Irminger Basins with warm-salty water, and its continued intrusion in Iceland & Greenland Seas leads to a –ve NAO
- Resulting northeasterlies drive cold-fresh water from the sub-Arctic to the subpolar North Atlantic (from strengthened E. Greenland current), setting the stage for return of +ve NAO phase; completing the cycle.

Bibliography

Alexander, M. A., & Deser, C. (1995). A mechanism for the recurrence of wintertime midlatitude SST anomalies. Journal of physical oceanography, 25(1), 122-137.

Bjerknes, J. (1964). Atlantic air-sea interaction. Advances in Geo- physics, Vol. 10, Academic Press, 1–82.

Boyer, T. P., S. Levitus, J. Antonov, R. Locarnini, and H. Garcia (2005). Linear trends in salinity for the World Ocean, 1955–1998. *Geophys. Res. Lett.*, **32,** L01604. doi:10.1029/2004GL021791.

Booth B, Dunstone NJ, Halloran PR, Andrews T, Bellouin N (2012). Aerosols implicated as a prime driver of twentieth-century North Atlantic climate variability. *Nature*, doi:10.1038/nature10946.

Bryan, K., & Stouffer, R. (1991). A note on Bjerkne's hypothesis for North Atlantic variability. *Journal of Marine Systems*, *1*(3), 229-241.

Carton J., Giese B. and Grodsky S. (2005). Sea level rise and the warming of the oceans in the SODA ocean reanalysis, *J. Geophys. Res.*, 110, doi: 10.1029/2004JC002817

Cassou, C., Deser, C., & Alexander, M. A. (2007). Investigating the impact of reemerging sea surface temperature anomalies on the winter atmospheric circulation over the North Atlantic. *Journal of climate*, *20*(14).

Chaudhuri, A. H., Gangopadhyay, A., & Bisagni, J. J. (2011). Contrasting Response of the Eastern and Western North Atlantic Circulation to an Episodic Climate Event**. Journal of Physical Oceanography, 41(9).

Chu, P. C. (2011). Global upper ocean heat content and climate variability. Ocean Dynamics, 61 (8), 1189-1204.

Collins WD, and Coauthors (2006). The Community Climate System Model Version 3 (CCSM3). *J. Clim.* **19**, 2122–2143. doi: http://dx.doi.org/10.1175/JCLI3761.1

Collins WJ, and Coauthors (2008). Evaluation of the HadGEM2 model. Met Office Hadley Centre Technical Note no. HCTN 74, available from Met Office, FitzRoy Road, Exeter EX1 3PB http://www.metoffice.gov.uk/publications/HCTN/index.html .

Cohen, R. A. (1999). An introduction to PROC LOESS for local regression. Paper presented at the Proceedings of the 24th SAS Users Group International Conference, Paper.

Craig, J., Fitzpatrick, C., Senciall, D., Stead, P., Bailey, W., & Department of Fisheries and Oceans, Ottawa, ON(Canada); Canadian Science Advisory Secretariat, Ottawa, ON(Canada). (2005). *An assessment of the physical oceanographic environment on the Newfoundland and Labrador Shelf during 2004*. Canadian Science Advisory Secretariat= Secrétariat canadien de consultation scientifique.

Danabasoglu, G., Ferrari, R., & McWilliams, J. C. (2008). Sensitivity of an ocean general circulation model to a parameterization of near-surface eddy fluxes. *Journal of Climate*, *21*(6).

Delworth TL, and Coauthors (2006). GFDL’s CM2 global coupled climate models—Part 1: Formulation and simulation characteristics, *J. Clim.*, **19**, 643– 674.

Delworth, T. L., & Greatbatch, R. J. (2000). Multidecadal thermohaline circulation variability driven by atmospheric surface flux forcing. *Journal of Climate*, *13*(9), 1481-1495.

Deser, C. (2000). On the teleconnectivity of the “Arctic Oscillation”. *Geophysical Research Letters*, *27*(6), 779-782.

Deser, C., and M. L. Blackmon (1993). Surface climate variations over the North Atlantic Ocean during winter: 1900-89. J. Clim, 6, 1743-1753.

Deser, C., Holland, M., Reverdin, G. and Timlin, M. (2002). Decadal variations in Labrador Sea ice cover and North Atlantic sea surface temperatures. J. Geophys. Res. 107(C5): doi: 10.1029/2000JC000683.

Dijkstra, H. A., Te Raa, L., Schmeits, M., & Gerrits, J. (2006). On the physics of the Atlantic multidecadal oscillation. *Ocean Dynamics*, *56*(1), 36-50.

Dima, M. and Lohmann, G. (2007). A hemispheric mechanism for the Atlantic multidecadal oscillation. *Journal of Climate*, *20*(11).

Donner LJ et al. (2011). The dynamical core, physical parameterizations, and basic simulation characteristics of the atmospheric component of the GFDL global coupled model CM3. *J. Clim.*, **24**, 3484–3519. doi: http://dx.doi.org/10.1175/2011JCLI3955.1

Enfield D.B. and Mayer D.A. (1997). Tropical Atlantic sea surface temperature variability and its relation to El Niño-Southern Oscillation. J of Geophys. Res., 102 doi: 10.1029/96JC03296

Enfield D., Mestas-Nunez E. and Trimble P. (2001). The Atlantic Multidecadal Oscillation and its Relation to Rainfall and River Flows in the Continental US. Geophys Res Lett 28: 2077-2080

Enfield C. and Cid-Serrano L. (2006). Projecting the risk of future climate shifts, doi: 10.1002/joc.1293

Evan, AT., Vimont DJ, Heidinger AK, Kossin JP, Bennartz R (2009). The Role of Aerosols in the Evolution of Tropical North Atlantic Ocean Temperature Anomalies. *Science*, **324,** 778-781. doi: 10.1126/science.1167404

Fan, M. and Schneider, E. K. (2012). Observed Decadal North Atlantic Tripole SST Variability. Part I: Weather Noise Forcing and Coupled Response, J. Atmos. Sci., 69, 35-50, doi: 10.1175/JAS-D-11-018.1

Fanning, A. F. and Weaver, A. J. (1997). A horizontal resolution and parameter sensitivity study of heat transport in an idealized coupled climate model. Journal of climate, 10(10), 2469-2478.

Femke de Jong, M. F., van Aken, H. M., V√•ge, K., & Pickart, R. S. (2012). Convective mixing in the central Irminger Sea: 2002,Äì2010. Deep Sea Research Part I: Oceanographic Research Papers, 63, 36-51.

Flatau, M. K., Talley, L., & Niiler, P. P. (2003). The North Atlantic Oscillation, surface current velocities, and SST changes in the subpolar North Atlantic. *Journal of Climate*, *16*(14).

Frankignoul, C., Müller, P., & Zorita, E. (1997). A Simple Model of the Decadal Response of the Ocean to Stochastic Wind Forcing*. *Journal of Physical Oceanography*, *27*(8), 1533-1546.

Frankcombe, L. M. and Dijkstra, H. A. (2011). The role of Atlantic‐Arctic exchange in North Atlantic multidecadal climate variability. *Geophysical Research Letters*, *38*(16).

Frankcombe L. M. (2010). The Atlantic Multidecadal Oscillation in models and observations, Natuuren Sterrenkunde Proefschriften, http://igitur-archive.library.uu.nl/dissertations/2010-0617-200232/UUindex.html

Gelderloos, Renske, Fiammetta Straneo, Caroline A. Katsman (2012). Mechanisms behind the Temporary Shutdown of Deep Convection in the Labrador Sea: Lessons from the Great Salinity Anomaly Years 1968–71. *J. Climate*, **25**, 6743–6755. doi: http://dx.doi.org/10.1175/JCLI-D-11-00549.1

Gent PR, and Coauthors (2011). The Community Climate System Model Version 4. *J. Clim.*, 24, 4973–4991. doi: http://dx.doi.org/10.1175/2011JCLI4083.1

Good, S. A., Martin, M. J. and Rayner, N. A. (2013). EN4: Quality controlled ocean temperature and salinity profiles and monthly objective analyses with uncertainty estimates. Journal of Geophysical Research: Oceans, 118(12), 6704-6716.

Gordon, C, Cooper C, Senior CA, Banks H, Gregory JM, Johns TC, Mitchell JFB, Wood RA (2000). The simulation of SST, sea ice extents and ocean heat transports in a version of the Hadley Centre coupled model without flux adjustments. *Clim. Dyn.,* **16,** 147–168.

Griffies, S.M. et al. (2011). The GFDL CM3 Coupled Climate Model: Characteristics of the Ocean and Sea Ice Simulations. *J. Clim.*, **24**, 3520–3544. doi: http://dx.doi.org/10.1175/2011JCLI3964.1

Guan, B., and S. Nigam (2009). Analysis of Atlantic SST variability factoring inter-basin links and the secular trend: Clarified structure of the Atlantic Multidecadal Oscillation. *J. Clim.*, **22**, 4228-4240.

Hansen et. al (2005). Earth's energy imbalance: Confirmation and implications. *Science*, 308, 1431-1435, doi: 10.1126/science.1110252

Hasselmann, K. (1974). On the spectral dissipation of ocean waves due to white capping. *Boundary-Layer Meteorology*, *6*(1-2), 107-127.

Haupt, B. J. and Seidov D. (2007). Strengths and weaknesses of the global ocean conveyor: Inter-basin freshwater disparities as the major control. *Progress in Oceanography*, *73*(3), 358-369.

Hodson D., Sutton R., Cassou C., Keenlyside N., Okumura Y. and Zhou T. (2010). Climate impacts of recent multidecadal changes in Atlantic Ocean Sea Surface Temperature: a multimodel comparison. Clim Dyn 34:1041-1058. doi: 10.1007/s00382-009-0571-2

Huang B. et al (2011). Influences of tropical–extratropical interaction on the multidecadal AMOC variability in the NCEP climate forecast system. Clim Dyn doi: 10.1007/s00382-011-1258-z

Hughes SL et al. (2009). Comparison on *in situ* time-series of temperature with gridded sea surface temperature datasets in the North Atlantic. *J. Mar. Sci.*, **66**, 1467-1479.

Hurrell J. W. et al. (2010). Decadal Climate Prediction: Opportunities and Challenges. Proceedings of Ocean Obs'09: Sustained Ocean Observations and Information for Society (Vol. 2), Venice, Italy, 21-25 September 2009, Hall J, Harrison DE, Stammer D, Eds., ESA Publication WPP-306.

Hurrell, J. W. (1995). Decadal trends in the North Atlantic oscillation. Science, 269, 676-679.

Joyce, T. M., Deser, C. and Spall, M. A. (2000). The relation between decadal variability of subtropical mode water and the North Atlantic Oscillation. *Journal of Climate*, *13*(14).

Jungclaus, J. H., Haak, H., Latif, M., & Mikolajewicz, U. (2005). Arctic–North Atlantic Interactions and Multidecadal Variability of the Meridional Overturning Circulation. *Journal of Climate*, *18*(19).

Kalnay et al. (1996). The NCEP/NCAR 40-year reanalysis project, Bull. Amer. Meteor. Soc., 77, 437-470.

Kavvada A, Ruiz-Barradas A, Nigam S. (2013). AMO's structure and climate footprint in observations and IPCC AR5 climate simulations. *Clim. Dyn.*, on line first article, DOI 10.1007/s00382-013-1712-1.

Keenlyside N.S., Latif M., Jungclaus J., Kornblueh L. and Roeckne E. (2008). Advancing decadal-scale climate prediction in the North Atlantic sector. Nature 453, 84-88

Kelly, K. A., and S. Dong (2004). The Relationship of Western Boundary Current Heat Transport and Storage to Mid-Latitude Ocean-Atmosphere Interaction, in . *Earth's Climate: The Ocean-Atmosphere Interaction,* edited by C. Wang, S.-P. Xie, and J. A. Carton, pp. 347-363, American Geophysical Union Geophysical Monograph 147.

Kerr, R. A. (2000). A North Atlantic climate pacemaker for the centuries *Science* 288 (5473): 1984–1986. doi:10.1126/science.288.5473.1984.

Knight J, Folland C. and Scaife A. (2006). Climate impacts of the Atlantic Multidecadal Oscillation. Geophys Res. Lett., **33**: L17706. doi: 10.1029/2006GL026242

Kushnir, Y. (1994). Interdecadal variations in North Atlantic sea surface temperature and associated atmospheric conditions. *J. Clim.,* **7**: 141–157.

Kushnir, Y, Seager R, Ting M, Naik N, Nakamura J (2010). Mechanisms of Tropical Atlantic SST Influence on North American Precipitation Variability. *J. Clim.*, **23**, 5610–5628. doi: http://dx.doi.org/10.1175/2010JCLI3172.1

Kwon, Y. O. and Frankignoul, C. (2012). Stochastically-driven multidecadal variability of the Atlantic meridional overturning circulation in CCSM3. *Climate dynamics*, *38*(5-6), 859-876.

Latif M et al. (2004). Reconstructing, monitoring, and predicting decadal-scale changes in the North Atlantic thermohaline circulation with sea surface temperature. *J. Clim.,***17,** 1605–1614.

Latif M. (2001). Tropical Pacific/Atlantic Ocean Interactions at Multi-Decadal Time Scales. Geophys Res Lett, 28, 539-542

Lee, S. K. and Wang, C. (2010). Delayed Advective Oscillation of the Atlantic Thermohaline Circulation. *Journal of Climate*, *23*(5).

Levitus, S., J. Antonov, T. P. Boyer, and C. Stephens (2000). Warming of the world ocean, Science, 287, 2225–2229.

Levitus, S., J. L. Antonov, J. Wang, T. L. Delworth, K. W. Dixon, and A. J. Broccoli (2001). Anthropogenic warming of Earth's climate system, Science, 292, 267–270.

Levitus, S., J. Antonov, and T. Boyer (2005). Warming of the world ocean, 1955–2003, Geophys. Res. Lett., 32, L02604, doi:10.1029/ 2004GL021592.

Lozier, M. S., S. Leadbetter, R. G. Williams, V. Roussenov, M. S. C. Reed, and N. J. Moore (2008). The spatial pattern and mechanisms of heat-content change in the North Atlantic. *Science*, **319**, 800–803, doi:10.1126/science.1146436.

Mann M.E. and Emanuel K.A. (2006). Atlantic Hurricane Trends Linked to Climate ChangeEos, Vol. 87, No. 24 : 233–244

Mantua NJ, Hare SR, Zhang Y, Wallace JM, Francis RC (1997) A Pacific interdecadal climate oscillation with impacts on salmon production. *Bull. Amer. Meteor. Soc.*, **78**, 1069-1079.

Marsland SJ, Haak H, Jungclaus JH, Latif M, Roeske F (2003) The Max-Planck-Institute global ocean/sea ice model with orthogonal curvilinear coordinates. *Ocean Modelling*, **5**, 91-127; HAMOCC: Technical Documentation, http://www.mpimet.mpg.de/fileadmin/models/MPIOM/HAMOCC5.1_TECHNICAL_REPORT.pdf

Marshall, J., Kushnir, Y., Battisti, D., Chang, P., Czaja, A., Dickson, R., ... & Visbeck, M. (2001). North Atlantic climate variability: phenomena, impacts and mechanisms. *International Journal of Climatology*, *21*(15), 1863-1898.

Mauritzen, C., Melsom, A., & Sutton, R. T. (2012). Importance of density-compensated temperature change for deep North Atlantic Ocean heat uptake. *Nature Geoscience*, *5*(12), 905-910.

McCabe GJ, Betancourt JL, Gray ST, Palecki MA, Hidalgo HG (2008) Associations of multi-decadal sea-surface temperature variability with US drought. *Quat. Int.,* **188**, 31–40, doi:10.1016/j.quaint.2007.07.001.

McCartney, M. S., & Talley, L. D. (1984). Warm-to-cold water conversion in the northern North Atlantic Ocean. *Journal of Physical Oceanography*, *14*(5), 922-935.

Medhaug I, Furevik T (2011). North Atlantic 20th century multidecadal variability in coupled climate models: sea surface temperature and ocean overturning circulation. *Ocean Sci. Discuss,* 8: 353–396.

Meehl G, Tebaldi C., Walton G., Easterling D. and McDaniel L. (2009). Relative increase of record high maximum temperatures compared to record low minimum temperatures in the U.S. Geoph. Res. Lett. 36 L23701. doi:10.1029/2009GL040736

Meinshausen, M. et al. (2011). The RCP Greenhouse Gas Concentrations and their Extension from 1765 to 2300, *Clim. Change*, 109, 213-241. Doi 10.1007/s10584-011-0156-z.

Mitchell and Jones (2005). An improved method of constructing a database of monthly climate observations and associated high-resolution grids. International Journal of Climatology, doi: 10.1002/joc.1181

Nakamura, M., Stone, P. H., & Marotzke, J. (1994). Destabilization of the thermohaline circulation by atmospheric eddy transports. *Journal of Climate*, *7*(12), 1870-1882.

Nigam S., Guan B., and Ruiz-Barradas A. (2011). Key role of the Atlantic Multidecadal Oscillation in 20th century drought and wet periods over the Great Plains. Geophys Res Lett 38: L16713. doi: 10.1029/2011GL048650

Osborn, T. J. (2011). Winter 2009/2010 temperatures and a record‐breaking North Atlantic Oscillation index. *Weather*, *66*(1), 19-21.

Peings, Y. and Magnusdottir G. (2014). Forcing of the wintertime atmospheric circulation by the multidecadal fluctuations of the North Atlantic ocean. *Environmental Research Letters*, *9*(3), 034018.

Peterson, B. J., McClelland, J., Curry, R., Holmes, R. M., Walsh, J. E., & Aagaard, K. (2006). Trajectory shifts in the Arctic and subarctic freshwater cycle. Science, 313(5790), 1061-1066.

Perez-Hernandez, M. D., and Joyce, T. M. (2014). Two Modes of Gulf Stream Variability Revealed in the Last Two Decades of Satellite Altimeter Data. Journal of Physical Oceanography, 44(1).

Pickart, R. S., Straneo, F. and Moore, G. W. K. (2003). Is Labrador sea water formed in the Irminger basin?. *Deep Sea Research Part I: Oceanographic Research Papers*, *50*(1), 23-52.

Polyakov, IV, Bhatt US, Simmons HL, Walsh D, Walsh JE, Zhang X. (2005). Multidecadal variability of North Atlantic temperature and salinity during the Twentieth Century. J. Clim. 18: 4562-4581.

Polyakov, I. V. et al. (2005). One more step toward a warmer Arctic, Geophys Res Lett 32, L17605, doi:10.1029/2005GL023740

Pope VD, Gallani ML, Rowntree PR, Stratton RA (2000) The impact of new physical parametrizations in the Hadley Centre climate model–HadAM3. *Clim. Dyn.,* **16,** 123–146.

Power, S. B., Tseitkin, F., Dix, M., Kleeman, R., Colman, R., & Holland, D. (1995). Stochastic variability at the air‚Äêsea interface on decadal timescales. Geophysical research letters, 22(19), 2593-2596.

Quenouille, M. H. (1952). Associated Measurements, Academic, New York.

Raddatz TJ, Reick CH, Knorr W, Kattge J, Roeckner E, Schnur R, Schnitzler K-G, Wetzel P, Jungclaus J (2007) Will the tropical land biosphere dominate the climate-carbon cycle feedback during the twenty first century? *Clim. Dyn.*, 29, 565-574, doi 10.1007/s00382-007-0247-8.

Rayner NA, Parker DE, Horton EB, Folland CK, Alexander LV, Rowell DP, Kent EC, Kaplan A (2003). Global analyses of sea surface temperature, sea ice, and night marine air temperature since the late nineteenth century, *J. Geophys. Res.*, **108**(D14), 4407, doi:10.1029/2002JD002670.

Rayner N. A. et al. (2005) Improved Analyses of Changes and Uncertainties in Sea Surface Temperature Measured In Situ since the Mid-Nineteenth Century: The HadSST2 Dataset. J. Clim. 19 :446-468

Reverdin, G., Cayan, D. and Kushnir, Y. (1997) Decadal variability of hydrography in the upper northern North Atlantic in 1948-1990. J. Geophys. Res. 102(C4). doi: 10.1029/96JC03943.

Rodwell, M. J. and Folland, C. K. (2002). Atlantic air–sea interaction and seasonal predictability. *Quarterly Journal of the Royal Meteorological Society*, *128*(583), 1413-1443.

Roeckner E et al. (2003). The atmospheric general circulation model ECHAM5. Part I: Model description. *Max Planck Institute for Meteorology Rep. 349*, 127 pp. [Available from MPI for Meteorology, Bundesstr. 53, 20146 Hamburg, Germany.].

Ruddick, B. and Kerr, O. (2003). Oceanic thermohaline intrusions: theory. *Progress in oceanography*, *56*(3), 483-497.

Ruiz-Barradas A., Nigam S., and Kavvada A. (2013). The Atlantic Multidecadal Oscillation in twentieth century climate simulations: uneven progress from CMIP3 to CMIP5. Climate dynamics Online First, DOI 10.1007/s00382-013-1810-0.

Ruiz-Barradas, A., and S. Nigam (2005). Warm-season rainfall variability over the US Great Plains in Observations, NCEP and ERA-40 Reanalyses, and NCAR and NASA Atmospheric Model Simulations. *J. Climate*, 18, 1808-1830.

Ruiz-Barradas A., Carton J. A., Nigam S. (2000). Structure of interannual-to-decadal climate variability in the tropical Atlantic sector. J. Clim 13: 3285-3297. doi: 10.1175/1520-0442

Ruiz-Barradas A, Nigam S (2005). Warm season rainfall variability over the U.S. Great Plains in observations, NCEP and ERA-40 reanalyses, and NCAR and NASA atmospheric model simulations, *J. Clim.*,**18**, 1808–1830, doi:10.1175/JCLI3343.1.

Sato, O. T. and Rossby, T. (1995). Seasonal and low frequency variations in dynamic height anomaly and transport of the Gulf Stream. Deep Sea Research Part I: Oceanographic Research Papers, 42(1), 149-164.

Schneider, E. K. and Fan, M. (2007). Weather Noise Forcing of Surface Climate Variability, Journal Of Atmospheric Sciences, J. Atmos. Sci.,64, 3265-3280. doi: 10.1175/JAS4026.1

Schneider, E. K. and M. Fan (2012). Observed decadal North Atlantic tripole SST variability. Part II: Diagnosis of mechanisms. J. Atmos. Sci., 69, 51-64. doi: http://dx.doi.org/10.1175/JAS-D-11-019.1

Shanahan TM, Overpeck JT, Anchukaitis KJ, Beck JW, Cole JE, Dettman DL, Peck JA, Scholz CA, King JW (2009) Atlantic Forcing of Persistent Drought in West Africa. *Science* **324** (5925): 377–380. doi:10.1126/science.1166352.

Sheffield J and coauthors (2013) North America climate in CMIP5 experiments. Part II: evaluation of historical simulations of intra-seasonal to decadal variability. *Accepted to the J Clim on 4/2013*.

Slonosky, V. C., Mysak L. A. and Derome J. (1997). Linking Arctic sea-ice and atmospheric circulation anomalies on interannual and decadal timescales, *Atmos. Ocean*, *35*, 333–366, doi:10.1080/07055900.1997.9649596

Smith, T. M., Reynolds, R. W., Peterson, T. C., & Lawrimore, J. (2008). Improvements to NOAA's Historical Merged Land–Ocean Surface Temperature Analysis (1880–2006). *Journal of Climate*, *21*(10).

Stommel, H. (1961). Thermohaline convection with two stable regimes of flow. Tellus, 13(2), 224-230.

Sundby S. and Drinkwater K. (2002). On the mechanisms behind salinity anomaly signals of the northern North Atlantic. Progress In Oceanography 73(2): 190-202

Sutton R. and Hodson D. (2005). Atlantic Ocean Forcing of North American and European Summer Climate Science 309: 115-117 doi: 10.1126/science.1109496

Sutton R. and Hodson D. (2003). Influence of the Ocean on North Atlantic Climate Variability 1871-1999. *J. Clim*, 16: 3296–3313.

Taylor, A. H., & Stephens, J. A. (1998). The North Atlantic oscillation and the latitude of the Gulf Stream. *Tellus A*, *50*(1), 134-142.

Taylor K., Stouffer R. and Meehl G. (2011). An overview of CMIP5 and the Experiment Design, Bulletin of the American Meteorological Society, doi: 10.1175/BAMS-D-11-00094.1

Ting M., Kushnir Y., Seager R. and Li C. (2011). Robust Features of the Atlantic Multi-Decadal Variability and its Climate Impacts. Geophys Res Lett 38: L17705. doi: 10.1029/2011GL048712

Ting M., Kushnir Y., Seager R. and Li C. (2009). Forced and Internal Twentieth-Century SST Trends in the North Atlantic, J Clim 22: 1469-1481, doi: 10.1175/2008JCLI2561.1

Tracey, K. L. and Watts, D. R. (1986). On Gulf Stream meander characteristics near Cape Hatteras. Journal of Geophysical Research: Oceans (1978,Äì2012), 91(C6), 7587-7602.

Våge, K., Pickart, R. S., Sarafanov, A., Knutsen, Ø., Mercier, H., Lherminier, P., ... & Bacon, S. (2011). The Irminger Gyre: Circulation, convection, and interannual variability. *Deep Sea Research Part I: Oceanographic Research Papers*, *58*(5), 590-614.

Våge, K., Pickart, R. S., Thierry, V., Reverdin, G., Lee, C. M., Petrie, B., ... & Ribergaard, M. H. (2009). Surprising return of deep convection to the subpolar North Atlantic Ocean in winter 2007–2008. *Nature Geoscience*, *2*(1), 67-72.

van Aken, H. M., Femke de Jong, M., & Yashayaev, I. (2011). Decadal and multi-decadal variability of Labrador Sea Water in the north-western North Atlantic Ocean derived from tracer distributions: Heat budget, ventilation, and advection. *Deep Sea Research Part I: Oceanographic Research Papers*, *58*(5), 505-523.

Volkov, D. L. and Van Aken, H. M. (2005). Climate‐related change of sea level in the extratropical North Atlantic and North Pacific in 1993–2003. *Geophysical research letters*, *32*(14).

Walter, K. and Graf, H. F. (2005). The North Atlantic variability structure, storm tracks, and precipitation depending on the polar vortex strength. *Atmospheric Chemistry and Physics*, *5*(1), 239-248.

Wang, H., Fu R., Kumar A. and Li W. H. (2010). Intensification of summer rainfall variability in the southeastern United States during recent decades. J. Hydrometeor., 11, 1007– 1018.

Wang, C. and Zhang, L. (2013). Multidecadal Ocean Temperature and Salinity Variability in the Tropical North Atlantic: Linking with the AMO, AMOC, and Subtropical Cell. *Journal of Climate*, *26*(16).

Wang, C., Dong, S. and Munoz, E. (2010). Seawater density variations in the North Atlantic and the Atlantic meridional overturning circulation. *Climate dynamics*, *34*(7-8), 953-968.

Webster, P. J., G. J. Holland, J. A. Curry, and H.-R. Chang (2005). Changes in tropical cyclone number, duration and intensity in a warming environ- ment, Science, 309, 1844–1846.

Wu, P. and Rodwell, M. J. (2004). Gulf Stream forcing of the winter North Atlantic oscillation. *Atmospheric Science Letters*, *5*(1-4), 57-64.

Yashayaev, I., van Aken, H. M., Holliday, N. P. and Bersch, M. (2007). Transformation of the Labrador Sea water in the subpolar North Atlantic. Geophysical Research Letters, 34(22).

Yoshimori, M., Raible, C. C., Stocker, T. F. and Renold, M. (2010). Simulated decadal oscillations of the Atlantic meridional overturning circulation in a cold climate state. *Climate dynamics*, *34*(1), 101-121.

Zhang R. and Delworth T. (2006). Impact of Atlantic multidecadal oscillations on India/Sahel rainfall and Atlantic hurricanes. Geophys Res Lett 33: L17712. doi:10.1029/2006GL026267

Zhang R. and Vallis G.K. (2006). Impact of Great Salinity Anomalies on the Low-Frequency Variability of the North Atlantic Climate. J. Climate, 19, 470–482.

Zhang R. (2007). Anticorrelated multidecadal variations between surface and subsurface tropical North Atlantic. Geoph Res Lett 34: L12713. doi:10.1029/2007GL030225

Zhang R. et al. (2013). Have aerosols caused the observed Atlantic Multidecadal variability? *J. Atmos. Sci.*, **70**, 1135-1144.